NUEJ

NARESUAN UNIVERSITY ENGINEERING JOURNAL

January-June 2023 Vol.18, No.1
ISSN : 2651-1568

NUEJ
Naresuan University
Engineering Journal

Editorial Team

Advisory

Prof. Dr. Somchai Wongwises	Faculty of Engineering, King Mongkut's University of Technology Thonburi
Assoc. Prof. Dr. Uraya Weesakul	Faculty of Engineering, Thammasat University
Assoc. Prof. Dr. Sarintip Tantanee	Faculty of Engineering, Naresuan University
Assoc. Prof. Dr. Suchart Yammen	Faculty of Engineering, Naresuan University

Editor

Asst. Prof. Dr. Panu Buranajarukorn	Faculty of Engineering, Naresuan University

Associate Editor

Asst. Prof. Dr. Panatpong Boonnoun	Faculty of Engineering, Naresuan University

Editorial Board

Prof. Dr. Kosin Chamnongthai	Faculty of Engineering, King Mongkut's University of Technology Thonburi
Prof. Dr Juntaraporn Palagongun	Faculty of Engineering, King Monkut's University of Technology North Bangkok
Prof. Dr. Pradit Terdtoon	Faculty of Engineering, Chiang Mai Univerisity
Prof. Dr. Puangrat Kajitvichyanukul	Faculty of Engineering, Chiang Mai Univerisity
Prof. Dr. Wanida Jinsart	Faculty of Science, Chulalongkorn University
Prof. Dr. Virote Boonamnuayvitaya	Faculty of Engineering, King Mongkut's University of Technology Thonburi
Prof. Dr. Vatanavongs Ratanavaraha	Institute of Engineering, Suranaree University of Tecnology
Prof. Dr. Somchai Wongwises	Faculty of Engineering, King Mongkut's University of Technology Thonburi
Prof. Dr. Sampan Rittidej	Faculty of Engineering, Mahasarakham University

NUEJ
Naresuan University
Engineering Journal

Editorial Board

Prof. Dr. Sumrerng Jugjai	Faculty of Engineering, King Mongkut's University of Technology Thonburi
Prof. Dr. Apinunt Thanachayanont	Faculty of Engineering, King Mongkut's Institute of Technology Ladkrabang
Prof. Dr. Issarachai Ngamroo	Faculty of Engineering, King Mongkut's Institute of Technology Ladkrabang
Prof. Christian Hicks	Newcastle University, United Kingdom
Prof. Dr. Paisarn Muneesawang	Faculty of Engineering, Naresuan University
Prof. Dr. Songphol Kanjanachuchai	Faculty of Engineering, Chulalongkorn University
Assoc. Prof. Dr. Kamchai Nuithitikul	Faculty of Engineering, Walailak University
Assoc. Prof. Dr.Chalermraj Wantawin	Faculty of Engineering, King Mongkut's University of Technology Thonburi
Assoc. Prof. Dr. Nipon Theeraumpon	Faculty of Engineering, Chiang Mai Univerisity
Assoc. Prof. Dr. Ninlawan Choomrit	Faculty of Engineering, Srinakharinwirot University
Assoc. Prof. Dr. Nivit Charoenchai	Faculty of Engineering, Chiang Mai Univerisity
Assoc. Prof. Dr. Yodchanan Wongsawat	Faculty of Engineering, Mahidol University
Assoc. Prof. Dr. Lunchakorn Wuttisittikulkij	Faculty of Engineering, Chulalongkorn University
Assoc. Prof. Dr. Watcharin Pongaen	Faculty of Engineering, King Mongkut's University of Technology North Bangkok
Assoc. Prof. Dr. Wassanai Wattanutchariya,	Faculty of Engineering, Chiang Mai Univerisity
Assoc. Prof. Dr. Virasit Imtawil	Faculty of Engineering, Khon Kaen University
Assoc. Prof. Sanguan Patamatamkul	Faculty of Engineering, Khon Kaen University
Assoc. Prof. Dr. Sdhabhon Bhokha	Faculty of Engineering, Ubon Ratchathani University
Assoc. Prof. Maetee Boonpichetvong	Faculty of Engineering, Khon Kaen University
Assoc. Prof. Dr.Tanyada Pannachet	Faculty of Engineering, Khon Kaen University
Assoc. Prof. Dr. Suwit Kiravittaya	Faculty of Engineering, Chulalongkorn University
Assoc. Prof. Dr.Athikom Roeksabutr	Faculty of Engineering, Mahanakorn University of

NUEJ
Naresuan University
Engineering Journal

Technology

Editorial Board

Assoc. Prof. Dr. Vo Ngoc Dieu	Ho Chi Minh City University of Technology, Vietnam
Assoc. Prof. Dr. Koonlaya Kanokjaruvijit	Faculty of Engineering, Naresuan University
Assoc. Prof. Dr. Thawatchai Mayteevarunyoo	Faculty of Engineering, Naresuan University
Assoc. Prof. Dr. Suchart Yammen	Faculty of Engineering, Naresuan University
Assoc. Prof. Dr. Sombat Chuenchooklin	Faculty of Engineering, Naresuan University
Assoc. Prof. Dr. Samorn Hirunpraditkoon	Faculty of Engineering, Naresuan University
Assoc. Prof. Dr. Mathanee Sanguansermsri	Faculty of Engineering, Naresuan University
Assoc. Prof. Dr. Apichai Ritvirool	Faculty of Engineering, Naresuan University
Assoc. Prof. Dr. Pupong Pongcharoen	Faculty of Engineering, Naresuan University
Assoc. Prof. Dr. Panus Nattharith	Faculty of Engineering, Naresuan University
Asst. Prof. Dr. Kaokanya Sudaprasert	Faculty of Engineering, King Mongkut's University of Technology Thonburi
Asst. Prof. Dr. Korakod Nusit	Faculty of Engineering, Naresuan University
Asst. Prof. Dr. Pajaree Thongsanit	Faculty of Engineering, Naresuan University
Asst. Prof. Dr. Supawan Ponpitakchai	Faculty of Engineering, Naresuan University
Asst. Prof. Dr. Somlak Wannarumon Kielarova	Faculty of Engineering, Naresuan University
Asst. Prof. Dr. Sasikorn Leungvichcharoen	Faculty of Engineering, Naresuan University
Asst. Prof. Dr. Ananchai U-kaew	Faculty of Engineering, Naresuan University
Asst. Prof. Dr. Sutanit Puttapanom	Faculty of Engineering, Naresuan University
Asst. Prof. Dr. Narumon Seeponkai	Faculty of Engineering, Naresuan University
Asst. Prof. Dr. Tanikan Thongchai	Faculty of Engineering, Naresuan University
Asst. Prof. Dr. Jirawadee Polprasert	Faculty of Engineering, Naresuan University
Dr. Ivan Lee	School of Information Technology and Mathematical Sciences, University of South Australia, Australia
Dr. Sasidharan Sreedharan	University of Hawaii, USA
Dr. Salisa Veerapun	Faculty of Engineering, Naresuan University

NUEJ
Naresuan University
Engineering Journal

Research Articles

Aims and Objectives

The primary objective of the *Naresuan University Engineering Journal (NUEJ)* is to publish high quality research articles presenting contemporary developments in theory, design, and applications in all areas of Engineering, Science and Technology, including research in Civil and Environmental Engineering, Mechanical Engineering, Electrical and Computer Engineering, Industrial, Chemical, and Material Engineering. NUEJ covers all multidisciplinary research in associated areas**,** such as Mechatronics, Energy, Industrial and Engineering Design, Manufacturing Technology, Engineering Management and Medical Engineering.

Journal Policies

Naresuan University Engineering Journal (NUEJ) is a peer reviewed journal, regularly published with 2 issues per year (January – June, and July – December). Submissions must be original, unpublished works, and not currently under review by other journals. NUEJ will consider only submitted works which respect research ethics, including confidentiality, consent, and the special requirements for human and animal research. All research articles dealing with human or animal subjects must attach an approval certificate from the appropriate Ethics Committee. Additionally, the research articles dealing with human subjects must provide evidence of informed consent.

Editorial board of NUEJ reserves the right to decide whether the submitted manuscript should be accepted for publication. The final decision of the editorial board cannot be appealed.

The submitted manuscript has to be written in English only, and can be in Microsoft Word (doc or docx) or PDF file format. The corresponding author is required to register and submit the manuscript at https://ph01.tci-thaijo.org/index.php/nuej

Editorial board of Naresuan University Engineering Journal
Faculty of Engineering, Naresuan University,
Phitsanulok, 65000, Thailand
Tel. +66 (0) 55 964092
Fax +66 (0) 55 964000
Email: nuej@nu.ac.th

Editor's Note

I am pleased to present the Naresuan University Engineering Journal (NUEJ), which provides useful knowledge, technology and engineering innovation for academia and researchers. This journal is provided in an electronic open-access platform for easily sharing new knowledge and ideas in all areas of engineering. To ensure the publication maintains high standards, the journal has qualification procedures for receiving articles, peer review, and acceptance for publication. Recently, the NUEJ was approved to be in the first tier of the Thai-Journal Citation Index (TCI 1) and the ASEAN Citation Index (ACI).

In this issue, the NUEJ Vol.18 No.1 (2023), articles pertaining to various fields of engineering e.g. water resources, civil engineering, mechanical engineering, electrical engineering, materials engineering, and production engineering, are published. Hopefully, the advanced engineering knowledge and technology in the papers are suitable for applying in industrial sectors and they can be used as guides for future research. Finally, I would like to give thanks to the authors and reviewers for their contributions.

Assistant Professor Dr. Panu Buranajarukorn
Editor
Naresuan University Engineering Journal

NUEJ
Naresuan University
Engineering Journal

Low-Flow Assessment Methods for Ungauged Sub-Basins in the Upper Ping River Basin, Thailand

Sokseyla Man[1] and Supattra Visessri[2,*]

[1,2] Department of Water Resources Engineering, Faculty of Engineering, Chulalongkorn University, Bangkok 10330, Thailand
[2] Disaster and Risk Management Information Systems Research Unit, Chulalongkorn University, Bangkok 10330, Thailand

* Corresponding author e-mail: supattra.vi@chula.ac.th

(Received: 24 July 2022, Revised: 6 December 2022, Accepted: 15 December 2022)

Abstract

The assessment of low-flow in ungauged or poorly-gauged basins where the flow data are unavailable remains a challenge in many parts of the world. This study aims to address the low-flow assessment in the ungauged sub-basins in Thailand by regionalizing low flow indices including the base-flow index (BFI), 95th percentile-flow (Q95) and the annual minimum 7-day moving average flow with a 10-year recurrence interval (7Q10). The framework is demonstrated through the case study of 25 sub-basins of the Upper Ping River basin with available data from 1995-2014. Performance of two widely used regionalization methods, the regression and climate adjustment methods are tested and compared. The accuracy of the methods is assessed by comparing the predicted with the observed low-flow indices calculated in terms of R^2, NSE, and RMSE. The results of the regression method indicate that the method performs best for predicting 7Q10 compared to Q95 and BFI. The best R^2, RMSE, and NSE values obtained from the regression model for predicting 7Q10 are 0.95, 0.95, and 0.26 respectively. The results of the climate adjustment method show that the method with a comparatively long overlap period is found to improve over the regression method. The longest 15 overlap period tested in this study show that the R^2 and RMSE can be improved to almost 1.00 and NSE can be reduced to 0.09. While this study could offer a way forward improving low-flow estimation and water resources management in ungauged basins, further study on non-stationarity of the basin is recommended.

Keywords: Climate adjustment, Low-flow indices, Record augmentation, Regional regression, Upper Ping River Basin

1. INTRODUCTION

Water is vital for human living and essential for environmental, economic, and ecological management. Due to the growth of the global population, the water demand for food production and social development towards better living conditions have also been increasing (Kundzewicz, 1997). Since the amount of water is limited especially in the dry year while the demand has increased higher, this may lead some areas to face the problem of water scarcity. In order to cope with the problem, the management of water resources is necessary. In recent years, water resources management has become more focused on mid-term and long-term planning for water demand and conservation management, water transfer, and diversion (Karamouz et al., 2003). For riparian countries, monitoring of flow characteristics in the river basin is the principal for water resources management responding to the problem of water scarcity. One of the most essential indicators which are beneficial for flow characterization is known as "low-flow" which is defined as "flow of water in a stream during prolonged dry weather" (Smakhtin, 2001). During low-flow periods, most stream habitats are reduced in area and and may also affect biota. Low-flow characteristics information provides threshold values for different water-based activities and is required for some water resources management such as irrigation, water supply, and water quality and quantity estimations (Eslamian, 2018).

In Thailand, there are more flood studies than drought or low-flow. The method for low-flow estimation has been paid little attention. This study focuses on assessing the techniques for estimating low-flow in gauged and ungauged sub-basins of the Upper Ping River basin where the hydrological study is particularly challenging due to limited available data. A previous study by Visessri (2014) used BFI as a low-flow index to predict flow in the Upper Ping River basin. This study introduced other two low-flow indices (Q95 and 7Q10) that might be useful for the prediction in ungauged basins. The objective of this study is to define the applicable method for low-flow estimation in ungauged sub-basins of the Upper Ping River basin which is the headwater of the Chao Phraya basin. If the low-flow in the Upper Ping River basin can be monitored, it could also reduce the risk of water scarcity in the Chao Phraya basin.

2. DATA

2.1 Study Area

This study is conducted in the Upper Ping River basin which is in the northwestern part of Thailand. It stretches from latitude 17°00'N to 19°48'N and from longitude 98°05'E to 99°23'E and covers a total area of 26,674 km^2 with elevation ranges from 195 to 2577 m a.s.l (meter above mean sea level) as shown in Figure 1. The west of the basin is mainly mountainous while the central and the east of the basin are relatively flat. The major water resource is the Ping River flowing from the north to the south. The Bhumibol reservoir separates the upper and lower part of the Ping basin. The basin has a varied climate with a mean annual rainfall of 1,097 mm (Sharma & Babel, 2014).

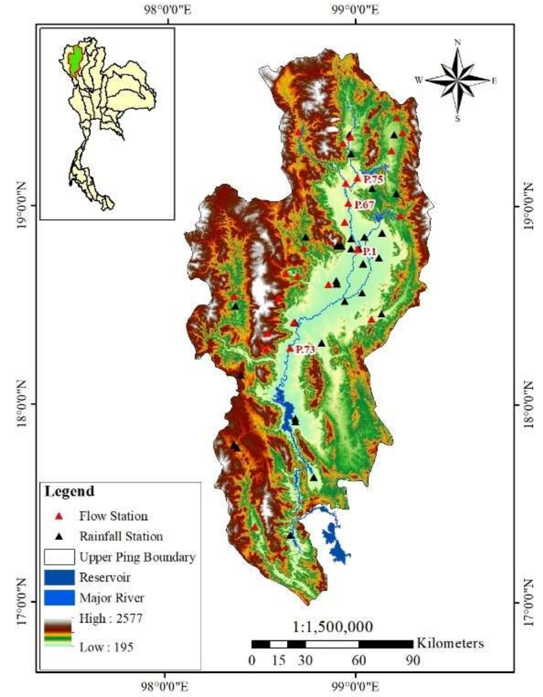

Figure 1 Elevation of the Upper Ping River basin

2.2 Flow Data and Rainfall Data

Flow data and rainfall data used in this study are daily series from 25 flow gauges obtained from the Royal Irrigation Department (RID) and the Department of Water Resources (DWR) and 43 rain gauges obtained from RID and the Thai Meteorological Department (TMD) which have been continuously monitored from 1995 to 2014, respectively. The study period from 1995 to 2014 was selected because it has a relatively small amount of missing data and sufficiently long records for low-flow assessment. The rainfall and streamflow time series from those stations are shown in Figure 2.

2.3 Land Use

Land use is classified into five main different types, such as Forest (F), Agriculture (A), Urban (U), Open water (W), and Mixed land-use (M). The major land use of the Upper Ping River basin is the forest which covers the area of 21,235 km^2 or equal to approximately 80% of the total area. The second majority is agriculture which covers another 14% of the total area while the urban, open water and mixed land-use areas show a minor proportion to the total area. The information mentioned above is obtained by overlapping the basin boundary with the land use data of year 2005 obtained from the Land Development Department (LDD), Thailand. The land use data of year 2000 are assumed to sufficiently represent the land use condition and have negligible change over the entire period of study. This assumption is supported by the study of Visessri & McIntyre (2015) which found that the land use change in the Upper Ping River basin was not significant enough to cause an impact on the regionalized flow indices (Visessri & McIntyre, 2015).

2.4 Soil Type

Based on the soil type data obtained from LDD, there are thirty-six soil types in the Upper Ping River basin. However, only four types among the total show the major value in terms of proportion to the total area. The first majority is Soil type group 62 which distributes about 70% and can be found almost everywhere in the basin. The second and third majorities are Soil type group 48 and Soil type group 20 which distribute about 9% and 3% to the basin, respectively. Another majority which distributes about 3% to the basin also is Soil type group 29. When considering the soil type of the 25 sub-basins used in this study, Soil type group 62 remains dominant; other soil types cover much smaller area.

A summary of the basin characteristics of the 25 sub-basins used in this study is given in Table 1.

2.5 Low-flow Characteristics

There are three commonly used low-flow indices (LFI) chosen in this study. They are ninety-five-percentile flow (Q95), baseflow index (BFI), and annual minimum 7-day moving average flow with a 10-year recurrence interval (7Q10).

2.5.1 Ninety-five-percentile Flow (Q95)

Q95 represents flow that is equaled or exceeded for 95 percent of the observation period and can be determined from the flow duration curve (WMO, 2008). It can be used for establishing low-flow criteria for stream standards. Furthermore, it can be used as a reference streamflow level to differentiate drought flows from nondroughted flows (Zelenhasić & Salvai, 1987). The value of Q95 is calculated for all 25 gauges from continuous daily flow data between 1995 and 2014 and is assumed to represent the long-term average of Q95.

2.5.2 Baseflow Index (BFI)

BFI is a non-dimensional index that is defined as the baseflow volume divided by the total streamflow volume. The values range between 0 and 1. The high index of baseflow indicates that the river flow can be sustained by the basin during a prolonged dry period (WMO, 2008). In this study, the BFI is determined using the method of local minimum as described in (White & Sloto, 1990) for all the 25 gauges.

2.5.3 Annual minimum 7-day moving Average Flow with a 10-year Recurrence Interval (7Q10)

7Q10 is determined from the annual series of minimum 7-day moving average flow at the selected 25 gauges. The average flow for each consecutive 7-day period is calculated from the daily records, and the lowest average value for each year represents that year in the annual series. The 7-day minimum average flows are fit to a log-Pearson Type III distribution to determine the recurrence interval for an individual 7-day minimum mean flow (Riggs, 1972).

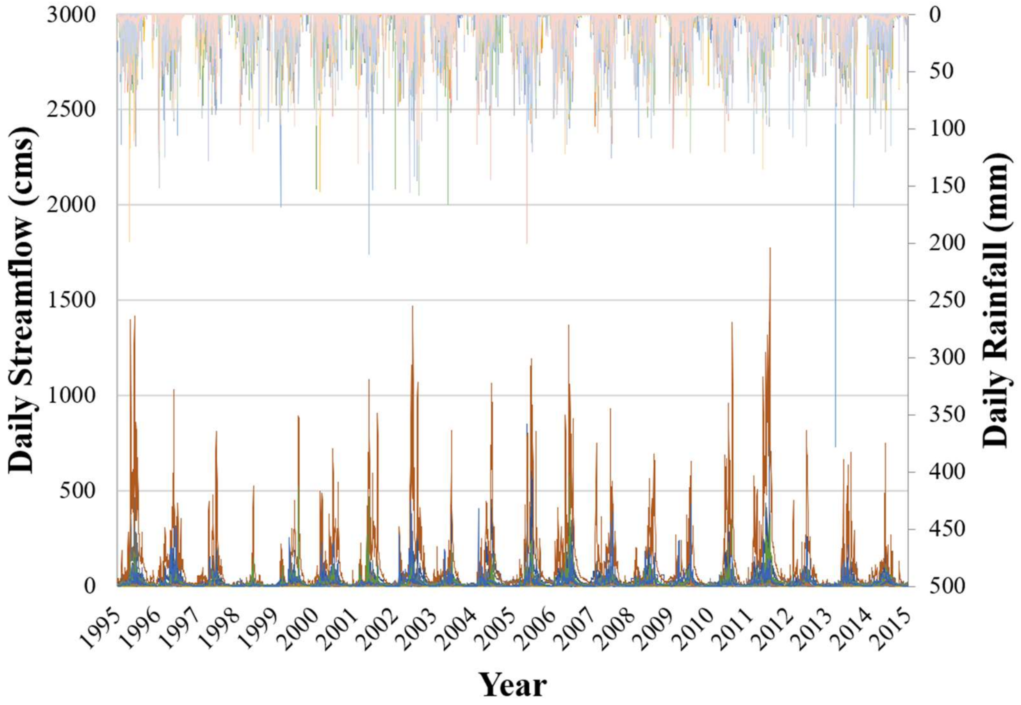

Figure 2 Daily rainfall and streamflow time series

Table 1 Statistical summary of the basin characteristics of the 25 sub-basins used in this study

Acronym	Variable description	Units	Minimum	Mean	Maximum
%A	Percentage of agriculture	%	0.01	14.43	31.17
%F	Percentage of forest	%	64.68	83.78	98.09
%G30	Percentage of soil type group 30	%	0.00	0.84	13.79
%G40	Percentage of soil type group 40	%	0.00	0.25	3.05
%G56	Percentage of soil type group 56	%	0.00	0.01	0.20
%G60	Percentage of soil type group 60	%	0.00	0.07	0.84
%G62	Percentage of soil type group 62	%	63.87	85.48	99.99
%M	Percentage of mixed-land use	%	0.00	0.42	3.37
%W	Percentage of open water	%	0.00	0.08	0.54
AMR	Annual mean rainfall	mm	912.90	1117.43	1305.40
Ar	Basin area	km^2	23.43	1638.54	14536.02
El_{max}	Maximum elevation	m	1251.00	1968.12	2577.00
El_{min}	Minimum elevation	m	195.00	436.44	1024.00
Sl_{max}	Maximum slope	%	116.25	236.32	441.30
Sl_{mean}	Mean slope	%	24.93	31.30	41.82

3. METHODOLOGY

There are two regionalization methods namely regional regression and climate adjustment used in this study because they performed reasonably well, and they require a few hydrological variables that allow us to test its applicability in the study area.

3.1 Regional Regression Method

Regional regression is a frequently used method to develop a relationship between LFI and an 'optimal' set of basin characteristics. The regression in this study is established using stepwise linear regression for homogeneous subregions to predict low-flow characteristics in ungauged sub-basins(Laaha et al., 2013). As stated in (Nathan & McMahon, 1992), a common form of prediction equations can be simplified as Eq. (1).

$$LFI = f(basin\ characteristics) \tag{1}$$

3.2 Climate Adjustment Method

The climate adjustment method is one of the methods to deal with the problem of low-flow estimation from a short streamflow record. The method consists of two steps which are the donor site selection and the record augmentation (Laaha & Blöschl, 2005). Unlike the regression method that is primarily based on the spatial relationship between the basin characteristics and LFI, the climate adjustment method is believed to be able to account for the influence of temporal variation of the climate on the prediction of LFI.

3.2.1 Donor Site Selection

In this study, the donor is selected based on the shortest Euclidean distance between the centroid of the donor (gauged) sub-basin and the centroid of the subject (ungauged) sub-basin or it is called the "Nearest basin method".

3.2.2 Record Augmentation

Once the suitable donor has been selected, the predicted LFI at the subject site can be adjusted by transferring the information from the donor based on two record augmentation techniques.

In the first technique, the predicted low-flow characteristic at subject site (QS_{pred}) is adjusted by scaling LFI calculated from the overlap period of the subject site (QS_o) with the ratio of LFI calculated from the entire observations period and LFI calculated from the overlap period of the donor site (QD and QD_o). In this study, four overlap periods of 1-yr, 5-yr, 10-yr, and 15-yr are selected to test the predictive performance. The predicted LFI at the subject site can be extrapolated using Eq. (2).

$$QS_{pred} = QS_o \times \left(\frac{QD}{QD_o}\right) \tag{2}$$

The second technique applies the same principle, but a weighting coefficient M(r) is included to account for the robustness of correlation between subject and donor sites. The predicted LFI at the subject site can be extrapolated using Eq. (3).

$$QS_{pred} = QS_o \times \left(\frac{QD}{QD_o}\right)^{M(r)} \tag{3}$$

where M(r) considers the length of the overlap period in years (n_o), as well as the correlation coefficient (r) of annual low flows and, can be calculated using Eq. (4).

$$M(r) = \frac{(n_o-3).r^3}{(n_o-4).r^2+1} \tag{4}$$

3.3 Evaluation of Methods Performance

To define the most applicable method between the spatial regionalization and the temporal regionalization methods, the scatter plot between observed and predicted LFI for each method will be constructed and the statistical indicators including coefficient of determination (R^2), root-mean-square error (RMSE) and Nash-Sutcliffe efficiency (NSE) will be calculated to define which method is the most applicable for this study.

3.3.1 Nash-Sutcliffe Efficiency

The Nash-Sutcliffe efficiency is a normalized statistic that determines the relative magnitude of the residual variance compared to the measured data variance. NSE indicates how well the plot of observed versus predicted LFI fits the 1:1 line (Moriasi et al., 2007). NSE can be computed by using Eq. (5).

$$NSE = 1 - \left[\frac{\sum_{i=1}^{n}(O_i-P_i)^2}{\sum_{i=1}^{n}(O_i-\bar{O})^2}\right] \tag{5}$$

where O_i is i^{th} observed low-flow indices, P_i is i^{th} predicted low-flow indices, $\bar{O}$ is mean of observed low-flow indices, and n is total number of observations.

3.3.2 Root-Mean-Square Error

The root-mean-square error is the square root of the mean of the square of all the errors. It is considered as an excellent general-purpose error metric for numerical predictions. RMSE is a good measure of accuracy, but only to compare prediction errors of different models or model configurations for a particular variable and not between variables, as it is scale-dependent (Neill & Hashemi, 2018). It can be computed by using Eq. (6).

$$RMSE = \sqrt{\frac{1}{n}\sum_{i=1}^{n}(O_i - P_i)^2} \tag{6}$$

3.3.3 Coefficient of Determination

The coefficient of determination is the criterion generally used in the linear regression to test the adjustment of the model (Ait-Amir et al., 2020) and can be calculated by using Eq. (7).

$$R^2 = \left[\frac{\sum_{i=1}^{n}(O_i-\bar{O})\times(P_i-\bar{P})}{\sqrt{\sum_{i=1}^{n}(O_i-\bar{O})^2}\times\sqrt{\sum_{i=1}^{n}(P_i-\bar{P})^2}}\right]^2 \quad (7)$$

where $\bar{P}$ is predicted low-flow indices

4. RESULTS AND DISCUSSIONS

The results are divided into three parts including the estimation of the observed and regionalized low-flow indices.

4.1 Low-flow Indices

4.1.1 Ninety-five-percentile Flow (Q95)

Figure 3 illustrates the flow duration curves (FDCs) of the 25 flow stations used in this study. It can be seen from Figure 3 that FDCs developed from the three located mainstream stations namely P.73, P.1, and P.67 indicate much higher flows for overall compared to the others. The Q95 of the 25 flow stations are then determined from the FDCs.

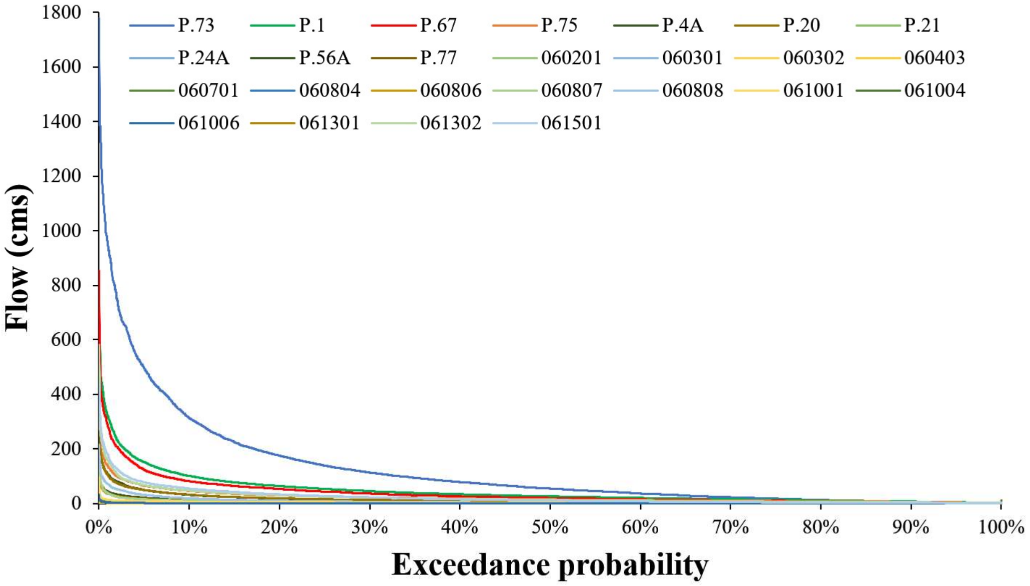

Figure 3 FDCs of the 25 selected flow stations

4.1.2 Baseflow Index

Figure 4 demonstrates the baseflow lines of the 25 selected flow stations. Similar to the FDC, the baseflow line developed from the three located mainstream stations namely P.73, P.1, and P.67 indicate much higher flows for overall comparing to the others. The plot also depicts that the daily baseflow in the 25 sub-basins has a similar pattern, but they are different in amount. The BFIs are then defined as the baseflow volume divided by the total streamflow volume.

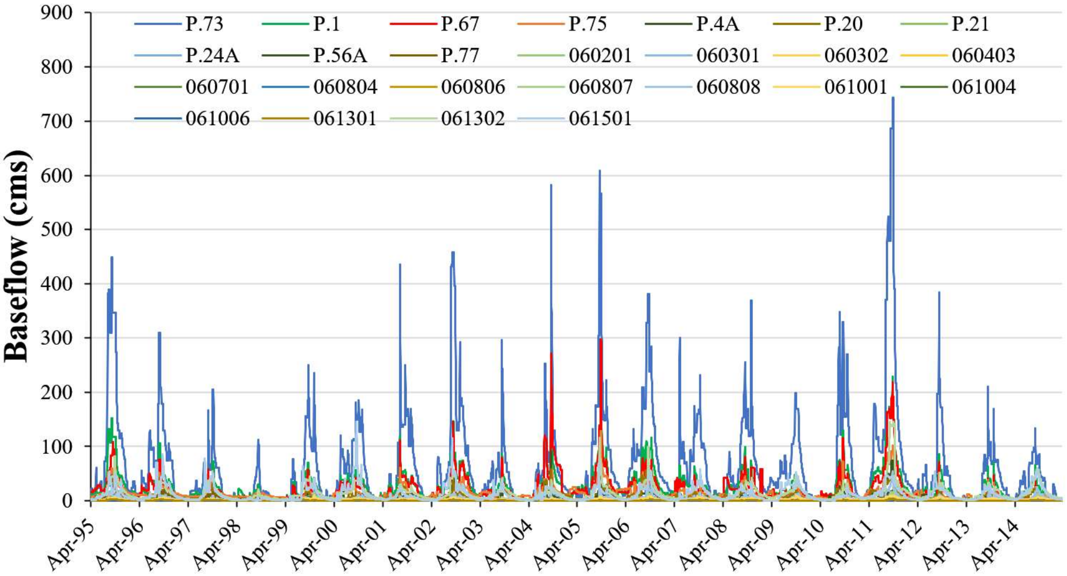

Figure 4 Baseflow hydrograph of the 25 flow stations

4.1.3 Annual Minimum 7-day Moving Average Flow with a 10-year Recurrence Interval

Figure 5 shows the 7-day moving average flow of the 25 selected flow stations. The plot is much similar to that of the baseflow hydrograph. However, they are different in terms of quantity. The 7-day minimum average flows determined from streamflow time series are fitted to a Log-Pearson Type III distribution to determine 7Q10. The result indicates that the three located mainstream stations (P.73, P.1, and P.67) mentioned above keep showing higher values. Moreover, station P.75 located upstream of the three stations is also found to present a significantly higher value of 7Q10 compared to the others.

The estimated LFI of all the 25 flow stations can be summarized as shown in Table 2

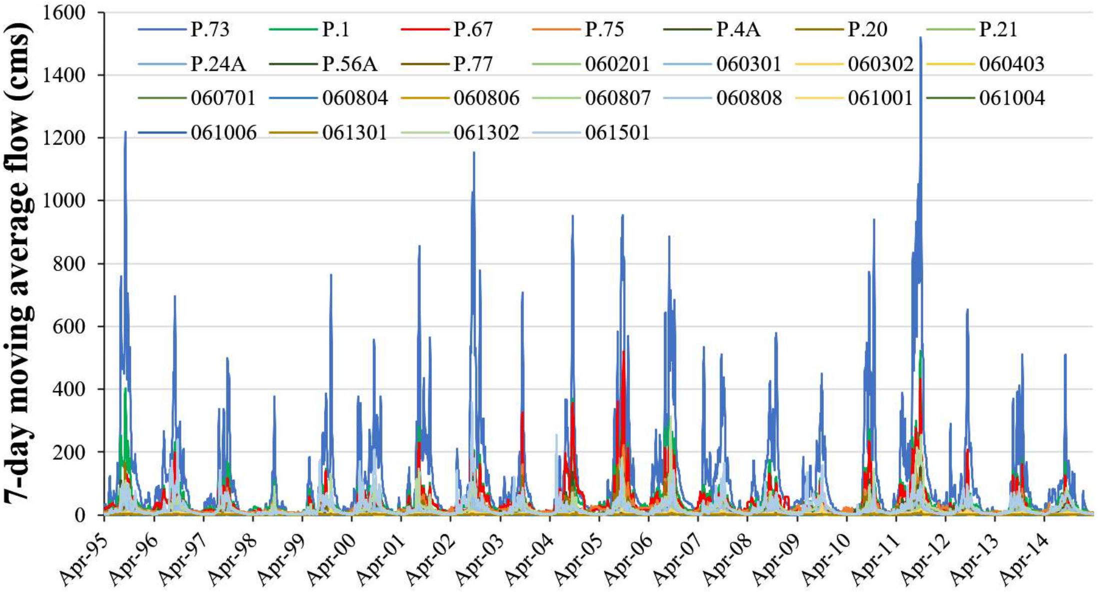

Figure 5 7-day moving average flow of the 25 stations

Table 2 The average LFI of the 25 sub-basins

No.	Station	Q95	BFI	7Q10	No.	Station	Q95	BFI	7Q10
1	P.1	4.60	0.58	10.21	14	060403	0.11	0.81	0.19
2	P.4A	0.12	0.41	0.50	15	060701	0.12	0.60	0.18
3	P.20	0.96	0.57	2.49	16	060804	0.06	0.51	0.12
4	P.21	0.15	0.48	0.41	17	060806	0.21	0.45	0.43
5	P.24A	0.21	0.45	0.52	18	060807	0.88	0.59	1.39
6	P.56A	0.31	0.49	0.83	19	060808	0.22	0.42	0.42
7	P.67	3.44	0.56	7.53	20	061001	0.70	0.73	0.93
8	P.73	0.96	0.53	12.98	21	061004	0.11	0.66	0.18
9	P.75	4.23	0.63	8.58	22	061006	0.10	0.58	0.16
10	P.77	0.01	0.52	1.53	23	061301	0.11	0.73	0.27
11	060201	0.11	0.67	0.23	24	061302	3.48	0.67	4.51
12	060301	0.26	0.65	0.45	25	061501	1.20	0.54	1.82
13	060302	0.11	0.65	0.15					

4.2 Regional Regression Method

4.2.1 Correlation between LFI and Each Independent Basin Characteristics

To investigate the possibility of using the regression to represent the relationship between the basin characteristics and the LFI, a matrix of scatter plots between each basin characteristic and each LFI was developed, and the correlation coefficient (r) is computed.

The results show that r of the Q95 ranges from -0.30 to 0.74. The %W and Sl_{max} are the descriptors with the highest r equal to 0.74 and 0.63, respectively. The r of the BFI ranges from -0.48 to 0.50. The El_{min} and Sl_{mean} seem to be most informative in predicting BFI with r equal to 0.50 and 0.49, respectively. For the 7Q10, r ranges from -0.57 to 0.91 where the Ar, %W, Sl_{max}, and %G62 are descriptors with relatively high r equal to 0.91, 0.90, 0.77, and -0.57, respectively. A few descriptors with high r values suggest the possibility of using the regression as the LFI can be explained by some of the informative basin characteristics.

4.2.2 Regression Equations

Based on the stepwise regression approach with the allowable p-value of 0.05, only three standardized basin characteristics namely proportions of agriculture (%A), forest (%F), and open water (%W) show a significant relationship for predicting the Q95. The regression equation which relates the three descriptors to the predicted Q95 is as shown in Eq. 8. The presence of the three sub-basin descriptors tends to increase the value of Q95 in each sub-basin. The result indicates that the regression equation yields a better R^2 and NSE of 0.78 with a moderate RMSE of 0.51 as shown in Figure 6(a).

$$Q95_{pred} = 2.20\%A + 2.63\%F + 1.18\%W \quad (8)$$

In the prediction of BFI, there are three standardized basin characteristics namely minimum elevation (El_{min}), mean slope (Sl_{mean}), and proportion of soil type group 60 (%G60) which share substantial contribution to the prediction. The regression equation which relates the three basin characteristics to the predicted BFI is as shown in Eq. 9. The presence of El_{min}, and Sl_{mean} tends to increase the amount of BFI while the presence of %G60 tends to decrease the amount of BFI in each sub-basin. The result shows that the equation yields a moderate R^2 and NSE of 0.58 with a high RMSE of 0.70 as shown in Figure 6(b).

$$BFI_{pred} = 0.43El_{min} + 0.37Sl_{mean} - 0.34\%G60 \quad (9)$$

The regression equation for predicting 7Q10 consists of four standardized basin characteristics namely area (Ar), proportions of agriculture (%A), forest (%F) and open water (%W) as shown in Eq. 10. The presence of the four descriptors tends to increase the amount of 7Q10 in each sub-basin. The result indicates that the equation yields a high R^2 and NSE of 0.95 with a low RMSE of 0.26 as shown in Figure 6(c).

$$7Q10_{pred} = 0.61Ar + 0.74\%A + 0.90\%F + 0.58\%W \quad (10)$$

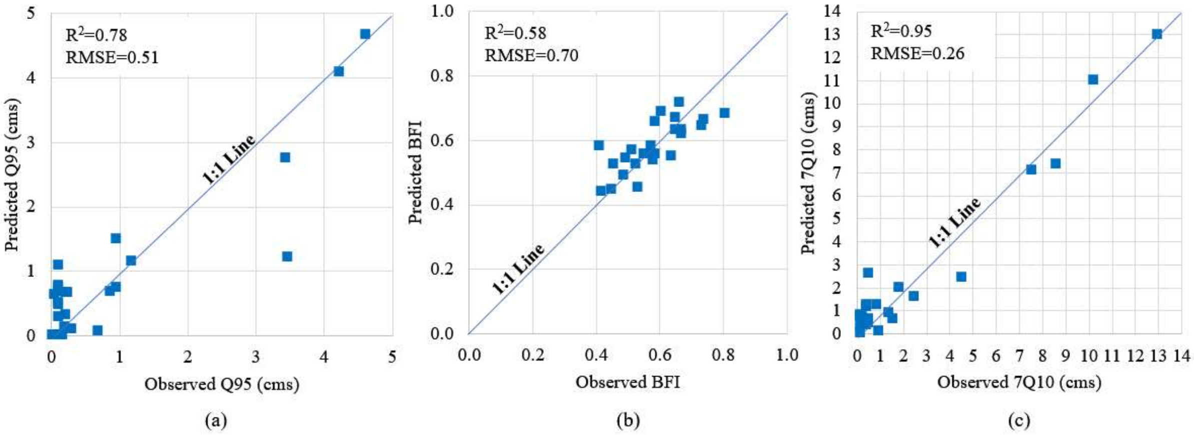

(a) (b) (c)

Figure 6 Predicted LFI estimated from regional regression method plotted versus Observed LFI estimated from overall 20-yr period: (a) Q95, (b) BFI, (c) 7Q10

To test the reliability of the regression model, the regression method was applied separately to calibration (2000-2014) and validation (1995-1999) periods. The regression method gives acceptable performance for Q95 and 7Q10 but not BFI. For Q95, the values of R^2, NSE, and RMSE are similar for both calibration and validation periods. When moving from calibration to validation period, a drop in performance of the 7Q10 is caused by an outlier. While further investigation of the outlier should have been done, it is beyond the scope of this study. The regression equation for BFI shows the worst performance for both calibration and validation periods. The results of reliability test are provided in Figure 7 and it can be concluded that the regression model is applicable for predicting low-flow indices but with variable performance.

4.3 Climate Adjustment Method

The climate adjustment method can be applied using different overlap periods. The effects of different overlap periods with different base years are investigated in the prediction. A sample of the Q95 which is predicted from various overlap periods of 1-yr, 5-yr, 10-yr, and 15-yr with the base year of 1995 is assessed using both augmentation techniques and can be plotted versus the observed Q95 estimated from the overall 20-yr period as shown in Figure 8. The results indicate that the appropriate length of overlap period is necessary for the prediction to obtain a reliable result. The figure clearly shows that for the overlap period of 1-yr, the prediction using the 1st technique performs better than the 2nd technique. However, for the overlap period of 5 years or more, the 2nd technique shows better performance overall.

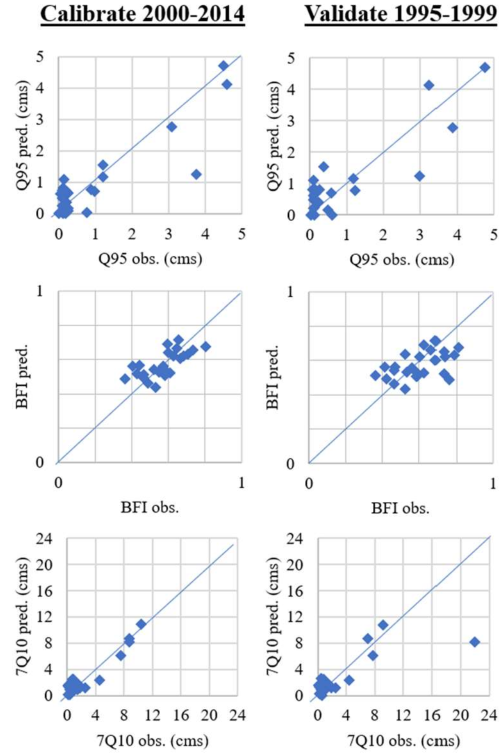

Summary results

Q95	Calibrate	Validate
RMSE (cms)	0.65	0.66
R^2	0.78	0.76
NSE	0.78	0.75

BFI	Calibrate	Validate
RMSE	0.08	0.11
R^2	0.49	0.25
NSE	0.49	0.18

7Q10	Calibrate	Validate
RMSE (cms)	0.95	2.96
R^2	0.92	0.68
NSE	0.92	0.65

Figure 7 Performance of the regression model in calibration and validation periods

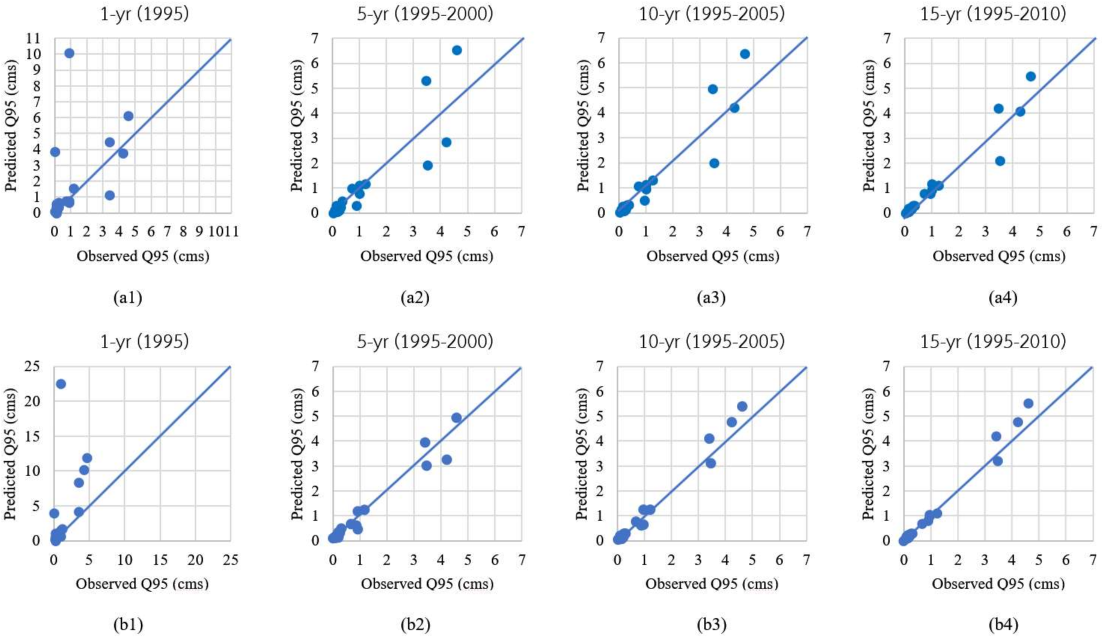

Figure 8 Adjusted $Q95_{pred}$ estimated from: (a1) 1-yr (1995), (a2) 5-yr (1995-2000), (a3) 10-yr (1995-2005), (a4) 15-yr (1995-2010) records using 1st technique plotted versus $Q95_{obs}$ estimated from overall 20-yr period; and Adjusted $Q95_{pred}$ estimated from: (b1) 1-yr (1995), (b2) 5-yr (1995-2000), (b3) 10-yr (1995-2005), (b4) 15-yr (1995-2010) records using 2nd technique plotted versus $Q95_{obs}$ estimated from overall 20-yr period

Figure 9 shows the summary of the method performance for the prediction of Q95 using both techniques with different overlap periods and base years. In the 1st technique, for 1-year overlap period, the method shows unsatisfied performance with very poor statistical indicators. For 5 years, the method yields R^2 range from 0.42 to 0.92, NSE range from -0.33 to 0.90, and RMSE range from 0.43 to 1.58. For 10 years, the method yields R^2 range from 0.72 to 0.97, NSE range from 0.69 to 0.96, and RMSE range from 0.28 to 0.77 while for 15 years, the method yields R^2 range from 0.89 to 1.00, NSE range from 0.89 to 0.99, and RMSE range from 0.25 to 0.62.

In the 2nd technique, for 5 years, the method yields R^2 range from 0.67 to 0.98, NSE range from -1.02 to 0.96, and RMSE range from 0.27 to 1.95. For 10 years, the method yields R^2 range from 0.90 to 0.98, NSE range from 0.79 to 0.97, and RMSE range from 0.25 to 0.62 while for 15 years, the method yields R^2 range from 0.98 to 1.00, NSE range from 0.96 to 1.00, and RMSE range from 0.09 to 0.27.

The summary of the BFI and 7Q10 is as shown in Figure 10 and Figure 11, respectively.

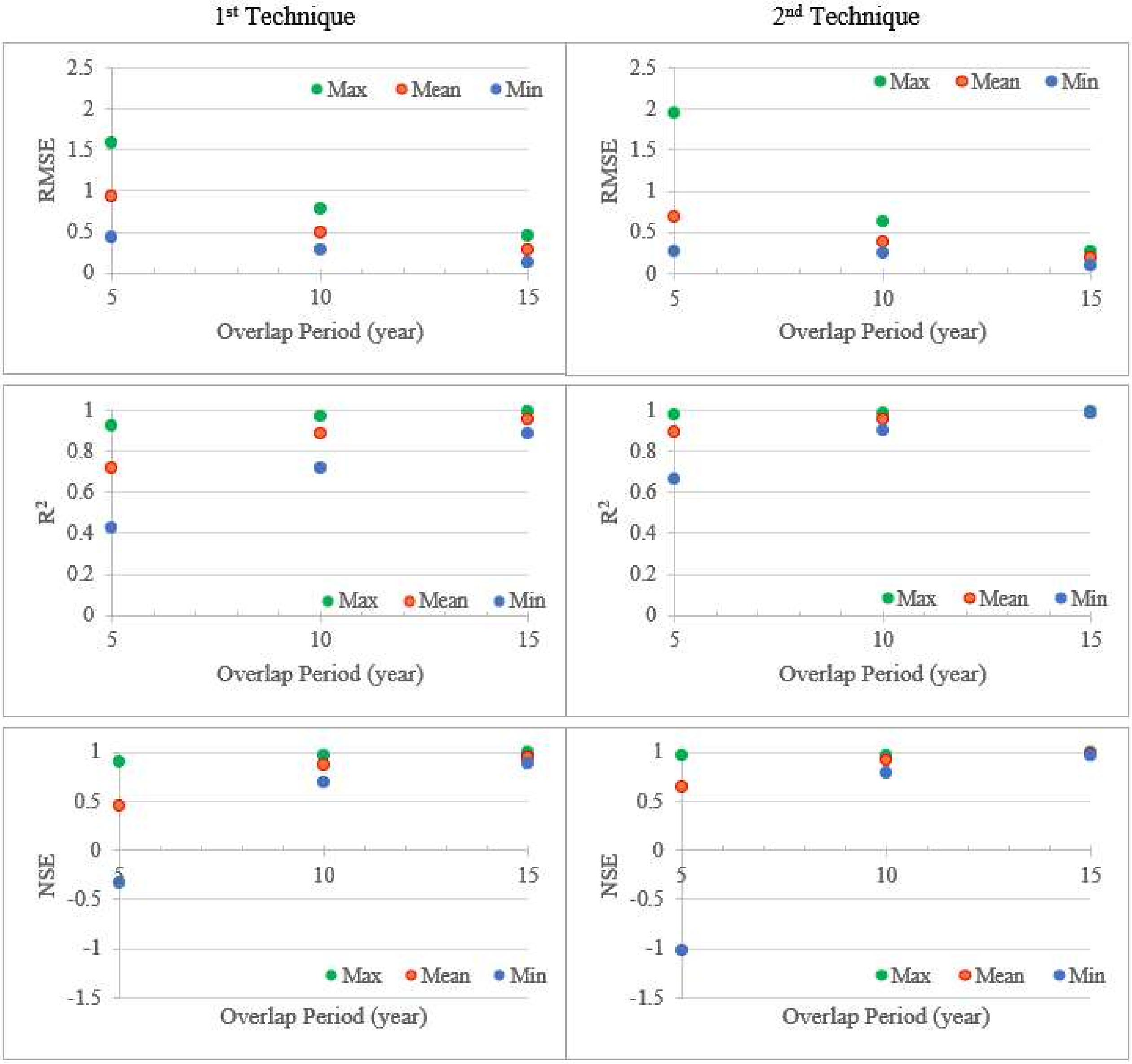

Figure 9 Summary of climate adjustment method performance of two augmentation techniques for Q95

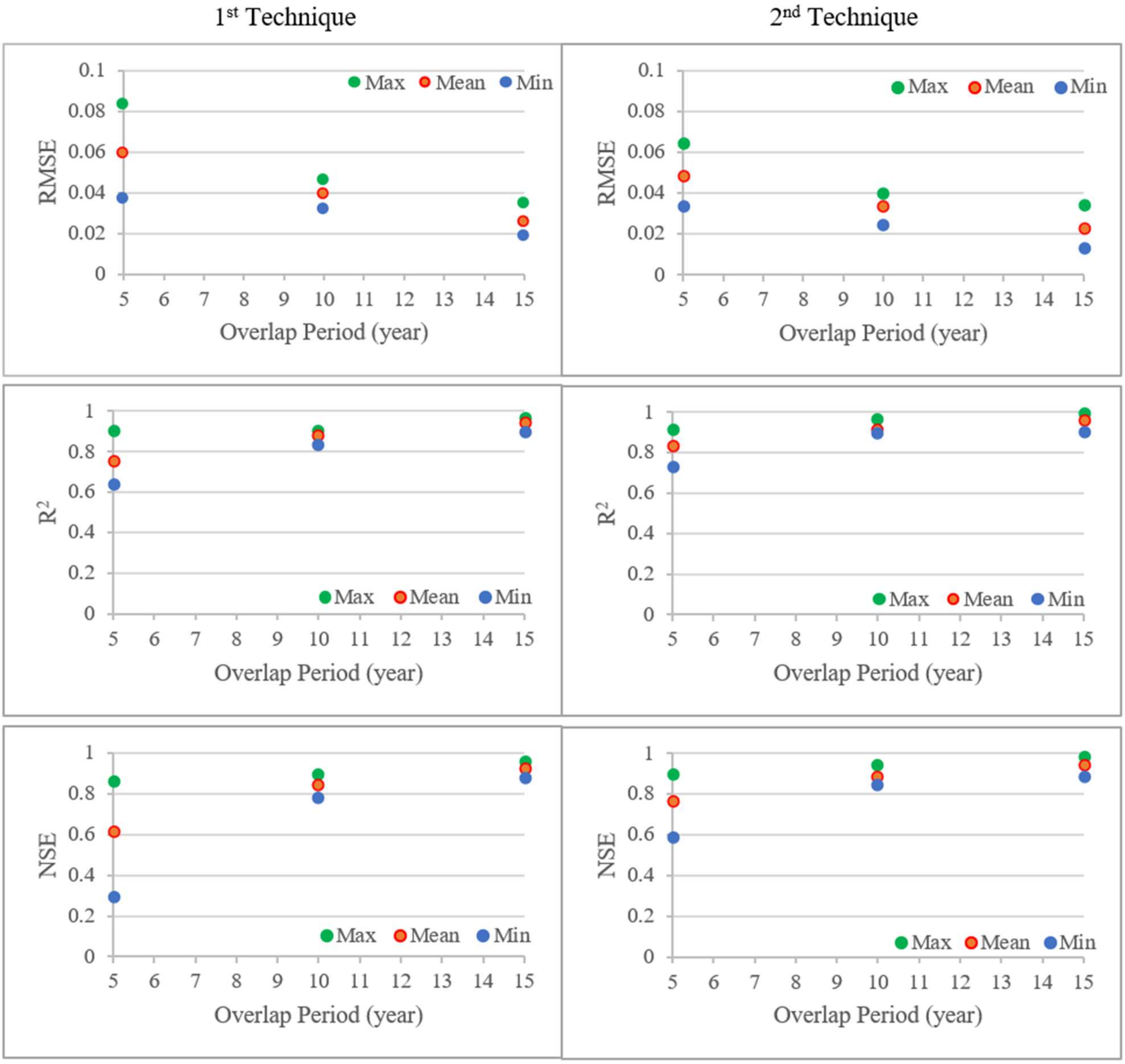

Figure 10 Summary of climate adjustment method performance of two augmentation techniques for BFI

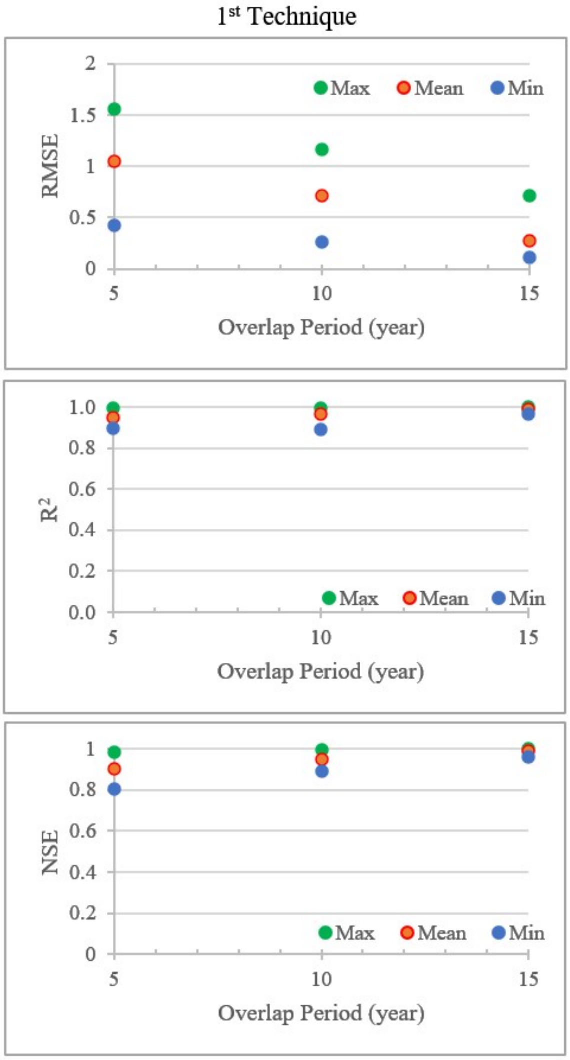

Figure 11 Summary of climate adjustment method performance using 1st techniques for 7Q10

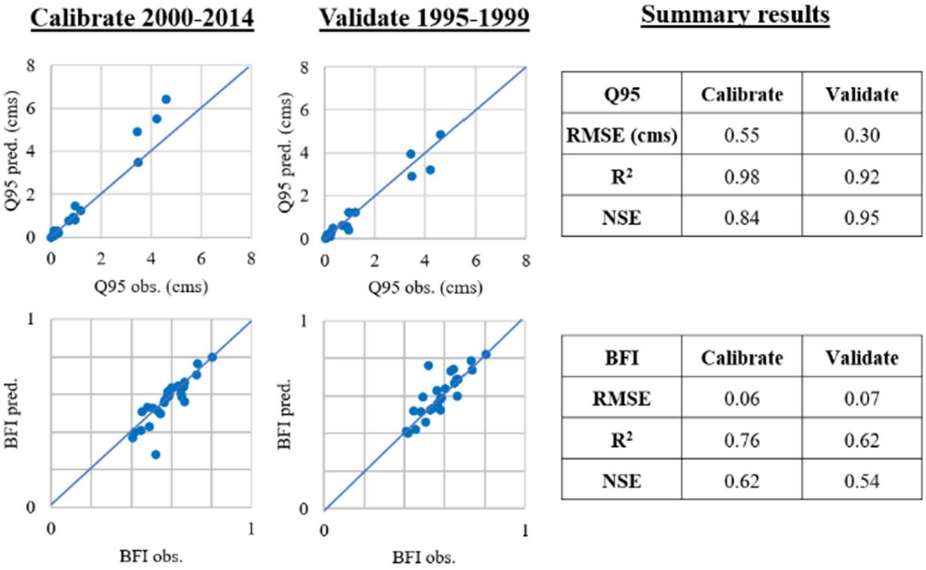

Q95	Calibrate	Validate
RMSE (cms)	0.55	0.30
R²	0.98	0.92
NSE	0.84	0.95

BFI	Calibrate	Validate
RMSE	0.06	0.07
R²	0.76	0.62
NSE	0.62	0.54

Figure 12 Performance of the 2nd technique of the climate adjustment method in calibration and validation periods

Figure 12 shows the results of reliability test when the 2nd technique of the climate adjustment method is used for calibration and validation period. The method can yield a reliable performance since the values of R^2, NSE, and RMSE in validation period are comparable to those of the calibration period. This supports the applicability of the climate adjustment method for estimating low-flow indices in ungauged basins.

5. CONCLUSIONS

The assessment of low-flow in ungauged basins remains a challenging issue especially for developing countries where the flow gauging network is limited. Regionalization using the regression and climate adjustment methods was found to be applicable to the prediction of low-flow in the Upper Ping River basin which is the study area. Generally, the climate adjustment method outperforms the regression method as it yielded better values for performance indices. The improved performance obtained from the climate adjustment method is probably due to being contribution from the consideration of the variation in climate over 20 years of the study period. The longer overlap period used for climate adjustment, the better the performance. However, the marginal increase in the performance is less seen when using the overlap period longer than 10 years. The 2nd technique of the climate adjustment method where the weighting coefficient was applied further improves the performance over its 1st technique. The framework demonstrated in this study could be used as a guideline to regionalize low-flow indices and estimate streamflow in other ungauged basins with similar climate regime and hydrological context. This would help address the issue of water scarcity and improve water resources management in ungauged basins.

6. ACKNOWLEDGMENT

The authors would like to thank the Royal Irrigation Department and Department of Water Resources for providing the data for this study. We also would like to thank the reviewers for their comments to improve this manuscript.

7. REFERENCES

Ait-Amir, B., Pougnet, P., & El Hami, A. (2020). Meta-Model Development. In *Embedded Mechatronic Systems 2* (pp. 157-187). Elsevier.

Eslamian, S. (2018). *Handbook of Engineering Hydrology (Three-Volume Set)*. CRC Press. https://books.google.co.th/books?id=I2G1DwAAQBAJ

Karamouz, M., Szidarovszky, F., & Zahraie, B. (2003). *Water resources systems analysis*. CRC Press.

Kundzewicz, Z. W. (1997). Water resources for sustainable development. *Hydrological Sciences Journal, 42*(4), 467-480.

Laaha, G., & Blöschl, G. (2005). Low flow estimates from short stream flow records—a comparison of methods. *Journal of Hydrology, 306*(1-4), 264-286.

Laaha, G., Hisdal, H., Kroll, C., Van Lanen, H., Nester, T., Rogger, M., Sauquet, E., Tallaksen, L., Woods, R., & Young, A. (2013). Prediction of low flows in ungauged basins. In *Run-off Prediction in Ungauged Basins, Synthesis across Processes, Places and Scales* (pp. 163-188). Cambridge University Press.

Moriasi, D. N., Arnold, J. G., Van Liew, M. W., Bingner, R. L., Harmel, R. D., & Veith, T. L. (2007). Model evaluation guidelines for systematic quantification of accuracy in watershed simulations. *Transactions of the ASABE, 50*(3), 885-900.

Nathan, R. J., & McMahon, T. A. (1992, June 01). Estimating low flow characteristics in ungauged catchments [journal article]. *Water Resources Management, 6*(2), 85-100. https://doi.org/10.1007/bf00872205

Neill, S. P., & Hashemi, M. R. (2018). *Fundamentals of ocean renewable energy: generating electricity from the sea*. Academic Press.

Riggs, H. C. (1972). *Low-flow investigations*. US Government Printing Office.

Sharma, D., & Babel, M. S. (2014). Trends in extreme rainfall and temperature indices in the western Thailand. *International Journal of Climatology, 34*(7), 2393-2407.

Smakhtin, V. U. (2001). Low flow hydrology: a review. *Journal of Hydrology, 240*(3-4), 147-186.

Visessri, S. (2014). *Flow prediction in data scarce catchments: A case study of Northern Thailand* Imperial College London].

Visessri, S. & McIntyre, N. (2015). Regionalisation of hydrological responses under land-use change and variable data quality. *Hydrological Sciences Journal, 61*(2), 302-320.

White, K. E., & Sloto, R. A. (1990). *Base-flow frequency characteristics of selected Pennsylvania Streams* (Vol. 90). US Department of the Interior, US Geological Survey.

WMO. (2008). *Manual on Low-flow Estimation and Prediction*. World Meteorological Organization. https://books.google.co.th/books?id=A5YiQwAACAAJ

Zelenhasić, E., & Salvai, A. (1987). A method of streamflow drought analysis. *Water resources research, 23*(1), 156-168.

NUEJ
Naresuan University
Engineering Journal

The Microwave Pretreatment Effects on Yield and Tocopherol Content of Cold-Pressed Sesame Oil

Patomsok Wilaipon

Mechanical Engineering Department, Engineering Faculty, Naresuan University, Phitsanulok, Thailand

Corresponding author e-mail: patomsok@hotmail.com

(Received: 20 June 2022, Revised: 6 December 2022, Accepted: 19 December 2022)

Abstract

The benefits of black sesame have long been recognized, and black sesame has been used for consumption, cosmetics for hair and skin care, and medication. One process used to produce high quality black sesame oil is the cold pressed process, where temperature is controlled to be lower than 60 ºC throughout the process. However, this process results in a lower yield than extraction by solvent. Therefore, with the aim of enhancing efficiency, this study is examining the impact of a microwave pretreatment on the output of cold pressing black sesame oil. The experiment tested three conditions, with different microwave wattages and pretreatment durations, while temperatures were controlled slightly below 60 ºC under all conditions. The effects of microwave pretreatment on seed color and weight loss profile of black sesame were studied. Tocopherol, one of the significant compounds of sesame oil, was also examined. It was found that under all conditions, microwave pretreatment increased yields from black sesame cold pressing by 8% relative to pressing with no pretreatment. In addition, higher $\gamma+\beta$ tocopherolin levels were found in the black sesame oil extracted after the pretreatment process, and the highest $\gamma+\beta$ tocopherol levels were found after using low microwave wattage with a longer duration of pretreatment. It was also found that the weight loss rate of black sesame seed increased as the microwave power was increased. Besides, as compared to the non-activated one, 180 W sesame seed showed the highest value of color difference.

Keywords: Cold Pressed Oil, Sesame Oil, Tocopherol, Cold Press Extraction, Microwave Pretreatment

1. INTRODUCTION

Black sesame is a plant with economic value. It is widely consumed, especially in Asia where black sesame has been used for medicine and cosmetics for some time. There are reports of the grain's medicinal benefits, such as its antioxidant and anti-inflammatory properties, as well as its capacity to lower lipid levels in the blood. There is also evidence that consuming black sesame oil for 45 days can reduce hypertension and lipid peroxidation, while helping to increase the antioxidant status of hypertensive patients between 35–60 years old (Sankar et al., 2006). Black sesame is a rich source of nutrition with high levels of biologically active compounds, such as omega-3, tocopherol, sesamin, and sesamolin (Rangkadilok et al., 2010; Gharby et al., 2017; Dogruer et al., 2021). Additionally, sesaminol diglucoside, an antioxidant derived from sesame seed cake, was studied (Nantarat et al., 2020; Eom et al., 2021).

Oil extraction by solvent is one of the most effective processes of extracting oil from plant seeds. However, this process has many disadvantages, especially the quality of the oil products, which is lower because of the high temperature and the numerous procedures that must be applied during extraction. Mechanical press oil extraction, on the other hand, is commonly used for extracting plant oil, is simpler, and can produce higher quality oil products. One reason for this is that it uses a lower temperature in production, especially during the cold-pressed process where temperature is kept below 60 ºC. However, mechanical press oil extraction results in a large quantity of remaining oil in the seed waste, indicating low production efficiency. Therefore, applying a pretreatment method prior to extraction aims to reduce the quantity of leftover oil in the seed waste. One of the pretreatment processes conducted to successfully extract most of the oil from the seeds is to use microwave radiation to activate the seeds prior to oil extraction. For example, the production efficiency of purslane seeds that have undergone 400 W microwave radiation is increased by 6% (Hosseini et al., 2017). Gac aril activated by 630 W microwave radiation results in the most efficient production and the highest preservation of beta-carotene and lycopene levels (Kha et al., 2013). In Chilean hazelnut extraction, 400–600 W microwave radiation significantly increases production efficiency relative to hazelnut extraction without microwave activation (Uquiche et al., 2008). Pretreatment of rapeseed using 800 W microwave radiation can increase extraction efficiency relative to rapeseed that has not undergone pretreatment (Wroniak et al., 2016). In addition, activation of rice bran by microwave prior to oil extraction has been shown to be more efficient than activation using steaming, but less efficient than activation using hot air (Thanonkaew et al., 2012).

The findings from the aforementioned studies provide evidence for microwave radiation's impact on activating black sesame seeds prior to using them in a cold-pressed process and for the relative efficiency of oil production when using activated seeds compared to seeds that have not been activated. Since tocopherol is a significant compound of sesame oil, the present study also measured the amount of tocopherol in cold-pressed black sesame oil where the microwave pretreatment method had been applied and compared it to levels found in oil from unprocessed seeds. Therefore, the purpose of this study was to determine how the microwave pretreatment of black sesame affected its yield and tocopherol content. Additionally, the variation in color of microwave-activated sesame was also investigated.

2. MATERIAL AND METHOD

The black sesame used in this study originated from raw sesame grown in Thailand. The sesame was kept in a sealed plastic bag and had never been opened before the experiment. The material was kept in storage with a controlled temperature of 25–30 ºC. The procedure required the use of an oil pressing unit, which was a cylinder-shaped iron device with a 20-mm inner diameter, a 30-mm outer diameter, and a 70-mm height. The underside had 13 drainage holes, each hole with a 1-mm diameter. The outer part of the tube was equipped with a 220V 150W band heater, used to heat up the cylinder as shown in Figure 1. Temperature measurements and the operation of the heater were controlled by the type K thermocouple with PID Temperature Controller (MaxWell, MTB series). A universal testing machine (UTM: Housefield: H50KS) was used as the starting power of the oil pressing.

For evaluating the weight loss profile of microwave pre-treatment, 10 grams of sesame seed were placed into an 800-W microwave for 360 seconds. Using a digital balance, an Ohaus balance with 0.01 g precision, the weight of the sesame was measured every 30 seconds for 360 seconds. The effects of microwave radiation at three different intensities were studied: 100, 180, and 300 watts. The color of the sesame was then measured using a WR-10QC handheld colorimeter, CIELAB $L^*a^*b^*$ colorimeter system. The color difference between activated and non-activated sesame was computed using the equation below.

$$\Delta E = \sqrt{(L_1^* - L_2^*)^2 + (a_1^* - a_2^*)^2 + (b_1^* - b_2^*)^2} \quad (1)$$

Where

ΔE is the colour difference,

L^* is the lightness coordinate,

a^* is the red/green coordinate, with $+a^*$ indicating red and $-a^*$ indicating green,

b^* is the yellow/blue coordinate, with $+b^*$ indicating yellow and $-b^*$ indicating blue.

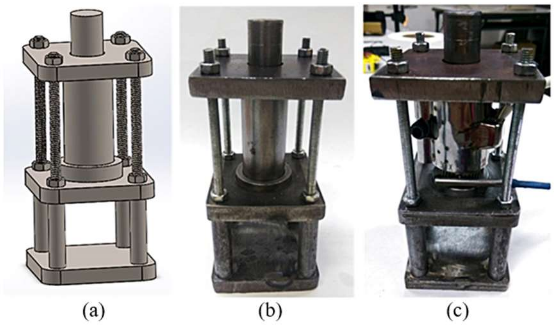

Figure 1 Cold pressed piston-cylinder set (a) drawing (b) cylinder set (c) cylinder set with electric heater

Ten grams of black sesame were baked and activated by microwave radiation. An 800 W 2450 Hz microwave was used, with electric power and duration set at 100 W-330 s, 180 W-150 s, and 300 W-60 s, respectively. The black sesame activated using this method had a temperature slightly lower than 60 ºC, which is the controlled temperature required for the cold pressing process. Subsequently, the treated black sesame was loaded into the cylinder equipped with a nylon filter, and the press speed of the UTM machine was set at 1 mm min^{-1}. The press of the UTM was paused for 10 min and the amount of sesame oil produced from the process was measured. Each different condition was tested 3 times with the pressing temperature at 60 ºC and the pressure at 70 MPa throughout the experiment.

Tocopherol levels in the treated sesame oil were measured using an HPLC machine and then were compared to the amount of tocopherols already known to be in a standard sample. The measurement process was initiated by dissolving the extracted sesame oil with isopropanol. After that, it was filtered through a 0.45-micron filter and injected into the HPLC machine, SHIMADZU (Japan) model Class-VP with specifications Detector: RF-10A XL Fluorescence Detector (EX 290 and EM 330 nm) Ultra C18, 5 µm, 25 cm x 4.6 mm (Restek).

3. RESULT AND DISCUSSION

Figure 2 depicts the weight loss profile of black sesame after microwave pretreatment for 0 to 360 seconds. It has three different microwave power levels: 100, 180, and 300 W. The weight loss rates of 100, 180, and 300 W appear to be consistent from the beginning to 180 s: 0.027, 0.061, and 0.111 % per second, respectively. After that time, the graphs' slopes are somewhat reduced to 0.027, 0.033, and 0.025 % per second, respectively. As the microwave power level increased, it produced a higher value of the pressure difference between the surface and the inside of the seed, resulting in a higher weight loss rate (Younces et al., 2016).

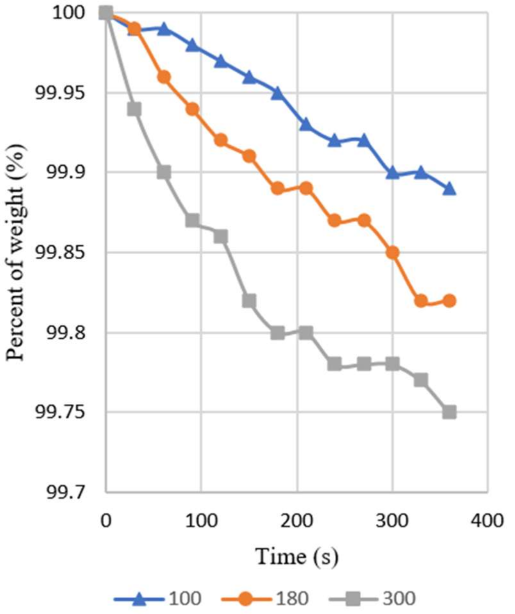

Figure 2 Percentage of remaining weight after microwave radiation

Figure 3 shows the color of black sesame after microwave pre-treatment. For 100 W microwave radiation, the *L**, *a**, and *b** values were found to be 13.71, 0.55, and 0.17, respectively. In comparison to the as-received sesame, the *L** value, lightness, was somewhat enhanced while the *a** and *b** values were decreased. These values were 13.22, 0.8, 0.09 for 180 W and 14.64, 0.35, 0.31 for 300 W, respectively. According to the calculations, when the microwave power increases, the color difference values, ΔE, increase. When compared to non-activated sesame, the ΔE values for 100, 180, and 300 W sesame were 0.29, 0.32, and 1.25, respectively.

The output of black sesame oil from the seeds that had undergone microwave-pretreatment extraction and the common seeds that had not undergone activation was 34.50–37.67% by weight. The yields from the black sesame seeds that had undergone microwave pretreatment at 100 W-330 s, 180 W-150 s, and 300 W-60 s showed a significant difference from yields from common seeds without microwave pretreatment, with a significance level at 95% at about 8% higher than common seeds, shown in Figure 4. The reason for increased yield may be the vaporization of seed moisture after microwave treatment. This causes an increase in pressure in the seed interior, leading to cell wall and membrane disruption, which facilitates the oil passage and affects the oil yield (Bose et al., 2020).

However, when comparing among the three microwave-pretreatment conditions, no statistical difference ($P < 0.05$) was found. The findings from this study are consistent with research in Chile (Uquiche et al., 2008) which found that activating hazelnuts by 400W and 600W microwave radiation prior to mechanical pressing for oil extraction increases yields from those of hazelnuts that have not undergone pretreatment. This is because the cell membrane of the seed is altered by the microwave radiation, which heats up the object from the inside. The present findings also relate to other studies (Wroniak et al., 2016; Bakhshabadi et al., 2017) which mention the use of microwave pretreatment resulting in membrane disruption and in an increase in oil extraction yields.

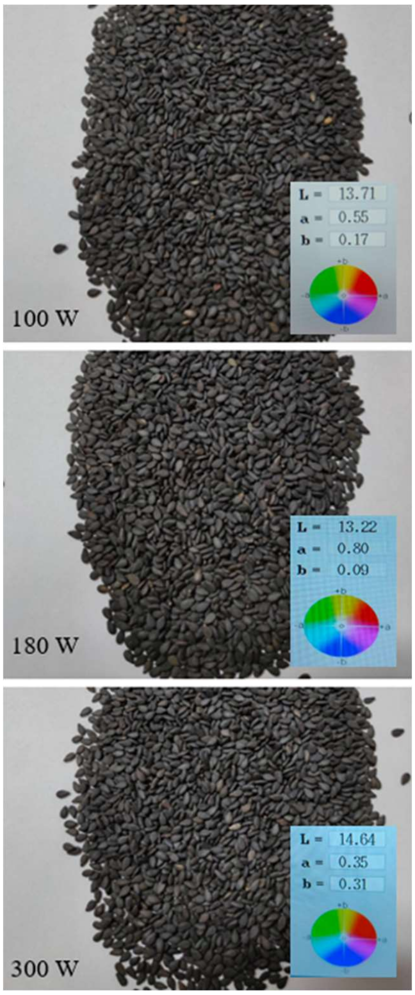

Figure 3 Sesame seed color after microwave pre-treatment

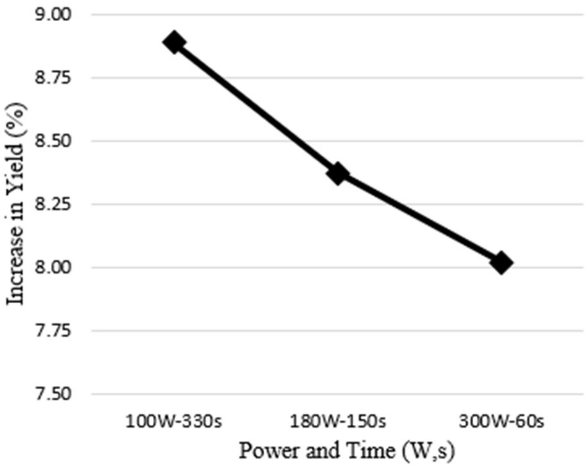

Figure 4 Increase in yield of pre-treatment sesame oil

High performance liquid chromatography separates the components of a liquid mixture by injecting the mixture into a stream of solvent flowing through a column packed with a separation medium. As the sample components separate from one another while flowing through the column, the detectors deliver a voltage response as a function of time, which is called a chromatogram. The moment each peak appears identifies the sample constituent with respect to a standard. The present study found γ+β tocopherol in every sample without α and δ tocopherol, as presented in Figure 5. This is consistent with other studies conducted in Thailand (Rangkadilok et al., 2010) which have reported that both types of tocopherols cannot be found in most black sesame. In Figure 5, when comparing tocopherol levels between the black sesame seeds that underwent microwave pretreatment at 100 W-330 s, 180 W-150 s, and 300 W-60 s with the controlled sample, or the common seeds that had not undergone microwave pretreatment, it was found that the seeds that had undergone microwave pretreatment had higher tocopherol levels than the controlled sample. The seeds that underwent pretreatment at a low wattage and for a longer time (100 W-330 s) had the highest tocopherol levels, followed by pretreatment conditions of 180 W-150 s and 300 W-60 s, respectively. These levels were higher than those observed in the corresponding controlled samples (20.33%, 17.47%, and 3.20%, respectively).

This result is consistent with a previous study on microwave pretreatment of kana rapeseed, which indicated that after a 7-min microwave treatment, α-tocopherolis levels decreased while γ and δ tocopherolis levels were found to be higher than rapeseed that had not undergone microwave treatment (Wroniak et al., 2016). Research on Sea Buckthorn leaves also found that γ tocopherol levels in microwave-dried samples were higher than those of samples which had undergone the conventional drying method (Gornas et al., 2014).

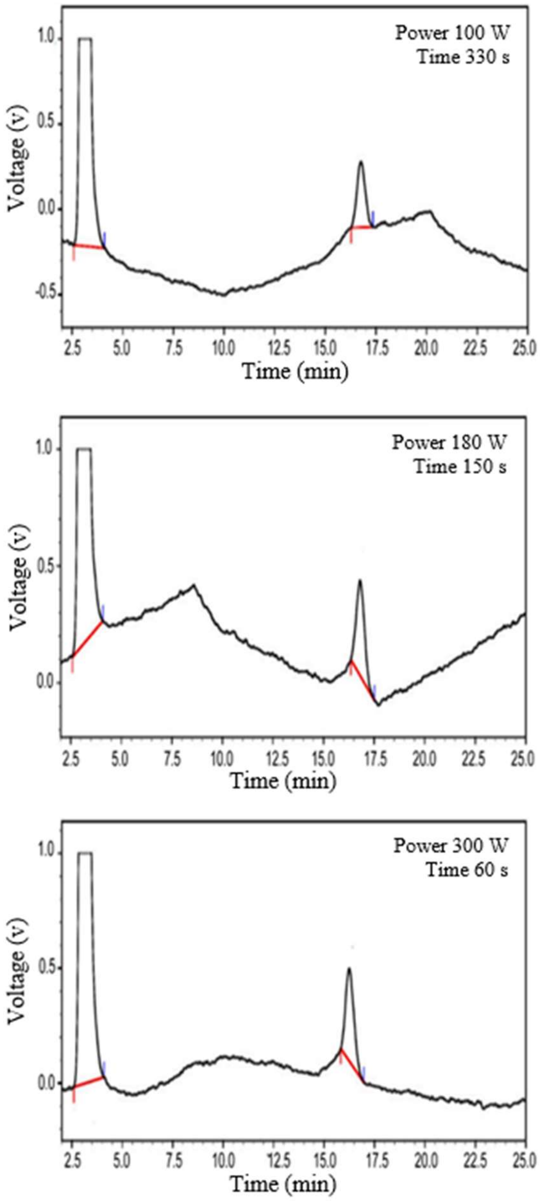

Figure 5 Tocopherol analysis result of pre-treatment sesame oil

4. CONCLUSION

This study investigated the impact of microwave pretreatment of black sesame on the seed's yield and on tocopherol levels in sesame oil extracted using the cold pressed process. The temperature was controlled to remain below 60 ºC throughout the process. The study found that this method can be applied prior to pressing oil from sesame in order to increase the yield from pressing. In terms of levels of the tocopherol compound, the study showed that pretreatment at all tested electrical powers and durations was able to increase the yield from the cold pressing process about 8%, with no statistically significant differences between the different conditions of pretreatment. Regarding levels of γ+β tocopherol in the cold pressed oil, using the microwave at a low wattage and with longer pretreatment duration at a temperature under 60 ºC yielded the highest levels of tocopherol, 20.33%, compared to other pretreatment conditions. Besides, the sesame seed that underwent 180 W of microwave treatment showed the highest value of color difference.

5. ACKNOWLEDGMENT

This research work was financially supported by Engineering Faculty, Naresuan University.

6. REFERENCES

Bakhshabadi, H., Mirzaei, H., Ghodsvali, A., Jafari, S. M., Ziaiifar, A. M. & Farzaneh, V. (2017). The effect of microwave pretreatment on some physico-chemical properties and bioactivity of black curmin seed's oil. *Industrial Crops and Products,* 97, 1–9. http://dx.doi.org/10.1016/j.indcrop.2016.12.005

Bose, P., Pradhan, D., Sonawane, A., Pathak, S. S., Anupriya, S. & Pradhan, R. C. (2020). Optimization of hot air and microwave pretreatment for enhancing the mechanical expression yield of Simarouba glauca oil. *J. Agric. Res*., 2, 100024. https://doi.org/10.1016/j.jafr.2020.100024

Dogruer, I., Uyar, H. H., Uncu, O. & Ozen, B. (2021). Prediction of chemical parameters and authentication of various cold pressed oils with fluorescence and mid-infrared spectroscopic methods. *Food Chem*., 345, 128815. https://doi.org/10.1016/j.foodchem.2020.128815

Eom, S. J., Zu, H. D., Lee, J., Kang, M. C., Park, J., Song, K. M. & Lee, N. H. (2021). Development of an ultrasonic system for industrial extraction of unheated sesame oil cake. *Food Chem*., 354, 129582. https://doi.org/10.1016/j.foodchem.2021.129582

Gharby, S., Harhar, H., Bouzoubaa, Z., Asdadi, A., Yadini, A. E. & Charrouf, Z. (2017). Chemical characterization and oxidative stability of seeds and oil of sesame grown in Morocco. *Journal of Saudi Society of Agricultural Sciences,* 16, 105–111. https://doi.org/10.1016/j.jssas.2015.03.004

Gornas, P., Sne, E., Siger, A. & Seglina, D. (2014). Sea buckthorn (hippophae rhamnoides L.) leaves as valuable source of lipophilic antioxidants: the effect of harvest time, sex, drying and extraction methods. *Industrial Crops and Products,* 60, 1–7. http://dx.doi.org/10.1016/j.indcrop.2014.05.053

Hosseini, S. D., Nayebzadeh, K., Mirmoghtadaie, L., Kavosi, M. & Hosseini, S. M. (2017). Effect of extraction process on composition, oxidative stability and rheological properties of purslane seed oil. *Food Chem.,* 222, 61–66. http://dx.doi.org/10.1016/j.foodchem.2016.11.150

Kha, T. C., Nguyen, M. H., Roach, P. D. & Stathopoulos, C. E. (2013). Effect of gac aril microwave processing conditions on oil extraction efficiency, and β-carotene and lycopene contents. *J of Food Engineering,* 117, 486–491. http://dx.doi.org/10.1016/j.jfoodeng.2012.10.021

Nantarat, N., Mueller, M., Lin, W. C., Lue, S. C., Viernstein, H., Chansakaow, S., Sirithunyalug, J. & Leelapornpisid, P. (2020). Sesaminol diglucoside isolated from black sesame seed cake and its antioxidant, anti-collagenase and anti-hyaluronidase activities. *Food Biosci,* 36, 100628. https://doi.org/10.1016/j.fbio.2020.100628

Rangkadilok, N., Pholphana, N., Mahidol, C., Wongyai, W., Saengsooksree, K., Nookabkaew, S. & Satayavivad, J. (2010). Variation of sesamin, sesamolin and tocopherols in sesame (sesamum indicum L.) seeds and oil products in Thailand. *Food Chem.,* 122, 724–730. https://doi.org/10.1016/j.foodchem.2010.03.044

Sankar, D., Rao, R. M., Sambandam, G. & Pugalendi, K. V. (2006). Effect of sesame oil on diuretics or β-blockers in the modulation of blood pressure, anthropometry, lipid profile, and redox status. *Yale J Biol Med,* 79(1), 19–26. PMID: 17876372; PMCID: PMC1942178.

Thanonkaew, A., Wongyai, S., McClements, D. J. & Decker, E. A. (2012). Effect of stabilization of rice bran by domestic heating on mechanical extraction yield, quality, and antioxidant properties of cold-pressed rice bran oil (oryza saltiva L.). *LWT – Food Science and Technology,* 48, 231–236. https://doi.org/10.1016/j.lwt.2012.03.018

Uquiche, E., Jerez, M. & Ortiz, J. (2008). Effect of pretreatment with microwaves on mechanical extraction yield and quality of vegetable oil from Chilean hazelnuts (gevuina avellana mol). *Innovative Food Science and Emerging Technologies,* 9, 495–500. https://doi.org/10.1016/j.ifset.2008.05.004

Wroniak, M., Rekas, A., Siger, A. & Janowicz, M. (2016). Microwave pretreatment effects on the changes in seeds microstructure, chemical composition and oxidative stability of rapeseed oil. *LWT – Food Science and Technology,* 68, 634–641. http://dx.doi.org/10.1016/j.lwt.2016.01.013

Younces, O. S., Sorour, M. A. & Mohamed, E. N. (2016). Effect of microwave on drying of parsley plant. *Middle East J. Appl. Sci*., 06(04), 1100-1109. www.curresweb.com/mejas/mejas/2016/1100-1109.pdf

NUEJ
Naresuan University
Engineering Journal

Analysis of Factors Affecting Springback Angle in Bending of ASTM A-210 Gr. A1 Seamless Carbon Steel Tube

Somchai Kongnoo[1,2]*, Kawin Sonthipermpoon[1] and Somlak Wannarumon Kielarova[1]

[1]Department of Industrial Engineering, Faculty of Engineering, Naresuan University, Phitsanulok, Thailand
[2]Department of Mold & Die Technology, Phitsanulok Technical College, Institute of Vocational Education Northern Region 3, Phitsanulok, Thailand

* Corresponding author e-mail: somchaiko63@nu.ac.th

(Received: 5 October 2022, Revised: 19 January 2023, Accepted: 25 January 2023)

Abstract

Rotary Draw Bending (RDB) is a common process in the tube bending industry but the problem of springback often occurs. When the clamp die part is released after the bending process, the bent tube will spring back as a result of the material deforming. Several studies have attempted to determine the factors of springback but there is no convincing empirical evidence to establish a relationship between the input and output factors of the tube bending process variables in springback problem. In this research, the factors affecting the springback angle by the Taguchi method in bending seamless tubes ASTM A-210 Gr. A1, outside diameter 44.45 mm, were established. The Taguchi method is used for medium carbon seamless tubes for steam boilers. The four factors that were considered included wall thickness, bending radius, dwell time and bending angle. The results showed that all factors have a significant influence on the springback angle in the tube bending process, and each factor affects the springback angle differently. The factors that affect the springback angle the most are Bending Radius with an impact of 43.01%, Bending Angle 25.16%, Wall Thickness 16.05%, and Dwell Time 15.78%. As well, the time-dependent springback principle has a significant effect on the springback response in tube bending.

Keywords: Springback Optimization, CNC Tube Bending, Taguchi Method, ASTM A-210 Gr. A1, Seamless Steel Tube

1. INTRODUCTION

NC Mandrel-Less Rotary Draw Bending (RDB) is the most commonly used metal tube bending machine today. When the clamping parts in the RDB are removed, the shape of the tube will be restored and springback inevitably occurs. The actual geometry of the tube bending will deviate from the design requirements. This directly affects the forming accuracy and the quality of the metal tube. Therefore, accurate springback prediction is the key to springback compensation and control. Springback factor analysis, mechanism and law of springback and predicting springback have been extensively researched (Zhou et al., 2021). The process involves factor inputs and the responses between these inputs are complex. However, there has been no convincing empirical proof for establishing the relationship between the input and output factor variables in the tube bending process relevant to springback (Podder et al., 2020).

Several studies have investigated springback from bending tubes. Mentella et al. (2008) developed a new method for a feasibility study and the determination of the loading curves in the RDB process by controlling some of the main tooling parts, namely boosters and pressure dies. The main factors that were considered were thickness, outer diameter, bending radius and bending angle. Jiang et al. (2010) studied the coupling effects on the springback angle of the material properties and the bending angle during numerically controlled bending of a titanium alloy tube TA18. Yang et al. (2010) studied the role of friction in the bending behaviors of thin-walled tube in RDB with a small bending radius. Ho-Seung Jeong et al. (2012) conducted a predictive study of the springback angle during the bending process of Inconel 625. By applying Elastic Theory to predict the bending moment and springback of the tube, Mei Zhan et al. (2016) created an analytical model for tube bending springback that considered different parameter variations of titanium alloy tubes. Borchmann et al. (2020) studied the influence of the stiffness of the machine axes on the formation of wrinkles during RDB by finite element method (FEM) simulations that considered the stiffness of each machine axis. Huifang Zhou et al. (2021) studied springback angle prediction of circular metal tube considering the interference of cross-sectional distortion in mandrel-less rotary draw bending by distinguishing the variables affecting springback.

2. PROBLEM DESCRIPTION

Several studies have attempted to study the factors that influence the occurrence of springback and the input variables influencing springback are still important for future research. One factor related to springback is the time dependence which has been the subject of various studies. Daxin and Liu (2010) studied springback and time-dependent springback of 1Cr18Ni9Ti stainless steel tubes under bending. Jun Ma et al. (2020) studied the influence of natural deterioration Pre/Post-Aging of springback in bending Al-Mg-Si alloy tubes using the time-dependent principle to study the springback angle. However, these studies relied on the time condition before and after forming only but did not consider the time factor during the manufacturing process as shown in Figure 1. This alloy can improve its mechanical properties when it is heat treated and in the aging process.

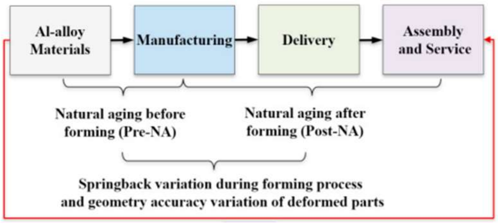

Figure 1 The influence of natural deterioration Pre/Post-Aging of springback. (Ma et al., 2020)

The time-dependent springback phenomenon has been experimentally observed in aluminium (Wang et al., 2004), stainless steel tubing (Daxin and Yafei Liu., 2010), high-strength steel (Lim et al., 2012), pure titanium sheets (Hama. et al., 2017), and Al-alloy (Ma et al., 2020). The mechanisms underlying the time-dependent springback are stress relaxation and creep behavior driven by the residual stress in the deformed materials (Ma et al., 2020).

The objective of the current study was therefore to fill the research gaps remaining from previous tube bending springback studies by studying other important factors, including the time-dependent factor, in the manufacturing process and the use carbon steel material. The predictions relevant to seamless steel tube bending for steam boiler applications are included in this comprehensive study.

3. EXPERIMENTAL DESIGN

In this study, metal tube bending experiments were conducted with the design of the experiments following the Taguchi method. The various factors affecting the springback angle were identified.

Table 1 Chemical composition and mechanical properties of ASTM A-210 Gr. A1

<table>
<tr><th colspan="6">Chemical Composition</th></tr>
<tr><td>C</td><td>Mn</td><td>P</td><td colspan="2">S</td><td>Si</td></tr>
<tr><td>0.27%</td><td>0.93%</td><td>0.035%</td><td colspan="2">0.035%</td><td>0.10%</td></tr>
<tr><th colspan="6">Mechanical Properties</th></tr>
<tr><td colspan="2">Tensile Strength</td><td colspan="2">Yield Strength</td><td colspan="2">Hardness</td></tr>
<tr><td colspan="2">415 MPa</td><td colspan="2">255 MPa</td><td colspan="2">79 HRB</td></tr>
</table>

3.1 Overview of the experimental method

The experimental equipment and tools included the Herber 76 CNC TB Bending Machine without the use of a mandrel is illustrated in Figure 2. This was necessary given the outer diameter-to-thickness ratio in the range of 7-10 mm (OD/t≤20) (Ma et al., 2020). The material used was medium carbon seamless steel tube ASTM A-210 Gr. A1. OD = 44.45 mm medium carbon steel tube. The chemical composition and mechanical properties of these materials are shown in Table 1.

3.2 Design of experiment

Experimental design and analysis by the popular Taguchi Method. The method that was adopted in the current research followed an orthogonal array type L27 (3^4), 27 bending operations were included in the process. The input factors were wall thickness, bending radial, dwell time and bending angle. The response factor was the springback angle. The level of these factors uses 3 level in the tube bending process is illustrated in Table 2.

Table 2 Description of the influence factors.

Input Factors	Level		
	Low	Medium	High
[A] Wall thickness (mm)	4.57	5.59	6.10
[B] Bending radius (mm)	76.2	114.3	152.4
[C] Dwell time (s)	0	3	6
[D] Bending angle	60°	90°	120°

In the calculation of the signal-to-noise ratio for the springback angle, where the springback angle is small, the impact of the input factors is small. Therefore, in this case, smaller is better, and the calculation is as follows:

$$S/N_s = -10\log\left\{\frac{\sum y_i^2}{n}\right\} \tag{1}$$

where S/N_s is the signal-to-noise ratio characteristic value where smaller is better, y_i is the sum of observations at level i, and n is the number of observations.

Figure 2 Herber 76 CNC TB Bending Machine.

3.3 Measurements Method

The springback angle of metal tube workpieces were checked with a Mitutoyo CMM model Beyond Apex 707. The angle Δθ is calculated as follows (Ma et al., 2020).

$$\Delta\theta = \theta_b - \theta_a \tag{2}$$

where $\Delta\theta$ is the springback angle, θ_b is the targeted bending angle and θ_a is the actual angle.

4. RESULTS AND DISCUSSION

The Taguchi method was followed in the design of these experiments.

4.1 Results of the Taguchi experiment L27 (3^4)

The results of the experiments on the orthogonal array L27 (3^4), performed according to the experimental plan, are shown in Tables 3 and 4. The springback angle $\Delta\theta$ was calculated using Equation (2) and the Signal-to-Noise Ratios in the case of Small-the-Better is shown in Table 3 and the average S/N Ratio of the level of the various factors affecting the springback angle are shown in Table 4.

Table 3 The average S/N Ratio of springback angle factor

Level	Input Factors			
	A	B	C	D
1	-18.01	-18.46	-17.28	-17.09
2	-17.39	-17.54	-17.63	-18.06
3	-17.40	-16.80	-17.89	-17.66
Delta	0.62	1.66	0.61	0.97
Percent	16.05	43.01	15.78	25.16
Rank	3	1	4	2

Table 4 The L27 test matrix and measured springback angles

Bending	Input Factors				Responds factor	
	A	B	C	D	$\Delta\theta$ (degree)	$\Delta\theta$ (Signal-to-Noise Ratios)
1	4.57	76.2	0	60	7.93	-17.99
2	4.57	76.2	0	60	8.02	-18.08
3	4.57	76.2	0	60	7.97	-18.03
4	4.57	114.3	3	90	8.27	-18.35
5	4.57	114.3	3	90	8.39	-18.48
6	4.57	114.3	3	90	8.41	-18.50
7	4.57	152.4	6	120	7.58	-17.59
8	4.57	152.4	6	120	7.45	-17.44
9	4.57	152.4	6	120	7.61	-17.63
10	5.59	76.2	3	120	8.19	-18.27
11	5.59	76.2	3	120	8.33	-18.41
12	5.59	76.2	3	120	8.26	-18.34
13	5.59	114.3	6	60	7.15	-17.09
14	5.59	114.3	6	60	7.19	-17.13
15	5.59	114.3	6	60	7.16	-17.10
16	5.59	152.4	0	90	6.85	-16.71
17	5.59	152.4	0	90	6.91	-16.79
18	5.59	152.4	0	90	6.82	-16.68
19	6.10	76.2	6	90	8.92	-19.01
20	6.10	76.2	6	90	8.87	-18.96
21	6.10	76.2	6	90	8.95	-19.04
22	6.10	114.3	0	120	7.14	-17.07
23	6.10	114.3	0	120	7.08	-17.00
24	6.10	114.3	0	120	7.21	-17.16
25	6.10	152.4	3	60	6.49	-16.24
26	6.10	152.4	3	60	6.39	-16.11
27	6.10	152.4	3	60	6.31	-16.00

Considering the average S/N Ratio of the level and various factors affecting the springback angle, as shown in Table 3, it can be concluded that the bending radial factor (B) affects the springback angle the most. This factor had an impact as high as 43.01%. The bending angle (D) contributed 25.16% to the springback angle, the tube wall thickness (A) 16.05% and the least impact factor was dwell time (C) at 15.78%. Also, it was noticed that the tube wall thickness factor and the stopping time factor were similar percentages with only a 0.27% difference.

Figure 3 shows the residual plots for the springback angle that were examined and were found to be normally distributed with a linear distribution plot and a normal histogram. It can also be concluded that the fitted values are normally distributed. When verifying the independence of the data it was found that the distribution of fitted values has an independent distribution pattern. The pattern cannot be predicted with certainty which shows that the error values are independent of each other.

The mean value of the main effects plot for S/N ratios shown in Figure 4, showed that the lowest tube wall thickness factor was 4.57 mm., the mean of S/N ratios was -18.01, but when the tube wall thickness was increased to 5.59 mm, the mean of S/N ratios was -

17.39, where the original value was +0.62, and the springback angle increased. The minimum bending radius factor was 76.2 mm, and the mean of S/N ratios was -18.46. When the bending radius was increased to 114.3 mm, the mean of S/N ratios was -17.54, an increase of +0.92, and when the bending radius was increased to 152.4 mm, the mean of S/N ratios was -16.80, a further increase from the lowest factor of +1.66. Also, when the lowest Dwell time factor was 0 seconds, the mean of S/N ratios was -17.28 and when the dwell time was increased to 3 seconds, the mean of S/N ratios was -17.63, a decrease of -0.35. Increasing the dwell time to 6 sec, the mean of S/N ratios was -17.89, down from the lowest factor of -0.61.

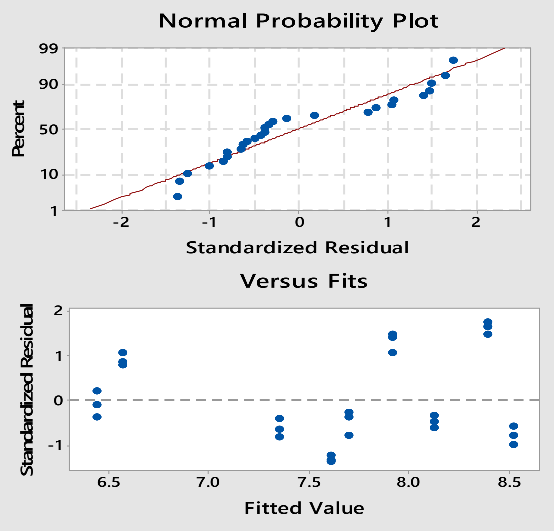

Figure 3 Residual plots for the springback angle.

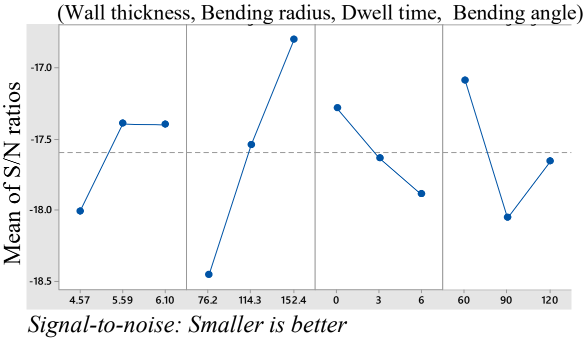

Figure 4 Mean of main effects plot for S/N ratios

Considering the fourth factor, the minimum bending angle factor of 60 degrees had a mean of the S/N ratios of -17.09. When the bending angle was increased to 90 degrees, the mean of the S/N ratios was -18.06, a decrease of -0.97. Then, when the bending angle was increased to 120 degrees, the mean of S/N ratios was -17.66, down from the minimum factor of -0.57.

The results of the analysis of each factor affecting the springback angle to the lowest value at $A_1B_1C_3D_2$ are tube wall thickness factor at 4.57 mm, bending radius factor at 76.2 mm, stopping time factor at 6 sec and bending angle factor degree at 90 degrees.

Table 5 ANOVA of the springback angle

Source	df	SSA	MSA	F-Value	P-Value
A	1	1.2630	1.2630	9.91	0.005
B	1	9.4323	9.4323	74.02	0.000
C	1	1.3613	1.3613	10.68	0.004
D	1	0.9988	0.9988	7.84	0.010
Error	22	2.8034	0.1274		
Total	26	15.8587			

S = 0.356966, R-sq. = 82.32%, R-sq. (adj) = 79.11%

The analysis of variance (ANOVA) in Table 5, at the significance level of 0.05, showed that the main factors were tube wall thickness, bending radius, dwell time and bending angle, at $p < 0.05$. It was shown that these four main factors significantly influenced the springback angle in the tube bending process. In addition, the reliability of the data is $R^2 = 82.32\%$, R^2 (adj) = 79.11%, so $R^2 > 80\%$. Therefore, the values obtained are reliable. for use in further research. The regression equation can be created as follows:

$$y_{\Delta\theta} = 10.657 - 0.34x_1 - 0.019x_2 + 0.0917x_3 + 0.00785x_4 \qquad (3)$$

where yΔθ is the response of the springback angle, x_1 is the tube wall thickness, x_2 is the bending radius, x_3 is the dwell time, x_4 is the bending angle.

4.2 Discussion

1. Experimental design and analysis by Taguchi Method is a popular method, and can determine the relationship of variables influencing the springback angle of ASTM A-210 Seamless Cold Drawn Medium-Carbon Steel Tubes Grade ASTM A-210. Gr. A1. If used in mass production, factory plant, production engineering or other engineering processes, the Taguchi Method will increase the efficiency of the work.
2. The main effect of all 4 factors, namely Wall Thickness, Bending Radius, Dwell Time, and Bending Angle, influence the value of the springback angle in significant tube bending process at 0.05. These findings will be useful in future research of factors such as the stress on the material, tube diameter, material type, and bending speed.
3. The factors that affect the springback angle the most are Bending Radius with an impact of 43.01%, Bending Angle impact 25.16%, Wall Thickness 16.05%, and Dwell Time 15.78%. It was also observed that the tube Wall Thickness factor and the Dwell Time factor were similar percentages, with only a 0.27% difference. If other factors are studied, as discussed in Item 1, the relationship between each factor may have different significance.
4. For the influence of the low effect of springback factor level when considering all 4 main factors, it can

be concluded that the wall thickness of the tube must be low. The bending radius must be low. Dwell time takes a lot of time. and the bending angle must be high.

5. Time-dependent in addition to considering before and after the manufacturing process, when considering in the manufacturing process, especially the forming process, for example, controlling the time during the material forming process can also help with the springback angle. In the future, if the time-dependent factors are further studied, all three processes of pre-forming, forming and post-forming should be included in the study. The details of the behavior of the material can then be more validly obtained.

5. CONCLUSION

In this research, the factors affecting the springback angle by the Taguchi method in bending seamless tubes ASTM A-210 Gr. A1, outside diameter 44.45 mm, were established. The experimental equipment and tools included the Herber 76 CNC TB Bending Machine without the use of a mandrel. This was necessary given the outer diameter-to-thickness ratio in the range of 7-10 mm (OD/t≤20). The Taguchi method is used for medium carbon seamless tubes for steam boilers. The four factors that were considered included wall thickness, bending radius, dwell time, and bending angle. The results showed that all factors have a significant influence on the springback angle in the tube bending process, and each factor affects the springback angle differently. The factors that affect the springback angle the most are Bending Radius with an impact of 43.01%, Bending Angle impact of 25.16%, Wall Thickness 16.05%, and Dwell Time 15.78% percent. As well, the time-dependent springback principle proved to exert a significant effect on the springback response in tube bending.

The results of this research can be used for further, such as springback angle prediction from regression equations to compare with other methods such as machine learning, another input factor affecting the springback angle value, another response factor related to tube bending such as ovality, has deserve further study.

6. ACKNOWLEDGEMENT

The authors gratefully acknowledge contributions from Mr. Charan Khamngoen, Assistant Governor of Electricity Generating 2, Mr. Boonthawee Khamkruang Ms. Jenjira Nanthaphong, Mr. Somnuk Wongkhot and Mr. Thanakorn Thechnan Technician Department and related parties under the Electricity Generating Authority of Thailand (EGAT). Mae Moh Power Plant, Lampang Province, who assisted in collecting this research data.

Thanks to the Faculty of Engineering at Naresuan University. They gave scholarships to support the study of graduate students (Ph.D.) to the researcher and author, Mr. Somchai Kongnoo. Finally, thanks to Mr. Roy I. Morien of the Naresuan University Graduate School for his editing of the grammar, syntax and general English expression in this document.

7. REFERENCES

Borchmann, L., Heftrich, C., & Engel, B. (2020). Influence of the stiffness of machine axes on the formation of wrinkles during rotary draw bending. Sn Applied Sciences, 2(10). https://doi:10.1007/s42452-020-03419-1

Daxin, E., & Liu, Y. (2010). Springback and time-dependent springback of 1Cr18Ni9Ti stainless steel tubes under bending. Materials & Design, 31(3), 1256-1261. https://doi.org/10.1016/j.matdes.2009.09.026

Hama, T., Sakai, T., Fujisaki, Y., Fujimoto, H., & Takuda, H. (2017). Time-dependent springback of a commercially pure titanium sheet. Procedia Engineering, 207, 263-268. https://doi.org/10.1016/j.proeng.2017.10.772

Jeong, H. S., Ha, M. Y., & Cho, J. R. (2012). Theoretical and FE Analysis for Inconel 625 Fine Tube Bending to Predict Springback. International Journal of Precision Engineering and Manufacturing 13(12), 2143-2148. https://doi:10.1007/s12541-012-0284-z

Jiang, Z. Q., Yang, H., Zhan, M., Yue, Y. B., Liu, J., Xu, X. D., & Li, G. J. (2010). Establishment of a 3D FE model for the bending of a titanium alloy tube. International Journal of Mechanical Sciences, 52(9), 1115-1124. https://doi:10.1016/j.ijmecsci.2009.09.029

Lim, H., Lee, M. G., Sung, J. H., Kim, J. H., & Wagoner, R. H. (2012). Time-dependent springback of advanced high strength steels. International Journal of Plasticity, 29, 42-59. https://doi.org/10.1016/j.ijplas.2011.07.008

Ma, J., Ha, T., Blindheim, J., Welo, T., Ringen, G., & Li, H. (2020). Exploring the Influence of Pre/Post-Aging on Springback in Al-Mg-Si Alloy Tube Bending. Procedia Manufacturing, 47, 774-780. https://doi.org/10.1016/j.promfg.2020.04.239

Mentella, A., Strano, M., & Gemignani, R. (2008). A new method for feasibility study and determination of the loading curves in the rotary draw bending process. International Journal of Material Forming, 1, 165-168. https://doi:10.1007/s12289-008-0017-0

Podder, B., Banerjee, P., Kumar, K. R., & Hui, N. B. (2020). Forward and reverse modelling of flow forming of solution annealed H30 aluminum tubes. Neural Computing and Applications, 32(7), 2081-2093.
https://doi:10.1007/s00521-018-3749-x

Wang, J. F., Wagoner, R. H., Carden, W. D., Matlock, D. K., & Barlat, F. (2004). Creep and anelasticity in the springback of aluminum. International Journal of Plasticity, 20(12), 2209-2232.
https://doi.org/10.1016/j.ijplas.2004.05.008

Yang, H., Li, H., & Zhan, M. (2010). Friction role in bending behaviors of thin-walled tube in rotary-draw-bending under small bending radii. Journal of Materials Processing Technology, 210(15), 2273-2284.
https://doi:10.1016/j.jmatprotec.2010.08.021

Zhan, M., Wang, Y., Yang, H., & Long, H. (2016). An analytic model for tube bending springback considering different parameter variations of Ti-alloy tubes. Journal of Materials Processing Technology, 236, 123-137.
https://doi:10.1016/j.jmatprotec.2016.05.008

Zhou, H. F., Zhang, S. Y., Qiu, L. M., & Wang, Z. L. (2021). Springback angle prediction of circular metal tube considering the interference of cross-sectional distortion in mandrel-less rotary draw bending. Science Progress, 104(1), 30.
https://doi:10.1177/0036850420984303

8. BIOGRAPHIES

Somchai Kongnoo, he received the B.I.Ed. Industrial Engineering from Pathumwan Institute of Technology in 2003, M.Eng. Management Engineering from Naresuan University in 2013. The present studying a Ph.D. in Management Engineering at Naresuan University, Thailand. From 2000 to 2011, he was a Design Engineer in Pichit Industrial Works Co., Ltd., present is Schunk Carbon Technology Co., Ltd. (Schunk Group). The company is an industry about manufacturing automobile parts produce. Responsibilities about mechanical machine design, tooling design, CAD/CAM/CNC and manufacturing process. The last position is Engineering Design Manager. Since 2011, he has been a teacher at Department of Mold & Die Technology, Phitsanulok Technical College, Institute of Vocational Education: Northern Region 3, Phitsanulok.

Kawin Sonthipermpoon, he received B.S.degree in Physics from Srinakarinwirot Phisanulok campus, Thailand in 1985 and M.Eng. degree in Electrical Engineering from King Mongkut's Institute of Technology Ladkrabang (KMITL), D.Eng. in Manufacturing Systems Engineering from Asian Institute of Technology (AIT), Thailand and received the Alexander von Humboldt Foundation scholarship to do Post-doctoral research in the Aerodynamic impeller design for Aero-Engines at the Institute of Turbomachinery, Hannover University, Germany. From 2005 - onwards, Associate Professor, Naresuan University, continue duties: Research in the field of Computational Fluid Dynamics (CFDs), Renewable energy such as Dish-Stirling Energy Systems. CNC machining application and CAD/CAM/CAE design, Enterprise Resource Planning (ERP), Information Technology as well as Robotics application and Smart Manufacturing Systems Engineering.

Somlak Wannarumon Kielarova, she received B.Eng. Industrial Engineering from Chiang Mai University, M.Eng. in Manufacturing Systems Engineering and D.Eng. Design and Manufacturing Engineering from Asian Institute of Technology (AIT). After, he received a scholarship to do post-doctoral research in the field of Jewelry Engineering at the Institute of Politechico di Torino, Italy. Began working as a lecturer under the Department of Industrial Engineering. Faculty of Engineering Naresuan University since 1997 with research results in Development of Generative Design, Product Design, Parametric Design and Artificial Intelligence for Product Design.

NUEJ
Naresuan University
Engineering Journal

Suitable Voltage Determination of Ohmic Heating Process for Household Pork Steak Preparation Machine

Siwakon Sriruwat [1], Orose Rugchati [2] and Sarawut Wattanawongpitak [1,*]

[1] Department of Electrical and Computer Engineering, Faculty of Engineering, Naresuan University, Phitsanulok, Thailand
[2] Department of Argo-Industry, Faculty of Agriculture Natural Resources and Environment, Naresuan University, Phitsanulok, Thailand

* Corresponding author e-mail: sarawutw@nu.ac.th

(Received: 13 September 2022, Revised: 12 January 2023, Accepted: 8 February 2023)

Abstract

This paper presents the procedure to determine the suitable applied voltage in the ohmic heating process for pork steak preparation combined with conventional grilling. The electrical, physical, and chemical properties parameters that are investigated. During the ohmic heating process, not only the temperature rises and duration time for each cooking level examined, but also the ampacity required of the equipment in the process is considered. In the experiment, meat samples with cross-section areas: 4 × 2, 4 × 3, and 4 × 4 inch^2 with a thickness of 0.5 inches were tested by an alternating current (AC) voltage source: 20, 25, and 30 V at a frequency of 50 Hz within 300 seconds. The criteria for selecting the suitable voltage were the rate of temperature rise of the meat sample must increase linearly for all 3 sizes of meat before the pre-boiling temperature, the maximum load current did not exceed the copper wire ampacity, and the duration time used between each adjacent stage of meat cooking was chosen to be longer. From the experiment results, the appropriate voltage for the steak cooker's default setting was 20 V for the following reasons: 1) The rates of temperature increase were linearly proportional for all 3 sizes of meat samples as well-done or internal meat temperature reached 71 ^{o}C and within 300 seconds. 2) The maximum load current of the applied voltages at AC 20 V was the lowest current (7.43 A). 3) The duration time used between each adjacent stage of meat cooking of AC 20 V was the longest time compared to others. Thus, the steak's cooking level can be easily managed. After the ohmic heating process, the steaks' physicochemical properties (pH, moisture, drip loss, cooking loss, water holding capacity (WHC), shear force, and color) were evaluated. The steaks did not approach the dangerous toxicity level, and the cooking time was nearly half that of conventional grilling.

Keywords: Alternating Current (AC), Suitable Voltage, Ohmic Heating, Steak Preparation Machine, Physicochemical Properties, Cooking level, Cooking time

1. INTRODUCTION

At present, ohmic heating is widely used in food processing and quality improvement. Preheating, cooking, pasteurization, and sterilization are all examples of these processes (Yildiz-Turp et al., 2013). Compared to other heating systems, ohmic heating allows for a quick temperature rise while saving energy. Ohmic heating is a process that results from the dissipation of heat caused by the passage of electric current through the food's resistance. To achieve a rapid temperature increase, the ohmic heating methods must account for the kind of food with low electrical resistance (Richa et al., 2017).

Generally, the ohmic heating is employed in muscle food to increase meat quality, accelerate the cooking process, and extend shelf life. However, due to the heterogeneous structure of the meat and the varying electrical conductivity of each piece of meat, a wholesale cut of meat was inappropriate for ohmic heating on an industrial scale. Consequently, the heat generated in each component differs (Shirsat et al., 2004). Nevertheless, in steak production, meat samples were categorized based on type, size, and shape. Therefore, the electrical conductivity of meat should be homogenous. The quantity of electrical current that flows through food is determined by the electrical resistance of the whole piece of meat. The electrical resistance varies with meat size, shape, and overall electrical conductivity. The electrical conductivity in meat consists of (1) muscle and the structure of the junction between connective tissues and muscle stripes, (2) Fat content retards temperature rises and results in unequal heat distribution between fat and muscle tissues (Shirsat et al., 2004a; Mahapatra et al., 2007; Damez and Clerjon, 2013), and (3) Moisture content and the concentrations of other intrinsic chemicals like salt and acid have a role in ohmic heating. The amount of salt or acid acts as a catalyst for ionization, with additional ions greatly increasing the electrical conductivity of the meat (Chen et al., 2022). When acid or salt are introduced, the rate of temperature change is increased (Marcotte and Trigui, 2000). Additionally, the inner water content influences the overall electrical conductivity by approximately 70%. As the temperature of the meat increases, the electrical conductivity of the meat also trends to increase (Shirsat et al., 2004).

Following the ohmic heating process in meat, softness, color, and toxicity are important factors to consider. The softness of the food can be measured by shear force or juiciness measurements. Zell et al. (2010) found that in the case of ohmic heating by applying a voltage to a high temperature for a short time (HTST), it will be very tough and less juicy than in the case of a low temperature that takes a long time (LTLT). But it was also found (Jung et al., 2022) that LTLT was softer than conventional heating methods because of large cooking losses. Bozkurt and Icier (2010) found that the fat content of the meat did not affect the color values. Nonetheless, ohmic heating provides brighter colors and a more homogeneous appearance of the color than conventional heating, which provides a stepped appearance of the color depending on the amount of heat radiated. The last part deals with food toxicity, which is induced by corrosion from metal to food contaminants, with the amount of corrosion varying depending on the type of metal utilized. Platinum, titanium, or food-grade metal coatings are recommended (Jun et al., 2007; Wang and Farid, 2015).

Generally, the electrical power sources in the ohmic heating process consist of alternating current (AC) and direct current (DC) sources. For both electrical power sources, the increase in temperature followed the same trend. In the case of DC ohmic heating, an oxidation reaction occurred in the anode electrode region. Consequently, the anode side of the meat has a higher internal temperature than the other side. In addition, residual metal and gel formation occurred at both electrodes during the DC ohmic heating process (Sriruwat et al., 2019). Therefore, AC ohmic heating is a better choice than DC ohmic heating. Sriruwat et al. (2020) studied the relationship between the input voltage and heat generated in pork meat by an AC ohmic heating process at voltage levels of 20, 25, and 30 V; cross-section areas of 4×2, 4×3, and 4×4 inch^2 with 0.5 inch thickness. The result shows that the rate of temperature change was linear within 3 minutes, but the temperature could not be increased to 71 ºC (well-done) except at 30 V (4×2 inch^2) before becoming a quadratic curve.

Based on the aforementioned above, AC ohmic heating with a voltage between 20 and 30 V can be used to enhance the internal temperature of a steak in less time and that was softer meat than conventional grilling. To maintain a linear rate of temperature rise while controlling the input voltage in order to cook all sizes of meat to a well-done. The leanest meat, the simplest control, the duration time, and the electrical effect must be considered.

Therefore, this paper aims to investigate the suitable voltage for the ohmic heating process determined by the temperature rise, the duration time between each adjacent stage of meat cooking, and the maximum current. The pork samples have a cross-section area of 4×2, 4×3, and 4×4 inch^2 with 0.5 inch thickness. The applied AC voltage level is 20, 25, and 30 V at a frequency of 50 Hz within 300 seconds. Furthermore, after the heating process, the experiments are shown their cooking time and quality of ohmic heating including pH, moisture content, drip loss, cooking loss, water holding capacity (WHC), shear force, and color.

2. THE EFFECT OF PHYSICAL AND ELECTRICAL FACTORS IN TEMPERATURE RISE

The increase in temperature during the ohmic heating process is generated by the input of electrical energy (W_e) into the meat, which is transformed into heat energy (W_h) and heat loss to the surrounding (ε), as represented by Equation (1). In addition, the electrical power is proportional to the current passing through it and the overall electrical resistance of the meat. Therefore, as the voltage rises, the temperature rises as well, changing the structure of the meat and, as the muscle structure changes, altering the rate at which the temperature rises.

$$\begin{aligned} W_e &= W_h + \varepsilon \\ I^2Rt &= mC_p\Delta T + \varepsilon \end{aligned} \tag{1}$$

where W_e is electrical energy (J), W_h is thermal energy (J), I is electrical current (A), R is electrical resistance (Ω), t is the duration of time for the ohmic heating process (s), m is mass (kg), C_p is the specific heat capacity of a substance (J/kg^oC), and ε is heat energy loss (J).

The electrical resistance is proportional to the electrical conductivity, cross-sectional area, and distance through which the current passes, as represented by Equation (2).

$$R = \frac{1}{\sigma}\cdot\frac{l}{A} \tag{2}$$

where A is the cross-sectional area (m^2), l is the thickness (m), and σ is the electrical conductivity (S/m).

As the temperature of a protein increases, its structure changes, resulting in a change in its overall electrical conductivity. When the temperature rises, connective tissue and muscle fibers contract more, resulting in water loss. It has been found that the meat's water is extracted from the intercellular gaps of the muscle fibers, resulting in a rise in the meat's overall electrical conductivity (Cross H.R. et al. 1986). Furthermore, Equation 1 shows that the thermal energy is mass dependent. Therefore, the increase in weight due to water has a significant effect on the rate of temperature rise.

3. MATERIALS AND METHODS

3.1 AC ohmic heating system

Figure 1(a) shows an ohmic heating system that includes a variable transformer ranging from 0 to 230 V, an ohmic cell, and measurement equipment. The ohmic cell is composed of parallel pads made of stainless steel 316L with 4.50 × 4.50 inch^2 and a thickness of 0.04 inch that is enclosed in a plastic box 4.72 × 4.72 × 1.18 inch^3.

A digital multimeter, Fluke model: Fluke-115 was used to measure the voltage drop and current, and temperature using a digital clamp meter, HT model: HT9015 by placing K-type temperature probes at places T1 and T2, each measuring 0.5 inch from the edge of the meat, as seen in Figure 1 (b).

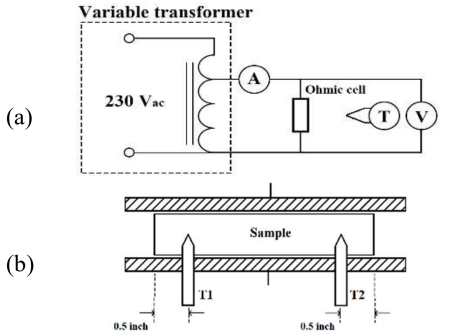

Figure 1 (a) AC ohmic heating system including variable transformer and (b) ohmic cell with temperature probe installed

3.2 Pork meat samples

Generally, the conductivity of pork meat after the slaughter at 90 minutes was in the range of 3.50 – 5.00 mS/cm, and at 24 hours after the slaughter, it was in the range of 5.00 – 8.00 mS/cm (Runowska et al., 2010). Pork meat typically contains 53% water, 26% protein, 21% fat, and less than 1% carbohydrates. where the sirloin portions are low fat (4%).

Pork meat (sirloin) from municipal slaughterhouses in Phitsanulok Province has been butchered within the last 24 hours. The muscle line was cut into a cross-section with 4 × 2, 4 × 3, and 4 × 4 inch^2, thickness 0.5 inch, and average weight (80, 115, and 150 g). The storage temperature was around 25 °C, with an initial pH of 5.5 to 5.7.

3.3 The experiment procedure

In order to find the suitable voltage, AC voltages of 20, 25, and 30 V were compared on all 3 sizes of meat within 300 seconds. The experiment was repeated 5 times and the mean was calculated. The electrical and temperature results were analyzed according to the following steps:

1. Collect the data and plot the rate of temperature change with respect to time, the maximum current used at each voltage level, and measure the duration time at the adjacent cooking level.
2. Analyze the temperature change of each voltage level by choosing the voltage level that maintains a linear rate of temperature rise, which provides the longest duration time and appropriate current for the design of the equipment in ohmic heating.

After obtaining the suitable voltage, an examination of ohmic heating with grilling was conducted utilizing the Association of Official Analytical Chemists (AOAC) method in order to evaluate various chemical and physical properties such as pH, moisture content, drip loss, cooking loss, WHC, shear force, and color. The AOAC is a widely recognized and respected source that provides reliable chemical and microbiological methods and consensus standards, which are adopted by various international organizations as harmonized reference methods. Subsequently, the data were analyzed utilizing the Statistical Package for the Social Science (SPSS), and mean values were compared utilizing Duncan's new multiple-range tests. Additionally, a comparison of the cooking times of ohmic heating with grilling to conventional grilling was conducted at five different cooking levels, while maintaining the same temperature, and residual metal was measured using an Atomic Absorption Spectrophotometer (Thai Industrial Standards Institute 1378-2559).

4. RESULTS

4.1 Procedure for determining the suitable voltage level

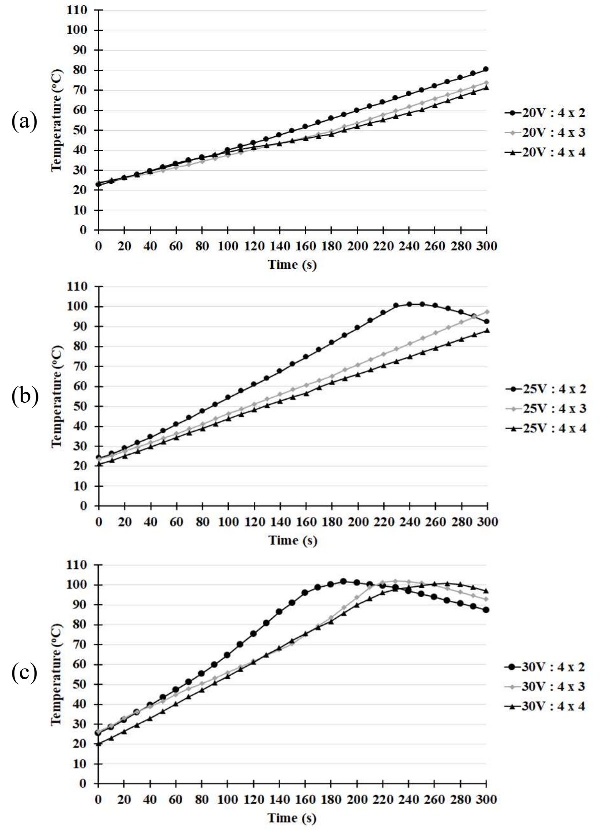

Figure 2 Relationship between temperature (°C) and time (s) of all meat sizes when applying (a) 20 V, (b) 25 V, and (c) 30 V

The relationship between temperature and time of all meat sizes during ohmic heating at different voltages was presented in Figure 2. The rate of temperature rise prior to 71 ºC was found to be constant at all voltages, except AC 30 V 4 × 2 inch^2 as shown in Figure 2(c). The increase in conductivity and the nonlinear rate of temperature rise during the pre-boiling period were caused by the impact of water leaking from the cell membrane due to the high voltage drop. As water began to evaporate, the electrical conductivity gradually decreased. After the temperature rises to 100 ºC, the temperature remained constant and gradually decreased.

Table 1 presents the rate of temperature rise and maximum operating current for consideration of the ohmic cooking time. At AC 20 V, the temperature rise rate was between 0.16 and 0.19 °C/s, and the maximum operating current was 7.43 A. This was lower than at AC 25 V and 30 V, where the temperature increase rate was between 0.22 and 0.34, and 0.34 and 0.45 °C/s, respectively, at maximum currents of 10.42 and 12.49 A.

In addition, the duration time between each adjacent stage of meat cooking was compared in Table 2. At AC 20 V, the cooking time was the longest of all voltage levels. Comparing each size of the meat, it was found that the largest size had the longest temperature rise time. This is because the specific heat capacity of water is greater than that of muscle (Muthukumarappan et al., 2019). The specific heat capacity is the amount of heat absorbed per unit mass of a material when its temperature increases by 1 K or 1 °C. Therefore, at the same voltage level, the overall specific heat capacity of large meat is higher than that of small meat. When the duration time between each adjacent stage of meat cooking was obtained from the fitting curve in the initial to well-done temperature.

The results of the experiment indicate that at AC 20 V, the temperature can be increased to 71 °C, a well-done state, providing a consistent temperature increase for all 3 sizes of meat. This voltage level also has the longest cooking time and the lowest maximum current. Therefore, we selected 20 V as the suitable voltage for the pork steak preparation machine. Figure 3 shows a comparison of cooking time between ohmic heating with grilling and conventional grilling, demonstrating that ohmic heating with grilling requires less time than conventional grilling. Additionally, the cooking time at the well-done was approximately half that of a conventional grilling.

4.2 Chemical, physical, and residual metal on the ohmic heating process in combination with grilling

Table 3 shows the chemical changes during ohmic heating combined with grilling. The pH of the meat tended to become slightly acidic after ohmic heating, which occurs as a result of the breakdown of muscle cells that releases intracellular fluid. In cases that involve a great deal of damage (well-done), the pH is significantly different from other cooking levels ($p<0.05$).

In addition, the cooking loss was low at the medium and medium well levels, since there was substantial water loss prior to heat storage. This resulted in a low residual water value in the meat for low-temperature storage. In terms of water holding capacity, the well-done level was found to be lower than the other levels, due to the large volume of water discharged at the start. Consequently, each value was substantially different from the others ($p<0.05$).

Table 4 shows the shear force and color values during cooking. The shear forces of the medium well and well-done meats were observed to be significantly low as pork meat becomes tender at a higher temperature. In terms of color values, rare meat was the brightest because the surface browns as the temperature rises, while medium rare and medium meat had the highest redness values among the different cooking levels. As a result, each value was substantially different from the others ($p<0.05$). L* represents lightness, a* represents relative to the green (-a*) – red (+a*) opponent colors, and b* represents relative to the blue (-b*) – yellow (+b*) opponent colors.

Table 5 shows the metal residues on pork steaks treated with ohmic heating and grilling. Manganese, chromium, and iron were analyzed using an Atomic Absorption Spectrophotometer (Thai Industrial Standards Institute 1378-2559). The findings indicate that permissible levels of heavy metals had no adverse effect on the health or appearance of the steak product.

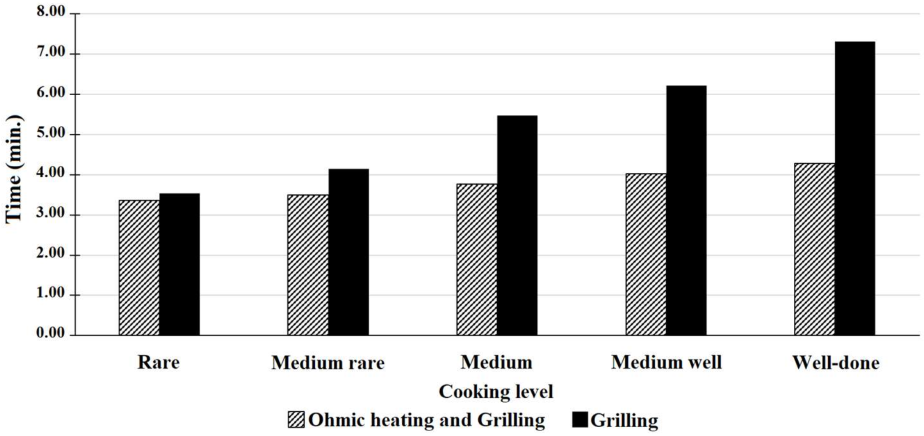

Figure 3 The relationship of cooking time (min) at different cooking levels of two heating processes.

Table 1 The rate of temperature rise and the maximum current during the ohmic heating process

Voltage level (V)	**dT/dt (°C/s)**			**I_{max}(A)**		
	(4 × 2)	(4 × 3)	(4 × 4)	(4 × 2)	(4 × 3)	(4 × 4)
20	0.19	0.17	0.16	6.96	7.43	7.24
25	0.34	0.25	0.22	9.53	10.40	10.42
30	0.45	0.35	0.34	10.47	10.49	12.49

Table 2 Duration time between each adjacent stage of meat cooking

Cooking level	**Temperature (°C)**	**Duration time between each adjacent stage of meat cooking (seconds)**								
		20V			**25V**			**30V**		
		(4 × 2)	(4 × 3)	(4 × 4)	(4 × 2)	(4 × 3)	(4 × 4)	(4 × 2)	(4 × 3)	(4 × 4)
R – MR	60-62	11	12	13	6	8	9	4	6	6
MR – M	62-65	16	18	19	9	12	14	7	9	9
M – MW	65-68	16	18	19	9	12	14	7	9	9
MW - WD	68-71	16	18	19	9	12	14	7	9	9

Note: R is rare, MR is medium rare, M is medium, MW is medium well and WD is well-done.

Table 3 Chemical properties of pork steaks treated with ohmic heating and grilling (initial pH 5.68, oil temperature 180 °C, furnace temperature 240 °C)

Cooking level	**pH** (after trial)	**Moisture content** (%)	**Drip loss** (%)	**Cooking loss** (%)	**WHC** (%)
Rare	5.99±0.06^{ab}	68.24±0.88	11.09±2.45^{a}	14.83±0.89^{a}	75.35±4.87^{a}
Medium rare	6.10±0.18^{a}	66.42±4.20	9.10±1.46^{a}	12.62±1.20^{b}	43.51±1.50^{b}
Medium	5.99±0.01^{ab}	67.03±0.42	7.90±0.34^{ab}	10.47±0.79^{c}	28.42±1.13^{d}
Medium well	5.93±0.06^{ab}	66.65±0.61	10.21±2.35^{a}	6.31±0.85^{d}	42.10±1.02^{b}
Well-done	5.87±0.05^{b}	68.06±1.34	5.27±0.96^{b}	4.90±0.97^{d}	34.89±0.20^{c}

Note: Vertically different characters showed a statistically significant difference at ($p< 0.05$)

Table 4 Physical properties of pork steaks treated with ohmic heating and grilling (initial pH 5.68, oil temperature 180 °C, furnace temperature 240 °C)

Cooking level	**Shear force** (kgF)	**Color value**		
		L*	**a***	**b***
Rare	7.32±0.39^{a}	68.85±0.55^{a}	7.26±0.31^{b}	21.52±2.00^{b}
Medium rare	7.68±0.63^{a}	61.54±0.36^{c}	8.36±0.33^{a}	23.23±1.69^{b}
Medium	4.97±0.70^{b}	59.60±0.25^{d}	8.60±0.16^{a}	25.96±0.83^{a}
Medium well	4.51±0.26^{b}	62.35±0.26^{b}	7.18±0.50^{b}	21.99±0.71^{b}
Well-done	4.38±0.31^{b}	62.76±0.13^{b}	6.30±0.26^{c}	26.63±0.44^{a}

Note: Vertically different characters showed a statistically significant difference at ($p< 0.05$).

Table 5 Metal residues on pork steaks treated with ohmic heating and grilling

Cooking level	**Residual metal type (ppm)**		
	Mn	**Cr**	**Fe**
Rare	0.06±0.08	0.03±0.05	0.07±0.00
Medium rare	0.00	0.07±0.02	0.08±0.06
Medium	0.11±0.03	0.04±0.02	0.13±0.01
Medium well	0.02±0.03	0.03±0.03	0.14±0.06
Well-done	0.10±0.08	0.06±0.04	0.24±0.10

5. CONCLUSION

This paper presents a procedure for selecting the suitable voltage of power supply in ohmic heating processes for household pork steak preparation machines at different cooking levels. This paper also considers the tenderness, color, and residual metal when used in the cooking process. Based on the proposed selection procedure in material and methods, it was determined that AC 20 V is the suitable voltage for a pork steak preparation machine, as the temperature can be raised to 71 ºC (well-done) for all 3 sizes of meat while maintaining a constant rate of temperature rise throughout 300 seconds. the maximum current did not exceed the copper wire ampacity, and the duration time between each stage of meat cooking was the longest. According to the chemical and physical experimental results, the shear forces of medium well and well-done meats were observed to be significantly low. In terms of color values, rare meat was the brightest color, while medium rare and medium meat had the highest redness values among the different cooking levels. The cooking time for well-done steak was half that of a conventional grill, and the amount of heavy metal contained in pork meat was within permissible limits and has no negative impact on the health or appearance of the steak product. In addition, the suitable voltage-selecting procedure of ohmic heating combined with grilling can be used in the design of electrical power supplies for other sizes and types of meat.

6. ACKNOWLEDGMENT

This study is funded by research funding from the Faculty of Engineering. We also appreciate the cooperation of the Department of Argo-Industry at Naresuan University's Faculty of Agriculture, Natural Resources, and Environment for this research.

7. REFERENCES

Bozkurt, H., and Icier, F. (2010). Ohmic cooking of ground beef: Effects on quality. *Journal of Food Engineering, 96(4),* 481–490.

Chen, Y., Llave, Y., Jiao, Y., Okazaki, E., Sakai, N., & Fukuoka, M. (2022). Ohmic tempering using a high frequency ohmic heating and model food of minced tuna based on Alaska pollock surimi – Evaluation of electrical conductivities. *Innovative Food Science & Emerging Technologies, 76,* Paper no.102940.

Cross, H. R., Durland, P. R., Seideman, S. C. (1986). Sensory qualities of meat. *In: Bechtel PJ, editor. Muscle as food. New York: Academic Press; 1986.* 297–320.

Damez, J. L., & Clerjon, S. (2013). Quantifying and predicting meat and meat products quality attributes using electromagnetic waves: an overview. *Meat Science, 95(4),* 879-896.

Jun, S., Sastry, S., & Samaranayake, C. P. (2007). Migration of electrode components during ohmic heating of foods in retort pouches. *Innovative Food Science and Emerging Technologies, 8(2),* 237–243.

Jung, A. H., Hwang, J. H., Jun, S., & Park, S. H. (2022). Application of ohmic cooking to produce a soy protein-based meat analogue. *LWT-Food Science and Technology, 160,* Paper no.113271.

Mahapatra, A. K., Jones, B. L., Nguyen, C. N., & Kannan, G. (2007). Experimental Determination of the Electrical Resistivity of Beef. *American Society of Agricultural and Biological Engineers Annual International Meeting,* Paper no. 076031.

Marcotte, M., & Trigui, M. (2000). Effect of Salt and Citric Acid on Electrical Conductivity and Ohmic Heating of Viscous Liquids. *Food Research and Development Centre Agriculture and Agri-Food,* Paper no. J2S 8E3.

Muthukumarappan, K., Marella, C., & Sunkesula, V. (2019). *Handbook of Farm, Dairy and Food Machinery Engineering (3rd ed.).* Academic Press. https://doi.org/10.1016/C2017-0-01578-1

Richa, R., Shahi, N. C., Singh, A., Lohani, U. C., More, P. K., Kumar, A., & Bhattacharya, T.K. (2017). Ohmic Heating Technology and Its Application in Meaty Food: A Review. *Advances in Research, 10(4),* Paper no. AIR.33799.

Runowska, G. C., Lyczynski, A., Pospiech, E., Podsiadla, M. K., Wojtczak, J., Rzosinska, E., Mikolajczak, B., Grzes, B., Iwabska, E., Krzecio, E., Sieczkowska, H., & Antosik, K. (2010). Electrical Conductivity as an Indicator of Pork Meat Quality. *Journal Central European Agriculture, 11(1),* 105-112.

Shirsat, N., Lyng, J. G., Brunton, N. P., & McKenna, B. (2004). Conductivities and Ohmic Heating of Meat Emulsion Batters. *Journal of Muscle Food, 15,* 121-137.

Shirsat, N., Lyng, J. G., Brunton, N. P., & McKenna, B. (2004). Ohmic processing: electrical conductivities of pork cuts. *Meat Science, 67,* 507–514.

Sriruwat, S., Rugchati, O., & Wattanawongpitak S. (2019). The Study of Temperature Variation within Porcine Meat Due to Low Voltage Direct Current under Ohmic Heating Process. *The Electrical Engineering Conference (EECON)*, *42(2)*, 553-556.

Sriruwat, S., Rugchati, O., & Wattanawongpitak S. (2020). Analysis of Temperature Variation within Porcine Meat Due to Alternating Current under Ohmic Heating Process. *The Electrical Engineering Conference (EECON)*, *43,* 615-618.

Wang, R., & Faris, M. M. (2015). Corrosion and health aspects in ohmic cooking of beef meat patties. *Journal of Food Engineering, 146,* 17-22.

Yildiz-Turp, G., Sengun, I. Y., Kendirci, P., & Icier, F. (2013). Effect of Ohmic Treatment on Quality Characteristic of Meat: A review. *Meat Science, 93,* 441-448.

Zell, M., Lyng, J. G., Cronin, D. A., & Morgan, D. J. (2010). Ohmic cooking of whole beef muscle Evaluation of the impact of a novel rapid ohmic cooking method on product quality. *Meat Science, 86,* 258–263.

NUEJ
Naresuan University
Engineering Journal

Assessment of Performance and Durability in Cement-Stabilized Quarry By-Product Soil as Road Pavement Bases

Nattanon Khumkud[1], Korakod Nusit[2*], Peerapong Jitsangiam[3], Polpreecha Chidburee[2], Susit Chaiprakaikeow[4],
Suriyavut Pra-ai[5] and Purichai Keawma[1]

[1] Department of Civil Engineering, Faculty of Engineering, Naresuan University, Phitsanulok, Thailand
[2] Center of Excellence on Energy Technology and Environment. Faculty of Engineering, Naresuan University, Phitsanulok, Thailand
[3] Department of Civil Engineering, Faculty of Engineering, Chiang Mai University, Chiang Mai, Thailand
[4] Department of Civil Engineering, Faculty of Engineering, Kasetsart University, Bangkok, Thailand
[5] RS2GH Research Unit, School of Engineering, University of Phayao, Phayao, Thailand

* Corresponding author e-mail: korakodn@nu.ac.th

(Received: 11 October 2022, Revised: 9 February 2023, Accepted: 14 February 2023)

Abstract

The knowledge of polymer-modified concrete has been well established and employed in real field applications for over a decade. On the other hand, research on polymer-stabilized soil is still limited. Therefore, this study aims to evaluate the performance and durability of polymer-stabilized soil for pavement applications. This study used the same polymer types for concrete modification as soil stabilizers. Two types of polymers used in this research are the Styrene Acrylic (SA) polymer and Styrene-Butadiene Rubber (SBR). The engineering performance, water absorption, and durability tests were conducted to characterize the polymer-stabilized soils. Preliminary results reveal that the strength and durability of polymer-stabilized quarry by-product soil can be improved by the proper dosage of polymers and cement. However, stabilized soil with the polymer alone cannot resist moisture damage at an early age; these are indicated by the dramatic drops in CBR values of the soaked specimens. Therefore, the stabilized soil requires little cement to gain its early strength. The test results indicate the possibility of employing polymer-stabilized cemented soil as road pavement materials. Besides the strength improvement by 21% to 29%, the polymer additives also enhanced the durability and reduced the water absorption rate of the cemented soil.

Keywords: Polymer-stabilized Pavement Materials, Quarry by-product, Durability, Water Absorption

1. INTRODUCTION

Stabilizing soil with chemical and mechanical additives is becoming more widely used for road pavement constructions. Among these methods, adding cement to enhance the performance of pavement materials seems to be the most common and simply used procedure. The strength and stiffness of pavement materials can be greatly improved by adding a small amount of Portland cement to the material mixtures. However, the cement-stabilized pavement materials are still susceptible to moisture damage (Erlingsson et al., 2017; Jitsangiam and Nikraz, 2012) and fatigue failure (Jitsangiam et al., 2016).

Currently, the pavement materials that successfully prevent damage from moisture ingress are unavailable (Jitsangiam and Nikraz, 2012). An innovative pavement material with water-resistant properties is required to protect the road structure from moisture damage. The water-resistant or 'hydrophobic' behaviors of geotechnical materials were discovered by Tillman et al. (1989). Polymer additives also increase the water repellent of treated soils (Raucah et al., 1993). Consequently, polymer additives are becoming more widely used for pavement material stabilization in recent years. The polymers are added to the soils for two main purposes which are (1) to improve the strength and stiffness (Ates, 2013; Azzam, 2014; Baghini et al., 2016; Iyengar et al., 2013; Naenini et al., 2012; Rezaeimalek et al., 2017a),

and (2) to enhance the long-term performances and reduce moisture susceptibility (Al-Khanbashi and Abdalla, 2006; Cameron et al., 2016; Orts et al., 2007; Liu et al., 2017; Rezaeimalek et al., 2017b). However, the polymer types evaluated in the previous research are unavailable worldwide. Moreover, Thailand's polymer applications for soil stabilization are still limited and rarely encountered. In-depth research is, therefore, required for the future development of hydrophobic road pavement materials in the country.

Liquid polymers have also been popularly used to improve the waterproof ability and workability of concrete for more than a decade (Ohama, 1998). Wang et al. (2016) listed the major types of polymer latex popularly used for enhancing concrete properties: butyl benzene latex (SBR latex), styrene-acrylic emulsion (SA latex), neoprene emulsion (CR latex), polyvinyl chloride-vinylidene chloride emulsion (PVDC latex), etc. In previous research, natural latex was not recommended to be used as the concrete modification because of its incompatibility. The polymer latex for concrete modification has been extensively used in Thailand; therefore, they are very easy to find and purchase at a reasonable price. Accordingly, the possibility of employing these concrete-modify polymers as soil stabilizers should be assessed.

This research aims to study the engineering performances, moisture susceptibility, and durability of soil enhanced by polymers for road pavement constructions. The Thailand Department of Highways (DOH) specifications were used as the criteria in this research. Moreover, the quarry by-products soil was targeted for modification and enhancement.

2. MATERIALS AND METHODS

2.1Materials

2.1.1 Parent material

Presently, manufactured aggregates from the quarry are the main sources of road construction materials in Thailand. In the quarry process, waste aggregates from the production line were usually screened out and stockpiled in the quarry area. This material is usually traded at a low price for the landfill purpose; because its gradations and some engineering properties do not satisfy the pavement design criteria. However, the physical properties of this quarry by-product soil (i.e., Atterberg limits, Los Angeles abrasion, and soundness) are aligned with the values required by the specifications. Table 1 illustrates the physical and engineering properties of the quarry by-product soil, which was employed as the parent material for stabilized soil in this research. This selected quarry by-product soil is classified as limestone

Figure 1 presents the gradation of the selected quarry by-product soil determined from the sieve analysis test (ASTM C136). It can be seen from Table 1 and Figure 1 that, based on the DOH specifications, the quarry by-product soil is not suitable for road base and subbase materials.

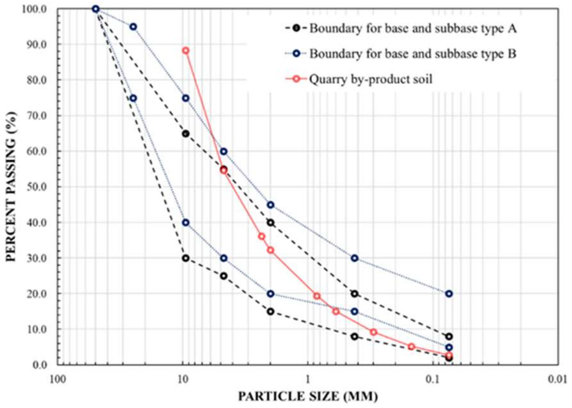

Figure 1 Particle size distribution (PSD) of quarry by-product soil compared with the gradations required for road base and subbase

2.1.2 Cement

The 'Portland cement type I' is recommended as the stabilizing agent for cement-stabilized pavement materials (both base and subbase materials) by the DOH specifications. The selected cement must be certified by the Thai Industrial Standard (TIS) No. 15 – Portland cement. However, the 'mixed cement types,' according to TIS No. 80, may be employed as the stabilizing agent for road subbase. In this research, only the Portland cement type I was chosen to prepare the polymer-stabilized cemented soils.

2.1.3 Liquid polymers

Two types of liquid polymer were employed as the main stabilizing agent in this research - (1) the SA and (2) the SBR of which important information about these two polymers is summarized in Table 2. Both types of liquid polymers are commonly used for concrete modification purposes. The SA and SBR provide excellent strength, environmental protection, and enhanced workability of the modified cement mortar (Aggarwal et al. 2007). It means that both liquid polymers are readily available in the markets. These liquid polymers were targeted and selected as the soil-modifying agents in this research.

Table 2 Properties of liquid polymers used in this research

Poly-mer	Form	Type	pH	Total Solid (%)	Ionic Nature
SA	Liquid Polymer	Dispersible	7.0 – 9.0	54 - 56	Anionic
SBR	Liquid Polymer	Dispersible	8.5 – 11.0	45 - 47	Anionic

2.2 Methodology and Test Methods

This research intends to modify the quarry by-product soil with liquid polymer and use it as the pavement material in Thailand. Therefore, the engineering properties of polymer-stabilized soil were compared with the values recommended by the DOH specifications (see Table 1). The research methodology was established for evaluating the modified soil's performances and properties, as shown in Figure 2.

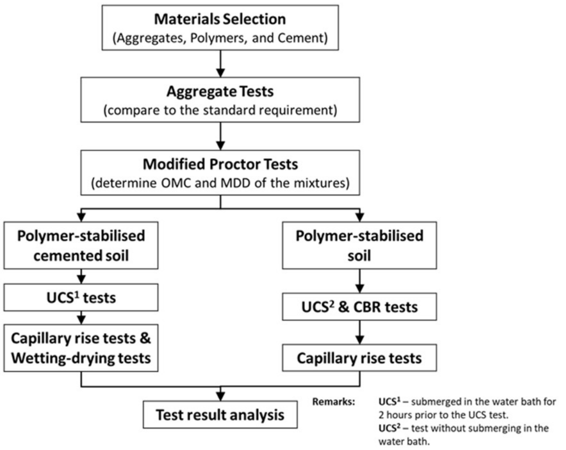

Figure 2 Research methodology

2.2.1 Modified Proctor tests

A series of modified Proctor tests (or modified compaction test) were performed in this research to determine the optimum moisture content (OMC) and the maximum dry density (MDD) of the admixtures. The specimen preparation and the test procedure proceeded according to ASTM D1557 (ASTM, 2012)

Table 1 Engineering properties of quarry by-product soil

Engineering properties (unit)	Test standards	Tested values	Recommended values from DOH* Standard			
			Base (DH-S 201)	**Subbase (DH-S 205)**	**Cement-stabilized Base (DH-S 204)**	**Cement-stabilized Subbase (DH-S 206)**
Liquid limit (%)	ASTM D4318	20	< 25	< 35	< 40	< 40
Plastic limit (%)	ASTM D4318	24	-	-	-	-
Plastic index (%)	ASTM D4318	4	< 6	< 11	< 15	< 20
CBR (%)	ASTM D1883	**5.4**	> 80**	> 25**	-	-
LAA (%)	ASTM C131	24	< 40	< 60	< 60	-
Soundness (%)	ASTM C88	2	< 9	-	-	-
USCS Group	ASTM D2487	SW	-	-	-	-
MDD (kN/m^3)	ASTM D1557	22	-	-	-	-
OMC (%)	ASTM D1557	8.2	-	-	-	-
UCS (MPa)	ASTM D1633	0.14	-	-	> 1.72***	> 0.69***
Remarks:	* Thai department of highways. ** 95 percent of MDD obtained from modified Proctor test. *** 7-day specimens molded by water equivalent to OMC (OMC was determined from a modified Proctor test).					
Abbreviations:	CBR: California Bearing Ratio LAA: Los Angeles Abrasion USCS: Unified Soil Classification System MDD: Maximum Dry Density OMC: Optimum Moisture Content UCS: Unconfined Compressive Strength					

The air-dried soils were scattered all over the mixing tray to prepare the polymer-stabilized soil specimens. Then, the defined amount of liquid polymer was evenly added to mix with the dry soil. The polymer-soil admixtures were hand-mixed until they became homogeneous.

The assigned amount of cement was thoroughly mixed with the air-dried soil in the mixing tray to prepare the polymer-stabilized cemented soils. Then, the liquid polymer was poured and mixed with the cement-soil admixtures. After that, the similar mixing process with the polymer-stabilized soil was continued until the liquid polymer was nicely blended with the cement-soil admixture. The mixing process after adding liquid polymer should be completed within 2 – 3 minutes. The limited mixing time was established to avoid the cementitious bonding developed at an early age. After the admixtures were ready, the modified Proctor tests were commenced immediately.

The primary strength test in this research reveals that 2% cement by weight of dried soil was enough to improve the compressive strength of the quarry by-product soil. The improved strength values attained the DOH requirement for the cement-stabilized subbase (greater than 0.69 MPa as specified in Table 1). For achieving the strength required for the cement-stabilized base, 3% of Portland cement is needed. Therefore, for primary investigation and economical purposes, the cement quantity equivalent to 2% by weight of dried soil was chosen to prepare the polymer-stabilized cemented soil in this research.

2.2.2 Unconfined compressive strength (UCS) test

The UCS values of the polymer-stabilized and cemented soil were determined according to ASTM D1663 (ASTM, 2000). The DOH specification required the strength of the 7-day specimens to be greater than 1,724 kPa and 689 kPa for the cement-stabilized base and subbase, respectively. For preparing the 7-day specimens, the compacted specimens were wrapped in the cling wrap to prevent moisture loss and placed in the controlled temperature chamber at 23±1.7 ºC. Before the UCS test, the specimens were submerged in the water bath for 2 hours (required by DOH standard). The water was drained from the specimen for 15 minutes before commencing the UCS tests. However, the polymer-stabilized specimens (both SA-stabilized and SBR-stabilized) dissolved and crumbled in the submerged water after 30 minutes; therefore, the water-submerging process was only performed with the polymer-stabilized cemented specimens in this research.

According to the specification (DH-S 204 and DH-S 206), the required UCS should be determined from the specimens compacted at OMC. However, the effects of molded moisture content on the UCS of stabilized soil were also investigated in this research; accordingly, the UCS test was measured from the specimens prepared from different moisture contents.

2.2.3 California bearing ratio (CBR) test

In this research, the CBR testing procedures complied with ASTM D1883 (ASTM, 2016). Based on the DOH specifications, the crushed rock base and aggregate subbase should have the minimum CBR values of 80% (for asphalt pavement) and 25%, respectively. For preparing the CBR specimens, the compacted specimens were left in the steel mold for seven days before the testing commenced. This process was performed to ensure a similar curing condition with the specimens prepared for the UCS test. In this research, the CBR values were only determined from the polymer-stabilized specimens.

2.2.4 Capillary rise test

Many researchers performed capillary rise tests to assess the water absorption potential of the compacted specimens. In this research, the Australian Standard, AS 1141.53 (Standard Australia, 1996), was used to evaluate the water absorption behavior of the polymer-stabilized soil and polymer-stabilized cemented soil specimens. For this test, the 7-day specimens were placed in the aluminum trays with the water filled up to 10-mm height (see Figure 3). The water height absorbed by the compacted specimens was then measured at the specified times and recorded for 72 hours (3 days). The capillary rise (C.R.) values at different times of measuring can be calculated based on Eq. (1)

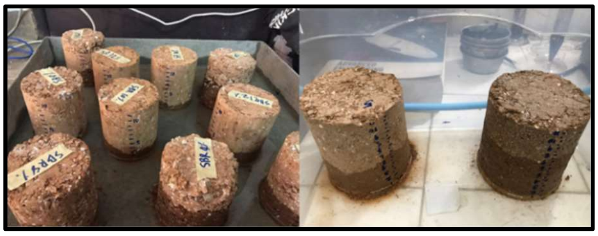

Figure 3 Water absorption and capillary rise tests

$$\mathrm{CR}\ (\%) = \frac{\mathrm{h}}{\mathrm{H}} \times 100 \qquad (1)$$

where h is the height of the capillary rise, and H is the initial height of the specimen. The capillary rise test is not compulsory for stabilized road pavement design; however, the CR value of the stabilized pavement material is generally limited to 25% of the specimen height (Kodikara et al., 2003). Previous research demonstrated that the results from CR test might unappropriated describe the moisture ingress characteristics of field material (Kodikara et al., 2003); accordingly, the CR test results were only used for the comparison purpose in this research. The moisture ingress behavior of the quarry by-product specimens, the cement-stabilized specimens, the polymer-stabilized specimens, and the polymer-stabilized cemented soils was evaluated in the next section.

2.2.5 Wetting and drying test

The wetting and drying test is commonly used to evaluate cemented soil's wet and dry durability (Wen et al., 2014). The testing procedure according to ASTM D559 (ASTM, 2015) was performed in this research. Twelve cycles of the wetting and drying process for every specimen were completed to investigate the weight loss of the test specimens. Only the weight losses of polymer-stabilized cemented soils were determined and evaluated in this research because the polymer-stabilized soils and quarry by-product soil cannot endure the submerging water process.

Based on ASTM D559, the wetting process was performed by submerging the specimens in the water for 5 hours before drying. Then, the specimens were transferred to the oven at the controlled temperature of 71±3 °C for 42 hours. After the drying process was completed, one of two replicated specimens was brushed with the wire scratch brush, as shown in Figure 4. Finally, the weight loss of each specimen was calculated and recorded. The process of wetting and drying is continued for eleven more cycles. Therefore, the test requires at least one and a half months. Eq. (2) illustrates the weight loss calculation at every wetting and drying test cycle.

$$\text{Weight loss}\ (\%) = \frac{\mathrm{A}}{\mathrm{B}} \times 100 \qquad (2)$$

where A is the original dry mass minus final dry mass, and B is the original dry mass.

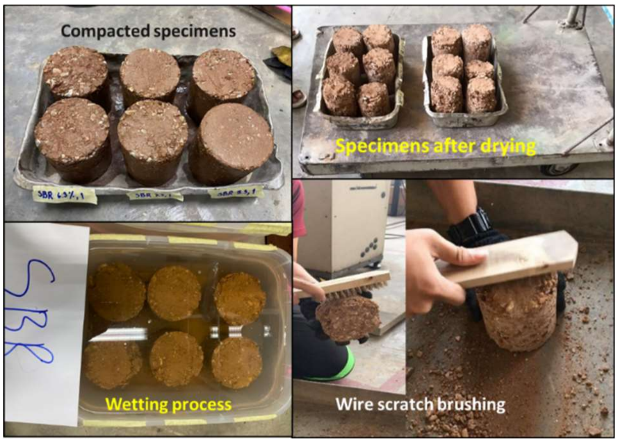

Figure 4 Wetting and drying test

3. TEST RESULTS

3.1 Modified Proctor test results

Figure 5 presents the results of the modified Proctor test performed in this research. The OMCs of the polymer-stabilized soils (both SA-stabilized and SBR-stabilized soils) are less than those obtained from the quarry by-product soil and the cement-stabilized soil. On the other hand, the OMCs of the polymer-stabilized cemented soils were higher than those determined from the quarry by-product and cement-stabilized soil. The maximum dry densities of all materials vary between 21.5 and 22.5 kN/m^3.

3.2 UCS test results

The UCS test results of the soil specimens and the modified soil specimens are presented in Figure 6. The UCS values of the quarry by-product soil and the quarry by-product soil stabilized by 2% of cement were also provided in Figure 6 as the reference.

The UCS test of quarry by-product soil was conducted instantly after the compaction process of the test specimen was completed (without submerging the specimen into the water bath). The compressive strength of the compacted quarry by-product specimen is 0.14 MPa.

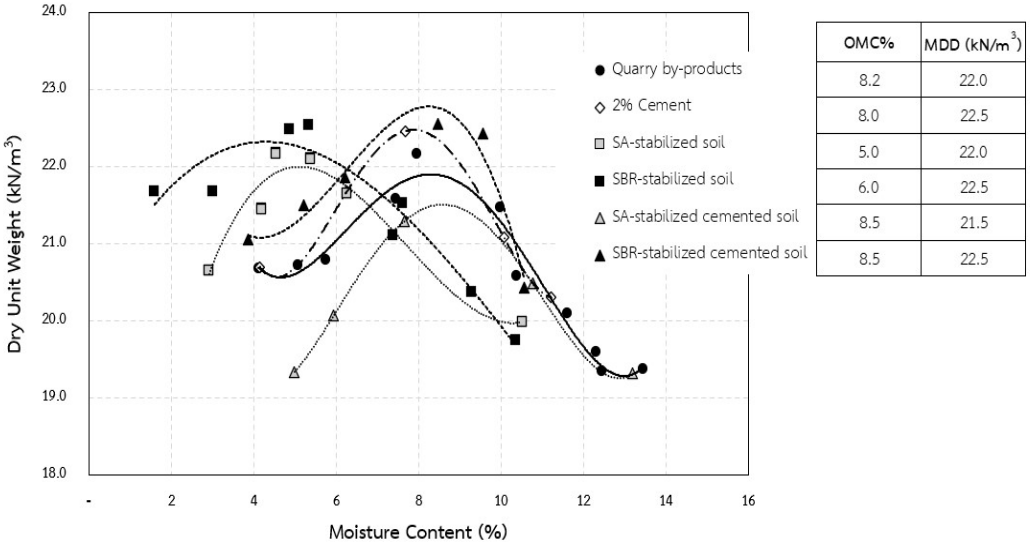

OMC%	MDD (kN/m³)
8.2	22.0
8.0	22.5
5.0	22.0
6.0	22.5
8.5	21.5
8.5	22.5

Figure 5 Modified Proctor test results

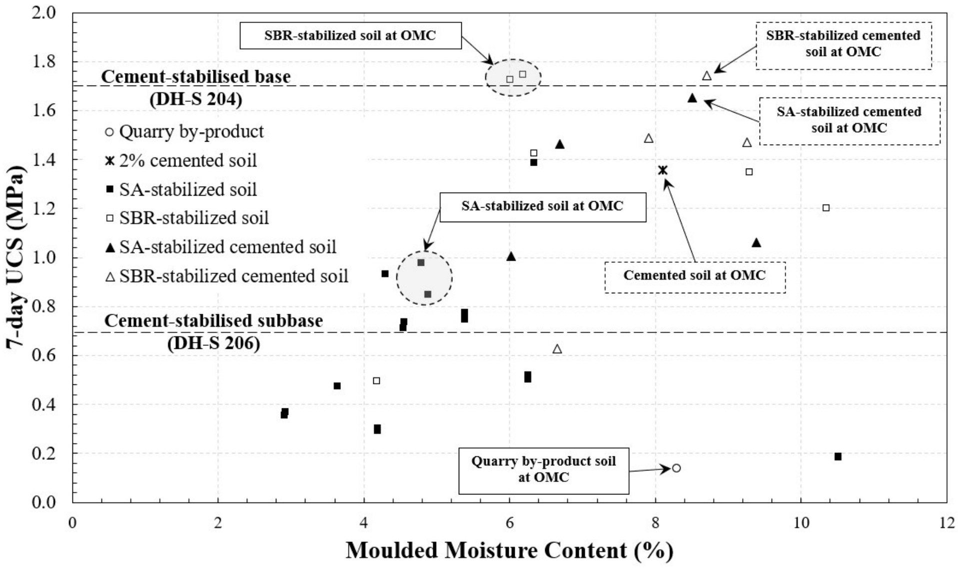

Figure 6 The UCS test results

This UCS value was averaged from 3 replicated specimens molded at OMC. On the other hand, the 2% cemented soil specimens were cured for seven days before testing. The average UCS value of 2% cemented soil is 1.36 MPa. Similar to the quarry by-product soil, it was determined from 3 replicated specimens molded at OMC.

Figure 6 shows that compressive strengths of the polymer-stabilized soil and polymer-stabilized cemented soil are greater than the value required for cement-stabilized road subbase (0.69 MPa) when an amount of water equivalent to OMC was used to mold the specimen. However, the strength tests of polymer-stabilized soils were performed without submerging the specimens into the water bath for 2 hours. There would be a reason that the strength of SBR-stabilized cemented soil (1.75 MPa) is mostly equivalent to the strength of SBR-stabilized soil (1.73 MPa). However, the strength of SA-stabilized cemented soil (1.65 MPa) is 68% greater than that of SA-stabilized soil (0.95 MPa). The great difference between USC values observed from SA-stabilized soil and SA-stabilized cemented soil required further investigation. The water suction force highly influences the compressive strength of unsaturated soil (Kohgo et al., 1993; Leroueil and Hight, 2013). Therefore, suction force may contribute to high strength values obtained from the polymer-stabilized specimens; since the polymer-stabilized specimens were tested without a water-submerging process, the degree of saturation was low (Nusit et al. 2016).

3.3 CBR test results

For the road base and subbase soils, DOH specifications require the CBR values equivalent to 80% and 25%, respectively (see Table 1). In this research, the CBRs were determined from the polymer-stabilized soils only. There would be because the CBR test is not mandatory for the cement-stabilized road base and subbase soils (see Table 1). Table 3 illustrates the results of the CBR test obtained from this research. The different ratio (%) in Table 3 is defined by Eq. (3)

Table 3 CBR test results

Road base or subbase materials	Moisture content (%)	CBR (%) (Compaction degree, %)		Different ratio** (%)	Swell index (%)
		Soaked	Unsoaked		
SA-stabilized soil	3.4	26.1 (91.8)	100.1 (91.8)	74	1.3
	5.4*	**30.0 (96.4)**	**83.2 (97.3)**	**64**	**0.9**
	7.4	7.9 (94.3)	47.4 (94.1)	83	0.2
SBR-stabilized soil	3.8	4.2 (92.4)	59.9 (91.6)	93	0.1
	5.8*	**15.8 (95.2)**	**96.2 (95.2)**	**84**	**0.6**
	7.8	59.3 (97.8)	88.0 (94.7)	33	0.9
Quarry by-product soil	**8.3***	**5.4 (95.4)**	**6.6 (98.2)**	**18**	**0.9**
Remarks	* Moisture contents equivalent to OMC were used to mold the specimens. ** Calculated based on Eq. 3.				

$$\text{Difference ratio (\%)} = \frac{\text{CBR}_{\text{unsoaked}} - \text{CBR}_{\text{soaked}}}{\text{CBR}_{\text{unsoaked}}} \times 100 \quad (3)$$

In Eq (3), $\text{CBR}_{\text{soaked}}$ is the CBR of soaked specimens, and $\text{CBR}_{\text{unsoaked}}$ is the CBR of unsoaked specimens. The different ratio (%) value indicates a high level of water sensitivity; the CBR of the test specimen may dramatically reduce if the specimen is submerged in the water.

3.4 Capillary rise test results

The capillary rise (CR) test results are presented in Figure 7 - 9. Figure 7 illustrates the CR development of polymer-stabilized soils compared to the results obtained from the quarry by-product specimens and the 2% cement-stabilized specimens. The CR test results of SA-stabilized cemented soil are presented in Fig. 8, while Fig. 9 shows the CR development measured from SBR-stabilized cemented soil molded at different moisture contents.

It can be seen from Figure 7 that the SA-stabilized soil absorbed water slower than the other specimens. The absorbed water took more than two days (48 hours) to reach the top of SA-stabilized specimens. The 2% cement-stabilized specimen shows better water susceptibility performance than the quarry by-product specimen. However, the capillary rise test of cement-stabilized soil was completed after 16 hours. Similar absorption behavior of cement-stabilized material was discovered in the previous research. Kodikara et al. (2003) observed that the capillary rose to the top of the specimen height is normally encountered if the optimum binder content was used to prepare that specimen. The optimum binder content is defined as the minimum amount of cement required to increase cement-stabilized materials' strength to the specification values.

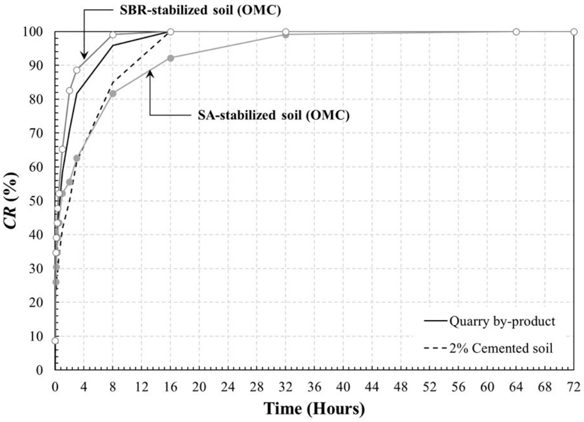

Figure 7 The CR development of the polymer-stabilized soils

The SA-stabilized cemented soil displays superior water susceptibility performance, as indicated by Figure 8. The minimum value of CR (84%) at 72 hours was obtained from the SA-stabilized cemented soil molded at OMC. Table 4 presents the compaction degrees of the capillary-rise-test specimens. For SA-stabilized cemented soil, the CR values at the same measuring times increase with the decreases in compaction degree. At about the same degree of compaction, the specimens compacted by water equivalent to the wet-side of optimum absorbed water slower than the specimens molded by water equivalent to the dry-side of optimum. The SBR-stabilized cemented soil behaves similarly to SA-stabilized soil, as demonstrated by Figure 9. However, the water rises in SBR-stabilized cemented soil developed faster than those measured from the SA-stabilized cemented soil.

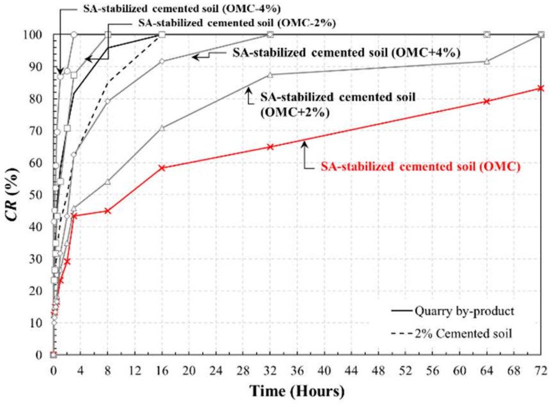

Figure 8 The CR test results of SA-stabilized cemented soil at different compacted moisture contents

Table 4 Compaction degree of the capillary-rise-test specimens

1	Quarry by-product	OMC	0	21.65	98.4
2	2% cement-stabilized soil	OMC	7	22.32	99.2
3	SA-stabilized soil	OMC	7	21.52	97.8
4	SBR-stabilized soil	OMC	7	21.67	96.3
5	SA-stabilized cemented soil	4.5% (OMC–4%)	7	20.12	93.6
6	SA-stabilized cemented soil	6.5% (OMC–2%)	7	20.81	96.8
7	SA-stabilized cemented soil	8.5% (OMC)	7	21.05	97.9
8	SA-stabilized cemented soil	10.5% (OMC+2%)	7	20.68	96.2
9	SA-stabilized cemented soil	12.5% (OMC+4%)	7	20.38	94.8
10	SBR-stabilized cemented soil	4.5% (OMC–4%)	7	21.22	94.3
11	SBR-stabilized cemented soil	6.5% (OMC–2%)	7	21.51	95.6
12	SBR-stabilized cemented soil	8.5% (OMC)	7	22.09	98.2
13	SBR-stabilized cemented soil	10.5% (OMC+2%)	7	21.71	96.5
14	SBR-stabilized cemented soil	12.5% (OMC+4%)	7	21.11	93.8

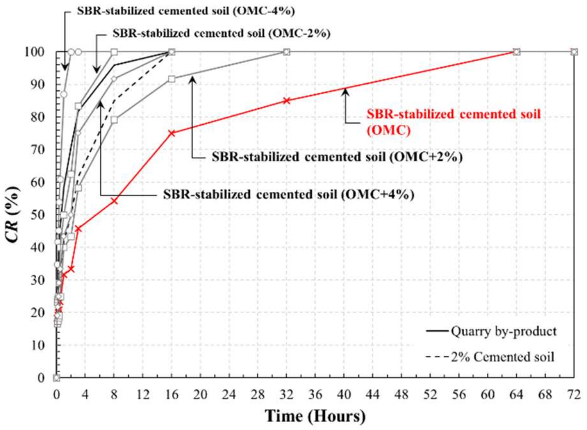

Figure 9 The CR test results of SBR-stabilized cemented soil at different compacted moisture contents

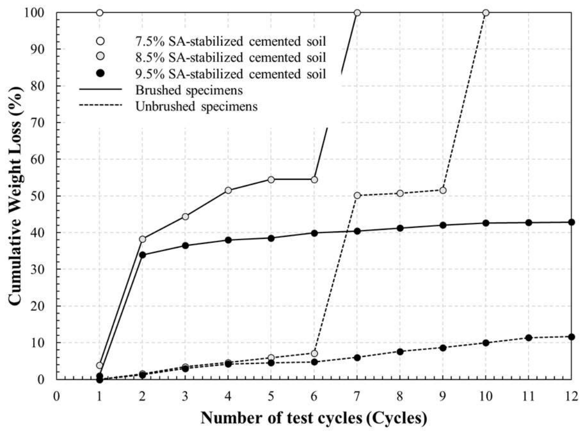

Figure 10 Wetting and drying test results of SA-stabilized cemented soils

3.5 Wetting and drying test results

Figure 10 presents the wetting and drying test results of SA-stabilized cemented soil. The test results of SBR stabilized cemented soil are demonstrated in Figure 11. Each mixture contains two replicate specimens; one was brushed after the drying process, while another was only gone through the wetting and drying process. Therefore, the weight loss due to the wire scratch brushing is the different values of weight loss between 2 replicated specimens (see Figure 11)

Figure 10 indicates 10% to 100% weight losses of SA-stabilized cemented soil. A hundred percent weight loss represents a completed specimen failure in this research. Both specimens molded by 7.5% of SA collapsed after the 1st cycle of the wetting process cycle

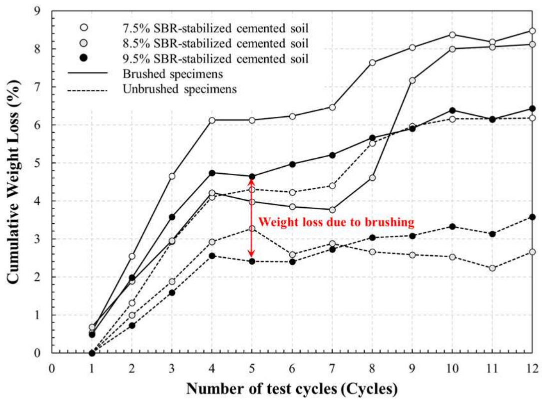

Figure 11 Wetting and drying test results of SBR-stabilized cemented soils

However, the specimens molded with 9.5% of SA survived the 12-cycle test. The final weight losses of these specimens were 12% for unbrushed specimens and 43% for brushed specimens. The huge shifts in weight loss came from two main reasons (see Figure 12); (1) the specimen was broken after the drying process, and (2) the specimen was broken after the wetting process.

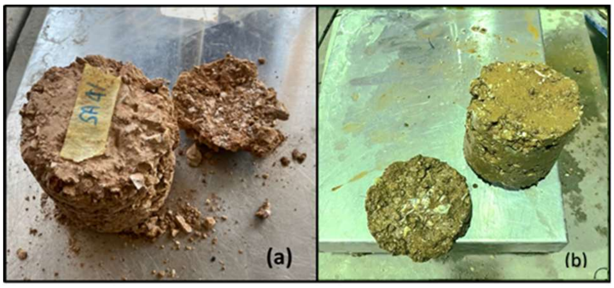

Figure 12 The specimen broken after (a) drying process, and (b) wetting process

The weight losses of less than 10% were observed from the SBR-stabilized cemented soil, as shown in Fig. 11. From the test results of this research, the SBR-stabilized cemented soils showed predominant durability performance compared to the SA-stabilized cemented soils. The greater UCS values of SBR-stabilized cemented soil may be the reason for better durability. For the SBR-stabilized cemented soils, the weight loss of brushed specimens differed from the unbrushed specimens from 1% to 5%. Moreover, all SBR-stabilized cemented specimens completed the 12 cycles of the wetting and drying process.

The weight losses of polymer-stabilized cemented soil increased concerning the wetting and drying cycles and the amount of liquid polymer added. Similar weight loss behavior can be inspected from both SA-stabilized and SBR-stabilized soil.

4.DISCUSSION

Table 5 summarises the test results evaluated in this research. The compressive strengths measured from the SA-stabilized and polymer-stabilized cemented soil attain the stabilized base specification strength criteria. Based on the UCS criteria, the 2% cemented and SBR-stabilized soil may be used as the stabilized subbase soil. However, only the SA-stabilized soil has CBR values higher than the subbase specification. The low CBR value determined from the soaked specimens is the most concerning issue in this study. The CBR of polymer-stabilized soil seems severely sensitive to moisture ingress, indicated by the different ratios in Table 3.

The capillary rise test illustrates that SA polymers can be used to reduce the water absorption rate of the stabilized soil. It also helps to decrease the capillary rise of the cement-stabilized soil. The compaction degree also greatly affects the water absorption behavior of the polymer-stabilized cemented soil. However, from the wetting and drying test, the SBR-stabilized cemented soil has the best durability performance among the test specimens. This excellent improvement may result from the increased strength of SBR-stabilized cemented soil.

Table 5 Test results determined in this research compared with the DOH specifications

Types	UCS (MPa)			CBR (%)			CR to the max. height** (Hours)	Final weight loss from wet-dry test*** (%)
	Test results	DOH base	DOH sub-base	Test results*	DOH base	DOH sub-base		
Quarry by-product soil	0.14	>1.72	>0.69	5.4	>80	>25	16	N.A.
2% cement-stabilized soil	1.36			N.A.			16	N.A.
SA-stabilized soil	0.95			30			64	N.A.
SBR-stabilized soil	1.73			15			16	N.A.
SA-stabilised cemented soil	1.65			N.A.			>72	100
SBR-stabilised cemented soil	1.75			N.A.			64	8.1
Remarks	* CBR values of soaked specimens. ** Specimens molded by water equivalent to OMC. *** Values determined from brushed specimens (molded by water equivalent to OMC). N.A. – Not Available.							

5.CONCLUSIONS

This research aims to improve the quarry by-product soil with SA and SBR polymers and employ the modified soils as road pavement materials in Thailand. The mandatory tests, i.e., physical property tests, UCS tests, and CBR tests, were performed along with the capillary rise test and wetting and drying test. The test values were then compared with the criteria issued by the Thailand department of highways. The key findings of this research are illustrated below;

- The increase in strength of the polymer-cement stabilized soil from the cemented soil at equivalent cement content causes the stabilized soil to employ as the stabilized road base materials. In addition, polymer additives may be substituted by the amount of cement added to the stabilized soil to obtain appropriate strength. The polymers, therefore, may be an environmental-friendly additive for soil stabilization in the future.
- The CBR of the polymer-stabilized soils is very sensitive to the increase in the degree of saturation. The CBR of soaked specimens reduced greatly from the unsoaked CBR, demonstrated by the different ratios in this research.
- The water absorption rate of the quarry by-product soil and the cement-stabilized soil can be reduced by adding the polymer equivalent to the OMC. The SA-stabilized cemented soil presents a superior performance in water absorption reduction. In addition, the compaction degree significantly influenced the water absorption behavior of the polymer-stabilized cemented soil. The specimens molded by the polymer on the optimum wet-side behaved differently from those molded by the dry-side.
- The study used the weight losses from 12 wetting and drying test cycles to compare the durability performance of polymer-stabilized cemented soil. The wetting and drying test results of the polymer-stabilized soil and the quarry by-product soil were unavailable since both types of soil dissolved in the water during the 1st wetting cycle. According to the

test results of this research, the SBR-stabilized cemented soil displayed the best durability performance. The increased amount of stabilized polymer reduced weight loss during the wetting and drying test.

Based on the test results, the SA-stabilized and SBR-stabilized cemented quarry by-product soil can be used as the road-stabilized subbase. The benefits of adding polymers to the cement-stabilized soil include; (1) increasing the UCS by 21% to 29%, (2) reducing the water absorption rate, and (3) enhancing the durability performances of cement-stabilized soil.

6.ACKNOWLEDGMENTS

This work was supported by Naresuan University Faculty of Engineering Scholarships and the Thailand Research Fund (TRF) scheme "TRF Research Grant for New Scholar (2019-2020)" Grant no. MRG6280053 and "TRF Research Career Development Grant (2016-2018)" Grant no. RSA5980070. Special thanks to Dr. Nanticha Kalapat for the great advice on this study. In addition, the Civil Engineering Department research team at Naresuan University, Chiang Mai University, Kasetsart University and Phayao University, Thailand, are also gratefully acknowledged for providing overview guidance and valuable input into this work.

7. REFERENCES

Aggarwal, L. K., Thapliyal, P. C., Karade, S. R., 2007. Properties of polymer-modified mortars using epoxy and acrylic emulsions. *Construction and Building Materials*,21(2),379-383. https://doi.org/10.1016/j.conbuildmat.2005.08.007

Al-Khanbashi, A., Abdalla, S. W., 2006. Evaluation of three waterborne polymers as stabilizers for sandy soil. *Geotechnical & Geological Engineering*, 24(6), 1603-1625.

ASTM., 2000. Standard test methods for compressive strength of molded soil-cement cylinders. *ASTM D1663*. West Conshohocken, PA.: ASTM International.

ASTM., 2007. Standard test method for particle-size analysis of soils. *ASTM C136*. West Conshohocken, PA.: ASTM International.

ASTM., 2012. Standard test methods for laboratory compaction characteristics of soil using modified effort (56,000 ft-lbf/ft3 (2,700 kN-m/m3)). *ASTM D1557*. West Conshohocken, PA.: ASTM International.

ASTM., 2015. Standard test methods for wetting and drying compacted soil-cement mixtures. *ASTM D559*. West Conshohocken, PA.: ASTM International.

ASTM., 2016. Standard Test Method for California Bearing Ratio (CBR) of Laboratory-Compacted Soils. *ASTM D1883*. West Conshohocken, PA.: ASTM International.

Ateş, A., 2013. The Effect of Polymer-Cement Stabilization on the Unconfined Compressive Strength of Liquefiable Soils. *International Journal of Polymer Science*, 2013, 356214.

Azzam, W. R., 2014. Utilization of polymer stabilization for improvement of clay microstructures. *Applied Clay Science 93-94*, 94-101. doi:https://doi.org/10.1016/j.clay.2014.03.006

Baghini, M. S., AIsmail, A., Naseralavi, S. S., et al., 2016. Performance evaluation of road base stabilized with styrene–butadiene copolymer latex and Portland cement. *International Journal of Pavement Research and Technology, 9(4)*, 321 – 336.

Cameron, D., Hopkins, C., Rahman, M., 2016. Hydrophobic Polymer Additive for Stabilization of Aggregates in Local Government Roads. *Procedia Engineering*,143,26-33. doi:https://doi.org/10.1016/j.proeng.2016.06.004

Erlingsson, S., Rahman, S., Salour, F., 2017. Characteristic of unbound granular materials and subgrades based on multi stage RLT testing. Transportation Geotechnics, 13, 28-42. doi:https://doi.org/10.1016/j.trgeo.2017.08.009

Jitsangiam, P., Nikraz, H., 2012. Coarse bauxite residue for roadway construction materials. *International Journal of Pavement Engineering*, 14(3), 265-273.

Jitsangiam, P., Nusit, K., Chummuneerat, S., et al., 2016. Fatigue Assessment of Cement-Treated Base for Roads: An Examination of Beam-Fatigue Tests. *Journal of Materials in Civil Engineering 28(10),* 04016095.

Kodikara, J., Lee, K. Y., Chakrabarti, S. 2003. Laboratory assessment of capillary rise in stabilized pavement materials. *Paper presented at the Proceedings of the 21st ARRB and 11th REAAA conference*, Cairns, Australia.

Kohgo, Y., Nakaho, M., Miyaki, T., 1993. Theoretical aspects of constitutive modeling for unsaturated soils. *Soils and Foundations*, 33(4), 49-63.

Leroueil, S., Hight, D. W., 2013. Compacted soils: From physics to hydraulic and mechanical behaviour. In B. Caicedo, C. Murillo, H. Laureano, J. E. Colmenares, & I. R. Berdugo (Eds.), *Advances in unsaturated soils* (pp. 41-59). Broken Sound Parkway, N.W.: CRC Press.

Liu, J., Wang, Y., Lu, Y., et al., 2017. Effect of Polyvinyl Acetate Stabilization on the Swelling-Shrinkage Properties of Expansive Soil. *International Journal of Polymer Science*, 2017, 8128020.

Naeini, S. A., Naderinia, B., Izadi, E., 2012. Unconfined compressive strength of clayey soils stabilized with waterborne polymer. *KSCE Journal of Civil Engineering*, 16(6), 943-949.

Nusit, K., Jitsangiam, P., Kodikara, J., et al., 2016. Advanced Characteristics of Cement-Treated Materials with respect to Strength Performance and Damage Evolution. *Journal of Materials in Civil Engineering 29(4)*, 04016255.

Ohama, Y., 1998. Polymer-based admixtures. Cement and Concrete Composites 20(2), 189-212. doi:https://doi.org/10.1016/S0958-9465(97)00065-6

Orts, W. J., Roa-Espinosa, A., Sojka, R. E., et al., 2007. Use of Synthetic Polymers and Biopolymers for Soil Stabilization in Agricultural, Construction, and Military Applications. *Journal of Materials in Civil Engineering19(1),*58-66. doi:doi:10.1061/(ASCE)0899-1561(2007)19:1(58)

Raucah, A. F., Katz, L. E., Liljestrand, H. M., 1993. *An Analysis of the mechanisms and efficacy of three liquid chemical soil stabilizers: volume 1*: Texas Department of Transportation.

Rezaeimalek, S., Nasouri, A., Huang, J., et al., (2017a. Comparison of short-term and long-term performances for polymer-stabilized sand and clay. *Journal of Traffic and Transportation Engineering (English Edition)*, 4(2), 145-155. doi:https://doi.org/10.1016/j.jtte.2017.01.003

Rezaeimalek, S., Huang, J., Bin-Shafique, S., 2017b. Evaluation of curing method and mix design of a moisture activated polymer for sand stabilization. *Construction and Building Materials*, 146, 210-220. doi:https://doi.org/10.1016/j.conbuildmat.2017.04.093

Standard Australia., 1996. Methods for sampling and testing aggregates - Absorption, *swell and capillary rise of compacted materials*. AS 1141.53. Sydney, NSW: Standard Australia.

Tillman, R., Scotter, D., Wallis, M., et al., 1989. Water repellency and its measurement by using intrinsic sorptivity. *Soil Research*, 27(4), 637-644.

Wang, M., Wang, R., Yao, H., et al., 2016. Research on the mechanism of polymer latex modified cement. *Construction and Building Materials*, 111, 710-718. doi:https://doi.org/10.1016/j.conbuildmat.2016.02.117

Wen, H., Muhunthan, B., Wang, J., et al., 2014. Characterization of cementitiously stabilized layers for use in pavement design and analysis *(NCHRP Report No. 789)*. Retrieved from Washington, D.C.; NCHRP.

NUEJ
Naresuan University
Engineering Journal

Lead Acid Battery Monitoring using Multiple Linear Regression Method

Thiraphong Banchong, Sumet Sittisrijan and Somporn Ruangsinchaiwanich*

Department of Electrical and Computer Engineering, Faculty of Engineering, Naresuan University, Phitsanulok, Thailand

* Corresponding author e-mail: sompornr@nu.ac.th

(Received: 16 January 2023, Revised: 9 March 2023, Accepted: 20 March 202)

Abstract

This paper is an electric motor battery monitoring system using Multiple Linear Regression. This proposed system can display battery parameters based on internet of things that afford its values of the voltage, current, and the remaining charge capacity in a real-time scenario. Also designed electronic hardwires and data storage system are illustrated. This article concerns an electric car battery status system with Multiple Linear Regression. The prototype consists of a microcontroller, current sensor module, voltage divider circuit, and MCP3008. The data of power batteries can be displayed on a smartphone and stored in the cloud server database. Eventually, this system can also be used to study battery characteristics throughout its lifespan.

Keywords: Battery Monitoring System, Multiple Linear Regression, Internet of Things

1. INTRODUCTION

Recently, Electric-drive vehicles are relatively new to the U.S. auto market, so only a small number of them have approached the end of their useful lives. As electric-drive vehicles become increasingly common, the battery-recycling market may expand Thailand and around the world have been facing environmental problems due to the increase in population, economic and social development, and the number of cars, which is causing the use of fuel to increase while energy is limited and scarce. The current energy consumption impacts the environment since engine combustion produces noise and air pollution, which also contributes to global warming and harms human health. Due to these worries, many countries, including Thailand, have prioritized that issue. There are policies and measures relating to the use of renewable energy. Because of this, automakers are focusing on utilizing renewable energy. As a result, the car has been created and is powered by electricity. To contribute to lowering pollution that harms both the environment and consumer health. Electric cars are a new alternative becoming increasingly popular in many nations (Jung at all., 2015). To meet the present needs, it has created many electric cars. Both high and low production costs, however, there is still a drawback in that inexpensive electric cars cannot display crucial status. The Internet of Things was applied to study the electric car battery status. It displays the battery power value while in use and sends it to Google Sheets every 3 seconds. However, there is still an error in that the wrong value is caused by the storage period and some data not being recorded, causing the measured value to differ from the actual value; when used continuously, this makes estimating battery power difficult. Recently, the multiple linear regression method has been proposed to apply for approximating battery power (Feng at all., 2017) and it can further to analyze the battery health (Zhang, 2019).

In this paper, current (A) and voltage (V) were collected from research on the internet of things electric car battery status system. In addition, the Z-score was utilized to exclude the aberrant data (Abdullah at all., 2014) and (Hegde at all., 2015). Obviously, online monitoring is a key player for observing lead acid battery (Badawy at all., 2020) and (Kale at all., 2022). The method of multiple linear regression and the study of additional battery data will aid in analyzing battery power and its subsequent application in an electric car battery status system with multiple linear regression.

2. BATTERY STATUS SYSTEM PROCESS

2.1 Battery

Lead acid battery has been applied for electric vehicles, since it is low cost, safe, and reliable comparing with other batteries. Basically it can transform chemical energy into electrical energy by using a galvanic cell with an anode, a cathode, and an electrolyte solution that can be either recharged or charged (Pavlov, 2011). Batteries consist of many small battery cells, which are connected in either series or parallel connection. For example, figure 1 shows a 48V DC supply as using 12V battery within series connection that electric cars usually use the 48V supply.

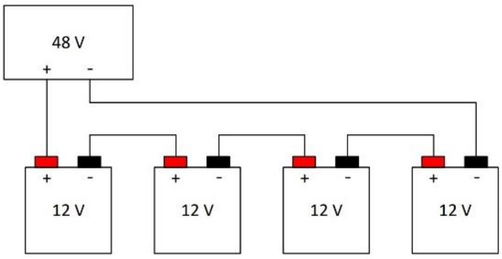

Figure 1 Battery connection

Figure 2 illustrates the utilization of the lead-acid batteries while supplying at different currents (Pavlov, 2011). For the first stage, the lead-acid batteries can basically deliver to electric load as linear characteristic. For example, when batteries are used to supply to load 0 – 10 minutes, it can supply as the linear transition period. Therefore, battery can be predicted easily. However, after 10 minutes, batteries can perform as nonlinear transition period. It is difficult to forecast battery capacity this usage time. Moreover, the battery system monitoring is required emergency a low-voltage warning system to inform to users as soon as possible.

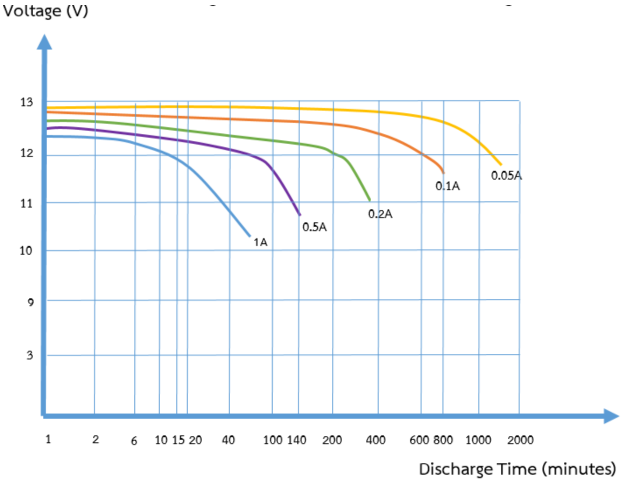

Figure 2 VRLA battery usage at different currents

2.2 The Internet of Things

The Internet of Things (IoT) electric car battery status system is a system that can display battery parameters. The battery's voltage, current, and remaining charge capacity are shown in real-time. Additionally, battery power information may be shown on a mobile device and kept in the cloud server database. The main components of the prototype system are a Wemos D1ESP8266 microcontroller board, a current measurement module to measure the battery current during operation, a voltage divider circuit to measure the battery voltage during operation, and an MCP3008 IC to convert analog signals to digital signals and amplify the status input.

Figure 3 illustrates the system and the correlation between the prototype's devices. During operation, electric cars are constantly in motion; therefore, transmitting the battery consumption data while in use is necessary. Consequently, the prototype sends real-time information to users through a portable Wi-Fi hotspot and sends the power usage status to a prepared Google Sheet.

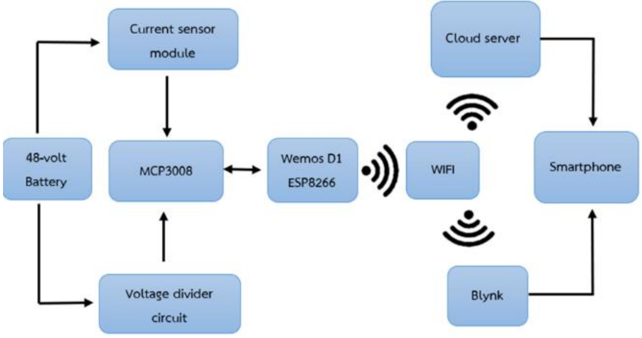

Figure 3 System components showing the battery usage of electric car

3. CASE STUDY

The program structure and operating system can be described according to this flowchart as shown in Figure 4 and also considering figure 1 that Wemos D1ESP8266 microcontroller board mainly performs the processing of battery power by using C programming. It begins by obtaining the parameters from the electric motors current sensor module. The battery voltage divider circuit accepts a voltage of 48 volts and then it can be reduced to the desired rating.

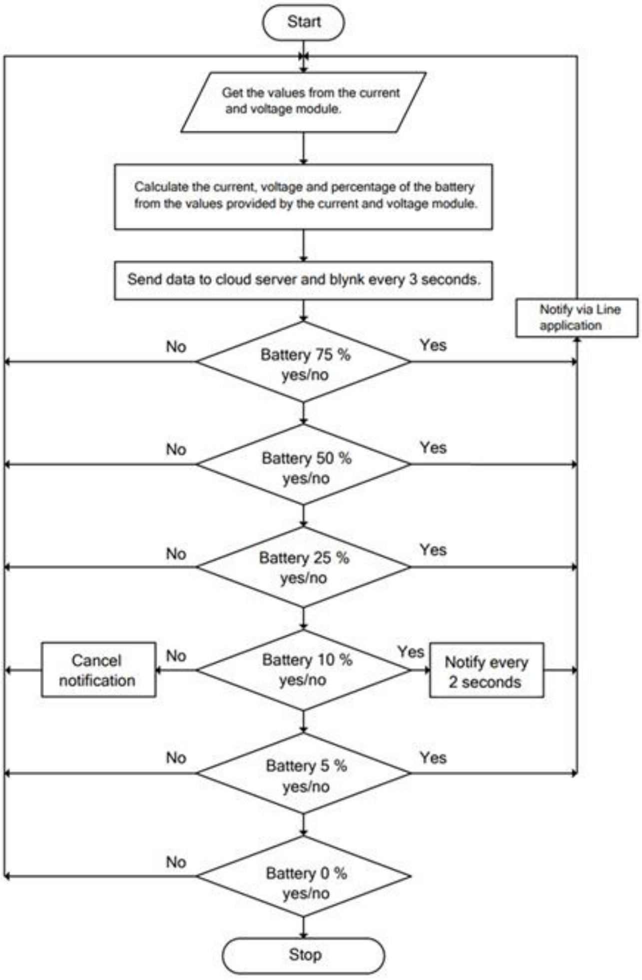

Figure 4 Prototype system program flowchart

The MCP3008 digitalizes the current and voltage. The microcontroller uses the parameters mentioned above to calculate the remaining battery power, transmitting the data to the cloud server database every 3 seconds and to the Blynk application, which calculates the remaining power percentage for example 100, 75, 50, and 25 percent, respectively. Send notices to LINE application when the specified level is reached. If the power drops below 10 percent, send a continuous (emergency) notice to the LINE application every 2 seconds to notify the user of the impending further charge. However, if there is no power left in the battery, the battery status display will stop processing, and it will resume functioning once the battery power is restored.

This study results can be summarized as follows. The WeMos D1 ESP8266 WIFI module, which is mounted in the car, captures various data. A prototype electric car with an Internet of Things battery status system has been tested. Figure 5 shows a cast study path in Naresuan University Phitsanulok, Thailand. The measured values can be transmitted to the Google Sheet. In addition, the result will send a notice to the LINE application to inform users of the remaining battery power and battery percentage in the Blynk application.

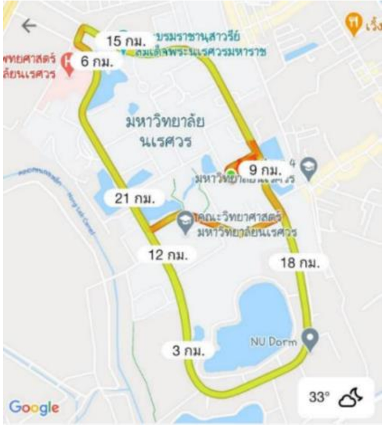

Figure 5 The path for testing the electric car's battery status system

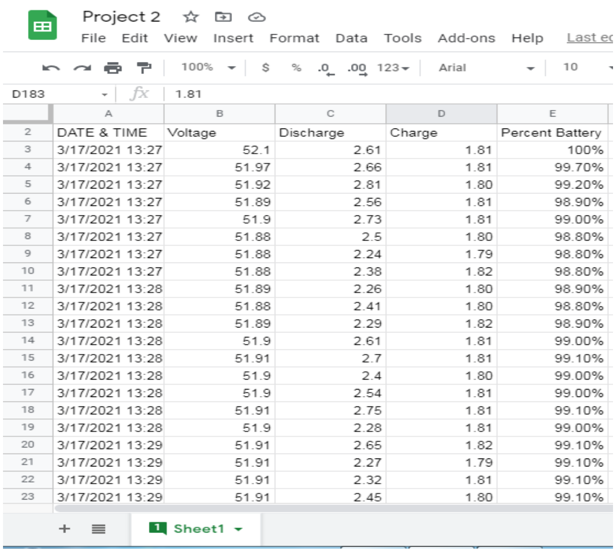

D183 fx 1.81

	A	B	C	D	E
2	DATE & TIME	Voltage	Discharge	Charge	Percent Battery
3	3/17/2021 13:27	52.1	2.61	1.81	100%
4	3/17/2021 13:27	51.97	2.66	1.81	99.70%
5	3/17/2021 13:27	51.92	2.81	1.80	99.20%
6	3/17/2021 13:27	51.89	2.56	1.81	98.90%
7	3/17/2021 13:27	51.9	2.73	1.81	99.00%
8	3/17/2021 13:27	51.88	2.5	1.80	98.80%
9	3/17/2021 13:27	51.88	2.24	1.79	98.80%
10	3/17/2021 13:27	51.88	2.38	1.82	98.80%
11	3/17/2021 13:28	51.89	2.26	1.80	98.90%
12	3/17/2021 13:28	51.88	2.41	1.80	98.80%
13	3/17/2021 13:28	51.89	2.29	1.82	98.90%
14	3/17/2021 13:28	51.9	2.61	1.81	99.00%
15	3/17/2021 13:28	51.91	2.7	1.81	99.10%
16	3/17/2021 13:28	51.9	2.4	1.80	99.00%
17	3/17/2021 13:28	51.9	2.54	1.81	99.00%
18	3/17/2021 13:28	51.91	2.75	1.81	99.10%
19	3/17/2021 13:28	51.9	2.28	1.81	99.00%
20	3/17/2021 13:29	51.91	2.65	1.82	99.10%
21	3/17/2021 13:29	51.91	2.27	1.79	99.10%
22	3/17/2021 13:29	51.91	2.32	1.81	99.10%
23	3/17/2021 13:29	51.91	2.45	1.80	99.10%

Figure 6 Battery usage status in prototypes is stored in Google Sheet

Consequently, the research findings show the battery power while using it, and the system sends the data to a Google Sheet every 3 seconds, as seen in Figure 6, and plots the remaining battery percentage. As shown in Figure 7, the test was conducted with different loads (current) with controlled values of roughly 2.35 and 6.25 A, respectively. Also the research record operation time, voltage, charge current and discharge current, so the data is of interest to academics. Therefore, the battery status system functions with a sensor.

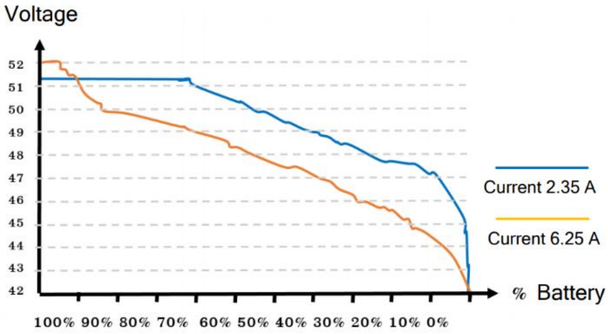

Figure 7 The graphs show the remaining percentage of batteries

4. MULTIPLE LINEAR REGRESSION MODEL

This paper is for predicting battery power of the electric car with different transition periods. The Multiple Linear Regression model is planned to apply for the prediction. The standard Multiple Linear Regression equation can be expressed as follows:

$$\psi = \beta_0 + \beta_1 X_1 + \beta_2 X_2 + \ldots + \beta_n X_n + \varepsilon \qquad (1)$$

Main parameters of battery, for example, voltage, charge current and discharge current affect the battery power prediction. Consequently, the battery status system for electric car has the following equation:

$$\psi = \beta_0 + \beta_1 X_1 + \beta_2 X_2 + \beta_3 X_3 + \varepsilon \qquad (2)$$

β_0 to β_3 is an unknown parameter known as the regression coefficient. ε is the random error and the predicted variable for the battery power of electric car. The independent variables X_1 to X_3 are the voltage, charge current, and discharge current, which influence battery power. The regression mentioned above model has been defined.

$$Battery = -409.257 + 9.844X_1 - 0.513X_2 + 0.322X_3 \qquad (3)$$

Data for battery power predictions include the following: voltage, charge current, and discharge current. The regression model described above (3) has been established.

Table 1 Descriptive statistical results of continuous variables

	% Battery	**Voltage**	**Discharge**	**Charge**
Count	24857	24857	24857	24857
Mean	79.58	49.62	2.69	1.08
Std	27.07	2.74	2.981	0.61
Min	0.00	-0.24	0.00	0.00
max	100.00	53.97	12.65	2.29

The following section will introduce the data required for model testing with JupyterLab (Ochkov at all., 2022). As shown in Figures 7, 8, and 9, JupyterLab is typically used for continuous variables with a linear correlation between data.

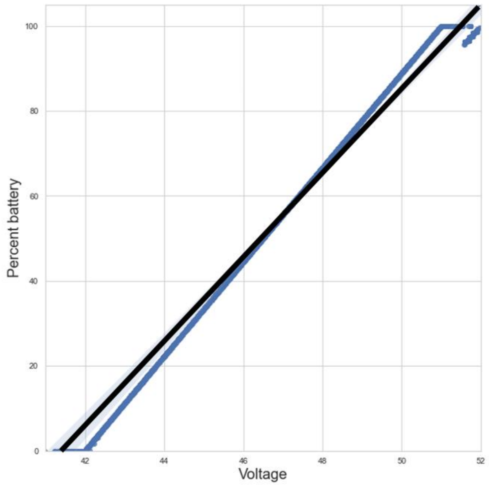

Figure 7 Correlation between voltage and battery power

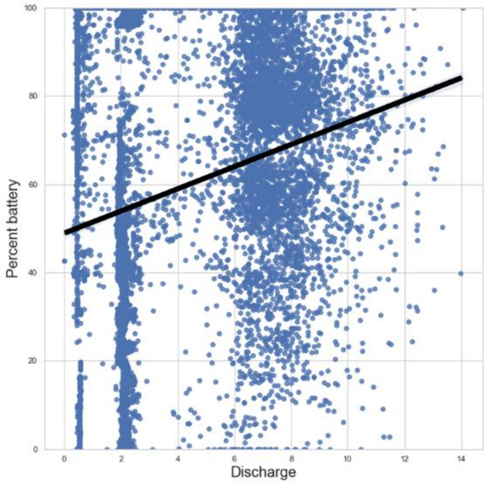

Figure 8 Correlation between discharge current and battery power

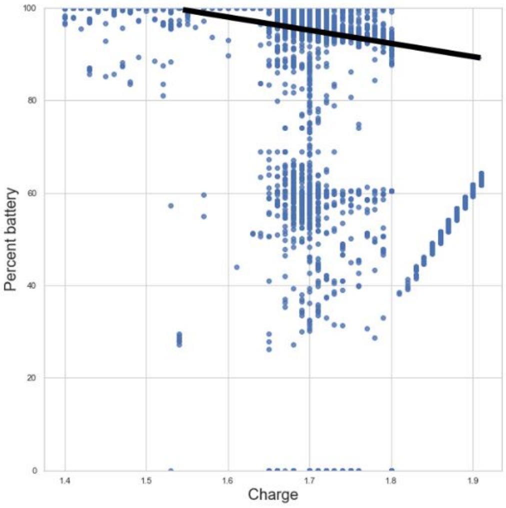

Figure 9 Correlation between charge current and battery power

Figure 7 illustrates the correlation between voltage and battery power, which can be determined by comparing battery power with three factors influencing forecasts. Figure 8 demonstrates the correlation between discharge current and battery power, while Figure 9 explains the correlation between charge current and battery power. According to the analysis above, JupyterLab is applied to multiple variables. Analysis of linear regression can be expressed as the following multivariate linear regression equation.

Table 2 Summary of model assessment

R Square	Mean Absolute Error	Mean Square Error
0.966	2.471	25.071

According to the multivariate linear regression equation, we estimate that the accuracy of test data and predictions is approximately 96.60 %. The inaccurate value may be caused by the storage period. Some data, such as the first, second, and third seconds, are not recorded. The load is always not constant; the measured data may be incorrect compared to the value that should be measured.

4. CONCLUSION

This paper is positively a battery monitoring system using the Multiple Linear Regression technique for predicting battery status. Also internet of things (IoT) is applied for either recording or displaying battery capacity of an electric car. The prototype consists of a microcontroller, current sensor module, voltage divider circuit, and MCP3008. The data of power batteries can be displayed on a smartphone and stored in the cloud server database. However, some errors have been found in MAE and MSE values, for example, the values have not yet approached 0, which is considered an error. The evidence is from the MSE values that have significantly high tolerances. Since MSE are less tolerant of outliers, which are an anomaly, the model must be able to detect them. As a result, there was an error in processing, which was used as a solution for further improvements.

5. ACKNOWLEDGMENT

The authors are grateful to the Faculty of Engineering, Naresuan University for supporting this research financially and also providing research facilities. Especially, Thiraphong Banchong and Sumet Sittisrijan are awarded as student scholarships in the Faculty of Engineering, Naresuan University.

6. REFERENCES

Abdullah, N. F., Rashid, N. E. A., Othman, K. A., & Musirin, I. (2014). Vehicles classification using Z-score and modelling neural network for forward scattering radar. *15th International Radar Symposium (IRS)* (pp. 1-4).

Badawy, A., El-Habrouk, M., Ragi Ali Rifaat Hamdy, R.A.R., Karim Hassan Youssef, K. H. (2020). Online monitoring and fault diagnosis and isolation of Valve Regulated Lead Acid batteries in Uninterruptible Power Supplies using decision trees. *11th International Renewable Energy Congress (IREC)*.

Feng, Y., & Wang, S. (2017). A forecast for bicycle rental demand based on random forests and multiple linear regression. *IEEE/ACIS 16th International Conference on Computer and Information Science (ICIS)* (pp. 101–105).

Hegde, V, & Pallavi, S. (2015). Descriptive analytical approach to analyze the student performance by comparative study using Z score factor through R language. *IEEE International Conference on Computational Intelligence and Computing Research (ICCIC)* (pp. 1-4).

Jung, J., Zhang, L., & Zhang, J. (Eds.). (2015). Lead-Acid Battery Technologies: Fundamentals, Materials, and Applications CRC Press.

Kale, S., Chaudhari, B.N. (2022), IoT Based Battery Monitoring System. *International Conference on Advances in Computing, Communication and Materials (ICACCM)*.

Ochkov, V. F., & Tikhonov, A. I. (2022) Jupyter Notebook, JupyterLab – Integrated Environment for STEM Education. *International Conference on Information Technologies in Engineering Education (Inforino)* (pp. 1-5).

Pavlov, D. (2011). Processes After Formation of the Plates and During Battery Storage. Lead-Acid Batteries: Science and Technology, Elsevier, 2011, pp. 535-566.

Zhang, Z., Li, Y., Li, L., Zhu, L., & Liu, S. (2019). Multiple linear regression for high efficiency video intra coding. *ICASSP 2019–2019 IEEE International Conference on Acoustics Speech and Signal Processing (ICASSP)* (pp. 1832-1836).

7. BIOGRAPHIES

T. Banchong Received the B.Eng in Electrical Engineering Department from Naresuan University, Thailand. Now he is studying towards a Master’s degree in Electrical Engineering at the Faculty of Engineering, Naresuan University, Phitsanulok, Thailand.

S. Sittisrijan received the B.Eng. in Electrical and Energy Engineering from the University of the Thai Chamber of Commerce, Thailand. Now he is studying towards a Master’s degree in Electrical Engineering at the Faculty of Engineering, Naresuan University, Phitsanulok, Thailand.

S. Ruangsinchaiwanich received the B.Eng. in Electrical Engineering Department from Rajamangala University of Technology Isan, Thailand, and the Ph.D. in Electronics and Electrical Engineering Department from the University of Sheffield, U.K. Furthermore, he has been working in Department of Electrical and Computer Engineering, Faculty of Engineering at Naresuang University, Phitsanulok, Thailand.

NUEJ
Naresuan University
Engineering Journal

Autobody spot-welding optimization based on Genetic Algorithm (GA)

Kawin Sonthipermpoon[1,*], Kunyaphorn Santhisan[2] and Somchai Kongnoo[1]

[1] Industrial Engineering Department, Faculty of Engineering, Naresuan University, Phitsanulok, Thailand
[2] Mechanical Engineering Department, Faculty of Engineering, Naresuan University, Phitsanulok, Thailand

* Corresponding author e-mail: sonkawin@nu.ac.th

(Received: 23 February 2023, Revised: 16 May 2023, Accepted: 22 May 2023)

Abstract

Resistance Spot Welding (RSW) is an important technology that has extensively been applied in the automotive industry. The advantages of this technology are quick and efficient for joining two pieces of metal together. The minimum number of spot welds without decreasing strength has gained much attention from researchers in recent years. In this research, the finite element (FEM) method and the Genetic Algorithm (GA) were proposed to optimize the Spot-welding spacing on automotive aluminum alloy parts. The simulation model was developed to analyze the von Mises stress generated by the side collision on the parts. According to the Insurance Institute for Highway Safety (IIHS) collision test, the computational experiment was designed that the diameter of the steel pipe 180 millimeters perpendicularly collided with the workpiece at the velocity of 14 meters per second to study the maximum stress of the workpiece. This numerical simulation cooperated with the GA for optimizing the spot-welding spacing under the lowest von Mises stress distribution criteria. From the experimental results, it was found that The GA presented the optimal spot-weld spacing on an automotive part. It could reduce the number of spot welds, weld belong-time, and power consumption by 10%. These results demonstrate that the proposed GA is a promising approach for the spot-weld spacing optimization for the Automotive part.

Keywords: Resistance spot welding (RSW), Finite Element Method (FEM), Genetic Algorithm (GA), Equivalent Von Mises stress, Pareto-based Approach.

1. INTRODUCTION

Spot welding technology is widely used in the automotive which is very popular for connecting car parts using sheet metal and for assembling parts in n parts of the structure that are prone to damage because of fatigue under fluctuating loads, according to the physical characteristics of the parts. (Ertas & Sonmez., 2011) The study found that cars one vehicle has a total of 4,800 spot-type resistance spot welding or over 80 percent of the total number of welding. Furthermore, it is expected that the number of connection points will increase in the future of cars significantly (Geißler & Hahn, 2011), which welding will increase the weight of the car and the cost of the department Related to welding. That means it will directly affect the total cost, Therefore, the design is to determine the appropriate distance of the welding point to have the smallest number of welding points under the specified conditions. Without reducing the strength of the welding point, therefore, it is something that researchers attach importance to the study and analysis to improve the quality of the welding point and modernize the production system in the automotive industry.

To address this, many studies in the literature have focused on the optimization of the spot weld distribution using a Meta-Heuristic. And (Zhang & Taylor, 2001) present the optimization problem of a spot-welded structure under fatigue life consideration using the umbrella model considered valid for fatigue life prediction. Besides, (Chae, Kwon, & Lee, 2002) purposed an h-version of adaptive meshing for spot welding locations in shell structures developed. In 2009 (Ertas & Sonmez, 2008) study is to develop a procedure to maximize the fatigue life or the load-carrying capacity of spot-weld joints by minimizing the maximum stress using finite-element analysis software. In addition (Wang, Basu, & Leiva, 2003) presents the design optimization procedure for automobile welds based on the sizing optimization technique to reduce the number of welds and save the cost, while the rigidity requirements are satisfied (Hasegawa, Sasaki, Uehara, & Kawamo, 2007) purposed a meta-heuristic method such an integer optimization method on the discrete type, by using hybrid meta-heuristics for optimization of spot-weld positions, likewise (Hu et al., 2022) present a method of multi-signal fusion to obtain the integrated signal a method of multi-signal fusion to obtain the integrated signal. However, The spot welding sequence has a notable effect on the geometrical variation of the final assembly (Tabar, Wärmefjord, & Söderberg, 2018). Various researchers proposed a multi-objective optimization of the process parameters, through the GA. (Kemda, Barka, Jahazi, & Osmani., 2022) presents the non-dominated sorting GA for minimizing production times and energies through the optimization of process parameters in resistance spot welding (RSW). And (Pashazadeh, Gheisari, & Hamedi, 2016).

RSW is a very fast process, and many factors effected to quality of the welds such as pressure, cycle time, and so on. To find the optimal number of RSW, It is necessary to know the behavior of a spot-welded structure under dynamic loads is strongly influenced by the number and locations of RSW. This paper proposes a method of GA to optimize the RSW spacing on an automotive aluminum alloy body part under the lowest von Mises stress distribution criteria.

2. THEORY AND PRINCIPLES

RSW is an old process that is still being used in welding metal welding in the automotive industry for use in the mass production of automobiles (Salem, 2011). This type of connection method is a low-cost, fast, and convenient way to create automatic welds (Ambroziak & Korzeniowski, 2010), this type of welding process depends on 3 main factors heat, pressure, and time.

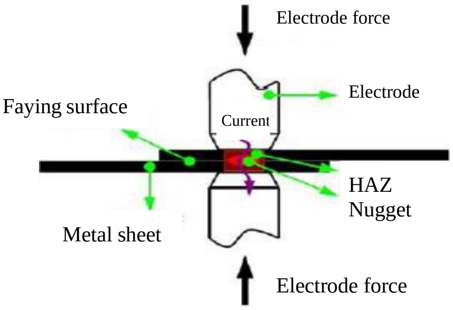

Figure 1 The resistance characteristics of resistance spot welding. (Mali & Inamdar, 2013)

Figure 1 shows the welding of two sheet materials by holding two pieces of welding. Then put pressure on the electrode. So that the current flows through both materials to connect this type of welding appears line in the middle welds. Between the two sheets of material, calling gasket. Nowadays the resistance spot welding method. Using to welding solid workpieces. To increase the strength and reduce fatigue of those parts. And it is the main technique used to weld. The metal parts of the car's body frame. The most in the Current car manufacturing industry. (Gould, 2012) From the survey, the vehicle requires hundreds of robot units for welding. They spot thousands of points from different departments. Resulting in used production time and energy costs.

Figure 2 shows the number of welding types of vehicle type sedan, which was found to have a total of 6,000 welding points and there is resistance spot welding of 4,800 welding points of the total number of welding, which is calculated as a percentage of 80 of the total number of welding points.

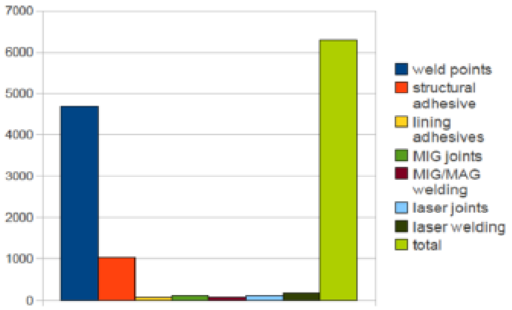

Figure 2 The making of the welded different types of cars. (Geißler & Hahn., 2011)

2.1 Genetic Algorithm

GA is a way to find the answer to optimize the response. That is the principle of the theory of evolution was Charles Darwin. (Zhao, Li, Sun, & Mei, 2009) In the past, the genetic method was used to represent the answer in binary. But now to solve a complicated. Biological theories explain the evolution of life through the mechanism of nature. Selection And heredity are the principle and guidelines for work to develop to be the best answer. Figure 3, shows genetic methodologies, the best answer instead of the binary method (Talbi, 2009).

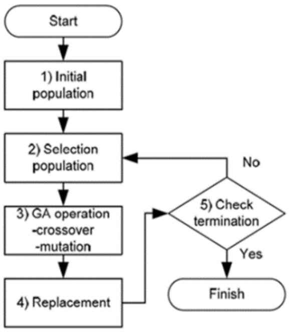

Figure 3 Genetic methodologies.

This is an algorithm the best for solving multi-objective optimization methods. (Al-Mukhtar & Doos, 2013) That is popular and has a good answer percentage of 90. The goal of the method is to approximate the value of the group of true Pareto optimal Solutions. (Jones, Mirrazavi, & Tamiz, 2002) After the development of the Multi-Objective GA in the ANSYS software is the Goal, the direct optimization. And the advantage is suitable for problems with multi-objectives.

2.2 FEM

To design engineering parts, we should first know the carrying capacity of those parts before designing. The FEM is so used as part of the technology for calculating industrial production, by applying a ready-made program for calculating various values. Nowadays car manufacturers use computer software technology to analyze automotive engineering. Problems allowing engineers to improve the quality of parts. With the finite element technique through CAE., It is a method that tests the strength of structural parts. That is popular and reliable in recent years because it can be faster than the actual test. And can reduce the cost of the actual test. The method is a numerical analysis technique for finding the approximate answer to partial differential equations with integrals is a mathematical method that is applied as a program to calculate engineering values such as stress and strain, etc. In designing engineering parts, in design engineering parts, first important know is the load capacity of that part before proceeding with the design. The principles of FEM will start by dividing the problem area into smaller parts called elements (Element) and then considering each element one by one to create an equation for each element the equation created must be consistent with the differential equation of the problem. Then, the value of each element together as a system for the series is bringing all the elements incorporated to make the shape of the real problems. The general procedure of the FEM consists of 6 steps as follows; (ibid.)

Step 1 Dividing the shape. (Figure 4)

Step 2 Selecting the estimation function within the elements that are based on the problem studied.

Step 3 Create an equation for sub-elements.

Step 4 then brings each element's compound into a large set of equations.

Step 5 Apply conditions in a large set of equations to solve unknown equations.

Step 6 When calculating the values, these values are then taken using to find other engineering values such as stress or strain.

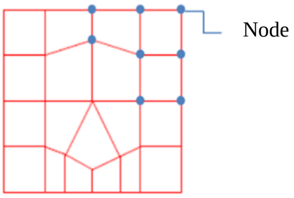

Figure 4 Break the shape of the problem into elements.

2.3 Response Surface Methodology Techniques (RSM).

There are statistical and mathematical techniques used in the design Analyze The experimental. Results for development and improvement to increase efficiency by studying the variables related by having the objectives. To find the suitability for that result. (Montgomery, 2012) Consideration of the response variable must start. By considering the variables that result from finite element analysis such as the deformation value or the stress of the system caused by various inputs etc.

3. EXPERIMENT AND IMPROVEMENT

Figure 5 shows the research methodology of this research

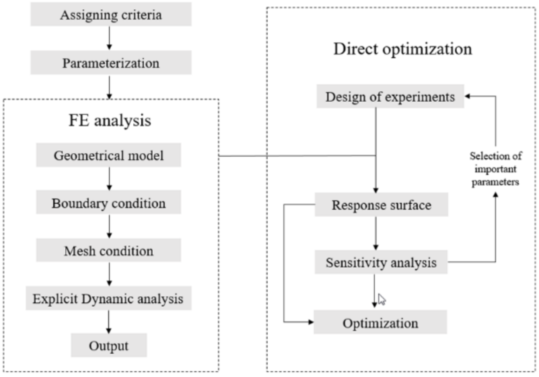

Figure 5 Research methodology

3.1 Automotive body part.

The experimental materials were the B-pillar reinforcement component that is available in all types of cars as illustrated in Figure 6

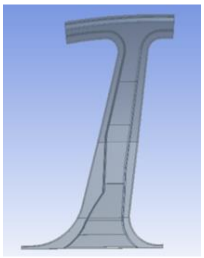

Figure 6 B-pillar reinforcement parts.

The parts are made of Aluminum Alloy 6061-T6. (S. Klimek., 2008), the thickness of 1.2 mm. The diameter of the welding is set according to the standards of The American Welding Society (AWS) and is equal to $4\sqrt{t}$ where t -thickness of the material. Table 1 shows The properties are mechanical of Aluminum Alloy 6061-T6

Table 1 Mechanical properties of Aluminum Alloy 6061-T6 used in the experiment

Item	**Crash Test**	**Ultimate (MPa)**	**Yield (MPa)**	**Elongation (%)**
Temper T6	Min	337	286	13.6
	Max	340	288	13.9

Table 2 The parameters of RSW

	Welding Condition		
Aluminum 6061	Force (kN)	Current (kA)	Time (ms)
	4.5	8	20

3.2 FEM and Explicit Dynamic.

This research considered the parameters of RSW by referring to Table 2 and the location of RSW is divided into 6 lines as shown in Figure 7

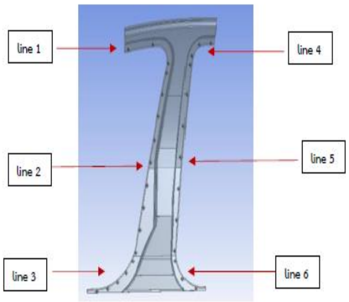

Figure 7 Welding on the B-pillar part.

Each line is defined with 3 parameters (Table 3):

1) Start point; SPn
2) Endpoint; EPn and
3) The Number of spot welds; NPn

Table 3 Parameters resistance spot welding of the B-pillar parts

Name	Definition	Original value(mm)
SP1	start point line1	20
SP2	start point line2	20
SP3	start point line3	20
SP4	start point line4	20
SP5	start point line5	20
SP6	start point line6	20
EP1	endpoint line 1	20
EP2	endpoint line 2	20
EP3	endpoint line 3	20
EP4	endpoint line 4	20
EP5	endpoint line 5	20
EP6	endpoint line 6	20
NP1	Number of spot welds line1	3
NP2	Number of spot welds line2	9
NP3	Number of spot welds line3	5
NP4	Number of spot welds line4	3
NP5	Number of spot welds line5	7
NP6	Number of spot welds line6	3

Aluminum tube 180 mm in diameter made from aluminum alloy running into the center of B-pillar parts at a speed of 14 meters per second as illustrated in Figure 8

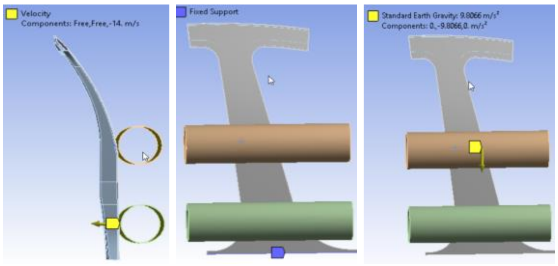

(a) (b) (c)

Figure 8 The 2 pipes running into the center of B-pillar parts.

3.2.1 Schedule for mesh.

The researcher determined the construction of the mesh as follows;

1. Set the method of creating Mesh as an Adaptive
2. The element size is the default
3. Physical preference: Explicit
4. Quality mesh = High smoothness
5. Growth rate = 1.2
6. Transition = slow
7. Element order = Linear
8. Initial size seed = Assembly
9. Span angle center = coarse

Once all the settings have been configured, the program can create the mesh. (Figure 9)

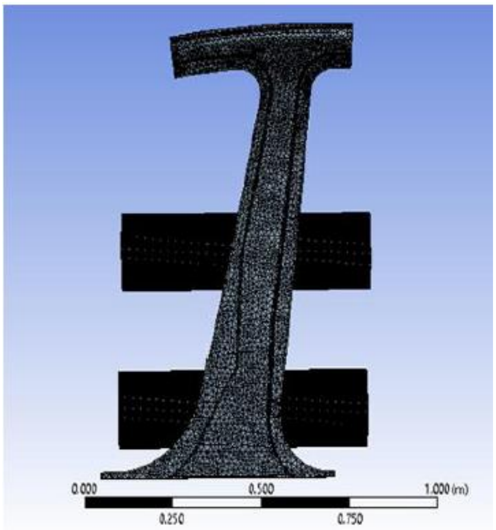

Figure 9 Mesh of parts.

3.3 Using GA in Structural Optimization

After creating the FEM model, the next step is to set up the optimization model. GA is introduced to determine the optimal spacing of RSW. In this research, the parameters in genetic search required by (Gatzi, Uebersax, & Konig, 2000) can be summarized in Table 4, which were searched for various structural problems with ANSYS software and found that the solution was effective.

Table 4 The parameters of GA

Parameters	Value
Initial population	100
Selection population	50
Crossover probability	0.98
Mutation probability	0.01

To generate the offspring and fitness function can be calculated by equations 1 and 2, respectively;

$$\text{offspring1} = \text{a} \times Parent1 + (1 - a) \times Parent2$$
$$\text{offspring2} = (1 - \text{a}) \times Parent1 + a \times Parent2 \qquad (1)$$

Fitness function: Minimize σ_e (Vonmises Stress)

$$F(X) = \ (f_1(x), f_2(x), \ldots, f_m(x)) \tag{2}$$

Subject to

$$g_j(X) \leq 0 \quad j = 1,2,3$$

$$X_i^l \leq X_i \leq X_i^u \quad i = 1,2,3$$

Where

$f_i(x)$ - Design component function

$g_i(x)$- the weight of the parameter

X_i^l - The upper bound of the design variable vector.

X_i^u - The lower bound of the design variable vector.

There are 2 conditions to stop the calculation as follows:

1) A Pareto percentage constraint is not more than 70 percent.

2) The value of the objective function initially did not change or there was a large change in the data according to the convergence stability percentage stop condition to find the initial constant based on the mean and standard deviation of parameters in the range of data export.

4. RESULTS

4.1 Analysis of experimental finite elements pre-application genetic.

Experiment with FEM to get the maximum total stress. That occurs on parts with spot resistance from both experiments results as follows;

4.1.1 6061-T6 Aluminum Plate Parts.

Figure 10 shows the distribution of total stress that occurs in a sheet equal to 424.93 MPa Appear is the total stress higher than the stress at the yield point. Resulting in the middle parts becoming deflected and deformed. With the total stress values from the experiment.

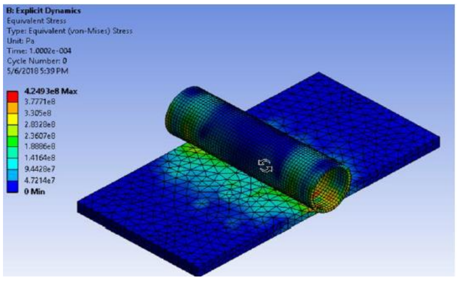

Figure 10 The result of finite element experiment plate parts.

4.1.2 B-pillar part

Figure 11 shows the result of total stress Resulting from the collision speed of two hollow pipes. And using welding parts parameters in Table 3 the maximum total stress is 302.09 MPa

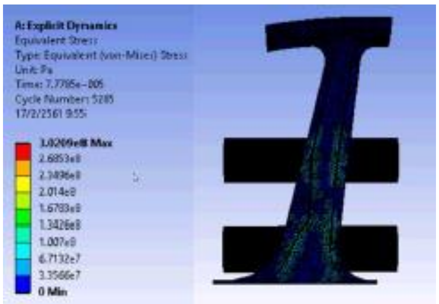

Figure 11 The result of finite element experiment B-pillar.

4.2 Analysis of experimental results with multiple-purpose genetic algorithm.

Bring the value maximum total stress of 2 cases, for the process of finding the appropriate distance between the junction points of the part as follows;

4.2.1 Aluminum Plate Parts 6061-T6.

This section brings the total stress to the optimization process using a multi-purpose GA and the experimental results of finding a suitable value. (Table 5)

The optimization process takes approximately 10 minutes to process. The answer converges design point 343 (Table 5) with the calculation details. Choose the candidate answer 1. Figure 12 shows the convergence conditions which consist of the Pareto percentage graph and the Convergence stability percentage graph. The Pareto percentage graph begins to converge to design point 150 and the Convergence stability percentage design point 300. After that, there is no change or no change. Answer developed.

Table 5 Suitable values of aluminum plate parts 6061-T6

Name	SP1 (mm)	SP2 (mm)	EP1 (mm)	EP2 (mm)	NP1	NP2	σ_{VM} (MPa)
1	2.04	2.04	2.04	2.04	2.04	2.04	169.71
2	2.7673	6.04	2.12	4.7067	3.64	3.1829	-
3	3.4945	4.04	2.2	7.3733	5.24	4.3257	-
4	4.2218	8.04	2.28	2.9289	6.84	5.4686	-
5	4.9491	3.04	2.36	5.5956	8.44	6.6114	-
6	5.6764	7.04	2.44	8.2622	2.36	7.7543	-
7	6.4036	5.04	2.52	3.8178	3.96	8.8971	-
8	7.1309	9.04	2.6	6.4844	5.56	2.2033	-
9	7.8582	2.54	2.68	9.1511	7.16	3.3461	-
10	8.5855	6.54	2.76	2.3363	8.76	4.489	-
11	9.3127	4.54	2.84	5.003	2.68	5.6318	-
…	…	…	…	…	…	…	…
330	2.034	2.077	2.0489	2.049	2.04	2.0352	158.22
331	2.2534	2.077	2.04	2.4977	2.1483	2.1505	173.41
332	2.0285	2.0741	2.0014	2.4982	2.0909	2.1462	167.8
333	2.1253	2.0397	2.0426	2.4971	2.04	2.1453	155.09
334	2.2264	2.915	6.0763	2.0904	2.2785	2.144	195.54
335	2.2348	2.04	6.2304	2.4643	2.04	2.1423	191.17
336	2.1619	2.0357	2.248	2.0811	2.0396	2.1405	175.3
337	2.2291	2.04	6.0752	2.4547	2.04	2.1423	169.28
338	2.245	2.0314	2.2519	2.0005	2.04	2.1453	164.16
339	2.2348	2.0856	6.2529	2.5377	2.04	2.1423	167.01
340	2.0402	2.0398	6.0752	2.04	2.04	2.1423	158.25
341	2.2346	2.04	2.24	2.04	2.04	2.149	178.73
342	2.0403	2.0371	2.04	2.4954	2.04	2.1482	164.57
343	2.1584	2.0812	2.248	2.4985	2.04	2.1405	148.85

Table 6 Suitable values of B-pillar parts

No.	NP1	NP2	NP3	NP4	NP5	NP6	σ_{VM}(MPa)
1	18.02	18.02	18.02	18.02	18.02	-	-
2	4.01	7.17	4.28	2.11	7.05	2.04	-
3	5.01	7.33	4.56	2.20	7.10	2.07	-
4	3.34	7.48	4.83	2.30	7.14	2.11	-
5	4.34	7.64	5.10	2.40	7.19	2.14	-
6	5.34	7.80	5.37	2.49	7.24	2.17	-
7	3.68	7.96	5.65	2.59	7.28	2.21	-
8	4.68	8.12	5.92	2.69	7.33	2.24	-
9	5.68	8.27	6.19	2.78	7.38	2.28	-
10	3.12	8.43	6.46	2.88	7.42	2.31	-
11	4.126	8.59	6.74	2.98	7.47	2.34	-
12	5.126	8.75	4.03	3.07	7.52	2.38	-
13	3.459	8.90	4.31	3.17	7.56	2.41	-
….	…	…	…	…	…	…	…
582	19.944	19.327	7.4331	21.851	18.817	3.1032	289.33
583	19.266	18.99	7.242	18.474	18.754	3.087	292.02
584	18.188	18.118	7.435	18.365	18.06	3.2316	285.91
585	18.005	180.089	7.2597	21.078	18.79	3.229	292.36
586	19.257	18.092	7.4258	18.109	18.182	3.213	291.30
587	19.144	18.93	7.2543	21.515	18.759	3.0886	290.11
588	19.856	18.989	7.396	21.756	20.88	3.007	-
586	19.257	18.092	7.425	18.109	18.182	3.231	295.61
587	19.144	18.93	7.254	21.515	18.759	3.088	292.85
588	19.856	18.989	7.396	21.756	20.88	3.007	-
589	18.258	18.073	7.390	18.051	18.069	2.332	282.366
590	19.935	19.314	7.431	21.763	18.82	3.138	287.91
591	18.031	18.089	7.254	18.109	18.063	3.2299	263.88
592	19.63	18.092	7.4313	21.484	18.182	3.2446	297.43
593	19.944	18.12	7.4331	18.454	18.045	3.1032	294.57
594	18.198	19.214	7.4331	21.668	18.902	3.0767	293.61

*SP1, SP2, SP3, SP4, SP5, SP6, EP1, EP2, EP3, EP4, EP5, EP6 (mm) * σ_{VM} (MPa)

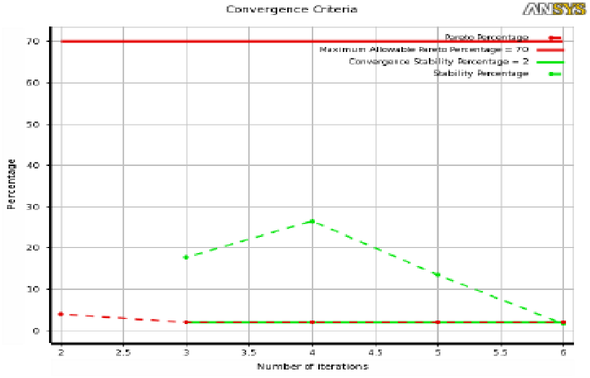

Figure 12 Convergence conditions of aluminum plate parts 6061-T6

4.2.2 B-pillar parts.

The process of finding the suitable value experimental results in Table 6 for finding the 3 best answers.

The optimization process takes approximately 30 minutes to process. The answer converges the design point 594 with the calculation details. (Table 6) Choose the candidate answer 1. Figure 13 shows a graph of convergence. Which consists of the Pareto percentage graph and the Convergence constant line graph. The Pareto percentage graph began converging at the design point at 200, and the design at 150. And both graphs converge at the number of iterations at 11 or around 550. After that, developed no more answers and the calculation stops at design point 594.

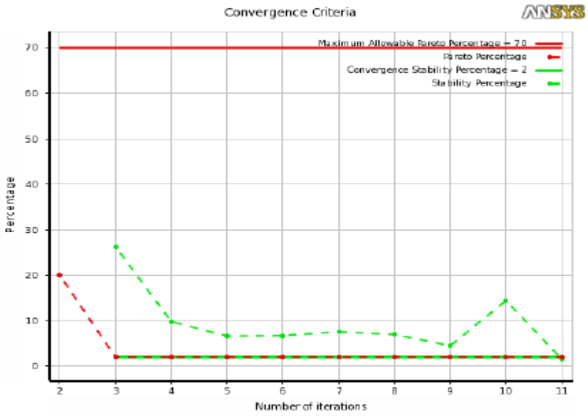

Figure 13 Convergence conditions of B-pillar parts

4.3 Graphic display

Display experimental results in a graphic format. To see the distribution of the total stress value on the part.

4.3.1 Aluminum alloy 6061-T6

After that, take the parameter of Candidate Answer 1 from the experiment in Section 4.1.1. Re-use the Finite Element Analysis program. That the maximum stress equals 139.64 MPa Which is lower than the total stress. Before using Multi-purpose, genetic methodologies which stress equals 424.93 MPa (Figure 14)

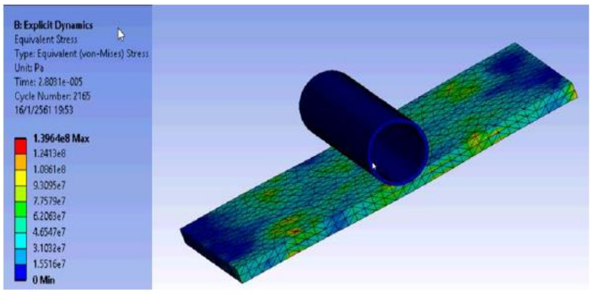

Figure 14 The result of finite elements experiment with 6061-T6 aluminum alloy plate

When bringing the original parameters in Table 1 compare. Found the number of welds reduces by percentage 80 of the original weld number. Cause in the maximum total stress total energy. And the time used to connect the pieces reduces by a percentage of 80 too. (Table 7)

4.3.2 B-pillar part.

After that, take the parameter of Candidate Answer 1 from the experiment in Section 4.1.2 Re-use the Finite Element Analysis program. Figure 15, shows the maximum stress equals 302.09 MPa Which is lower than the total stress. Before using Multi-purpose, genetic methodologies which are stress equals 424.93 MPa when bringing the original parameters to compare. Found the number of welds reduces by percentage 10 of the original weld number. Cause in the maximum total stress total energy. And the time used to connect the pieces reduces by a percentage of 10 too. (Table 8)

Table 7 Parameter comparisons before and after of aluminum alloy 6061-T6 parts

Name	Definition	Before	After	Compare
SP1 (mm)	start point line1	2	2.0368	+0.0368
SP2 (mm)	start point line2	2	2.3065	+0.3065
EP1 (mm)	endpoint line 1	2	2.04	+2.04
EP2 (mm)	endpoint line 2	2	2.0567	+2.0567
NP1 (mm)	Number of welds line1	10	2.024	8
NP2 (mm)	Number of welds line2	10	2.1476	8
σ_x (MPa)	Equivalent von Mises stress	424.93	139.34	285.29

Table 8 Parameter comparison

Name	Definition	Before	After	Compare
SP1(mm)	start point line1	20	21.654	+1.654
SP2(mm)	start point line2	20	18.308	-1.692
SP3(mm)	start point line3	20	18.721	-1.279
SP4(mm)	start point line4	20	18.015	-1.985
SP5(mm)	start point line5	20	19.169	-0.837
SP6(mm)	start point line6	20	21.708	+1.708
EP1(mm)	endpoint line 1	20	21.482	+1.428
EP2(mm)	endpoint line 2	20	20.353	+0.353
EP3(mm)	endpoint line 3	20	19.869	-0.131
EP4(mm)	endpoint line 4	20	19.114	-0.866
EP5(mm)	endpoint line 5	20	18.089	-1.91
EP6(mm)	endpoint line 6	20	18.79	-1.21
NP1(mm)	Number of spot welds line1	3	3.0229	0
NP2(mm)	Number of spot welds line2	9	7.0146	2
NP3(mm)	Number of spot welds line3	5	5.0318	0
NP4(mm)	Number of spot welds line4	3	2.179	1
NP5(mm)	Number of spot welds line5	7	7.4311	0
NP6(mm)	Number of spot welds line6	3	3.2291	0
σ_x (MPa)	Equivalent von Mises stress	302.09	270.16	-32.7

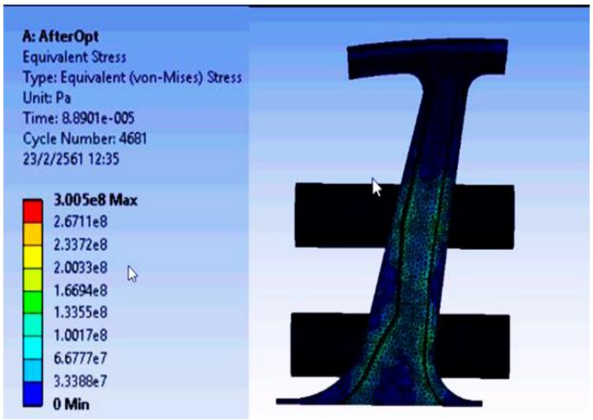
A: AfterOpt
Equivalent Stress
Type: Equivalent (von-Mises) Stress
Unit: Pa
Time: 8.8901e-005
Cycle Number: 4681
23/2/2561 12:35

Figure 15 The result of FEM

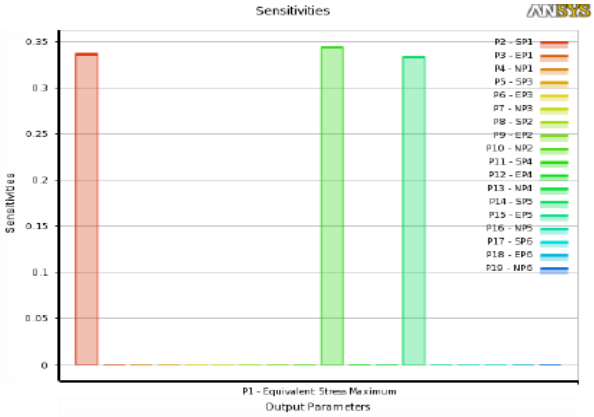

Figure 16 The sensitivity of parameters

4.4 Response Surface Methodology

This was the analysis of a method design to solve problems of design quality. An analysis of experimental. Results for development and improvement to increase parameter efficiency are most suitable, for testing sensitivity analysis next time.

4.5 Sensitivity analysis

Select these parameters to increase the efficiency of the answer with a sensitivity analysis (Figure 16) the graph shows the response sensitivity of parameters (P1) to those changes to the design variable. consists of variables SP1, SP2, SP3, SP4, SP5, SP6, EP1, EP2, EP3, EP4, EP5, EP6, NP1, NP2, NP3, NP4, NP5, and NP6 that have found 3 design variables at the parameter Showed sensitivity such as SP1, SP4, and SP5 with response sensitivity of 0.33743, 0.34463 and 0.33426 respectively.

5. CONCLUSION

1. Parameters that have the highest total stress values parameters had P3, P12, and P15 had the highest influence on total stress considering the response sensitivity analysis with values of 0.33743, 0.34463, and 0.33426 respectively.
2. Application of genetic methods to determine the distance of the resistance spot welding by Application of a multi-purpose genetic algorithm to find the suitable distance of the welding The results of both before and after the experiment showed that in the Number of welding points, Total energy value And the time it takes to connect the Aluminum alloy 6061-T6 plate parts is reduced to percentage 80 and in the B-pillar parts Number of welding points, total energy value and the time used to connect the pieces is reduced to 10%.

6. REFERENCES

Al-Mukhtar, A., & Doos, Q. (2013). The Spot Weldability of Carbon Steel Sheet. *Advances in Materials Science and Engineering, 2013*, 1-6. doi:10.1155/2013/146896

Ambroziak, A., & Korzeniowski, M. (2010). Using Resistance Spot Welding for Joining Aluminium Elements in Automotive Industry. *Archives of Civil and Mechanical Engineering, 10*, 5–13. doi:10.1016/S1644-9665(12)60126-5

Chae, S.-W., Kwon, K.-Y., & Lee, T.-S. (2002). An optimal design system for spot welding locations. *Finite Elements in Analysis and Design, 38*(3), 277-294. doi:https://doi.org/10.1016/S0168-874X(01)00064-6

Ertas, A.H. & Sonmez, F.O. (2008). Optimization of spot-weld joints. *Proceedings of the Institution of Mechanical Engineers, Part C: Journal of Mechanical Engineering Science, 223*(3), 545-555. doi:10.1243/09544062JMES1171

Ertas, A.H. & Sonmez, F.O. (2011). Design optimization of spot-welded plates for maximum fatigue life. *Finite Elements in Analysis and Design, 47*(4), 413-423. doi:https://doi.org/10.1016/j.finel.2010.11.003

Gatzi, R., Uebersax, M., & Konig, O. (2000). Structural Optimization Tool using Genetic Algorithms and Ansys.

Geißler, G. & Hahn, T. (2011). *Process development for multi-discriplinary spot weld optimization with CAX-LOCO, LS-OPT and ANSA.* Paper presented at the ANSA & μETA International Conference, Makedonia Palace, Thessaloniki, Greece.

Gould, B. (2012). *Joining Aluminum Sheet in the Automotive Industry – A 30 Year History Resistance welding , mechanical fasteners , and ultrasonic welding are examined in this overview of joining technology*.

Hasegawa, H., Sasaki, H., Uehara, H., & Kawamo, K. (2007). The optimisation of spot-weld positions for vehicle design by using hybrid meta-heuristics. *International Journal of Vehicle Design - INT J VEH DES, 43*. doi:10.1504/IJVD.2007.012301

Hu, J., Bi, J., Liu, H., Li, Y., Ao, S., & Luo, Z. (2022). Prediction of Resistance Spot Welding Quality Based on BPNN Optimized by Improved Sparrow Search Algorithm. *Materials, 15*(20), 7323.

Jones, D. F., Mirrazavi, S. K., & Tamiz, M. (2002). Multi-objective meta-heuristics: An overview of the current state-of-the-art. *European Journal of Operational Research, 137*(1), 1-9. doi:https://doi.org/10.1016/S0377-2217(01)00123-0

Kemda, F., Barka, B.V. Jahazi, M & Osmani, D. (2022). Multi-Objective Optimization of Process Parameters in Resistance Spot Welding of A36 Mild Steel and Hot Dipped Galvanized Steel Sheets Using Non-dominated Sorting Genetic Algorithm. *Metals and Materials International, 28*(2), 487-502. doi:10.1007/s12540-021-00986-9

Mali, M. P., & Inamdar, K. (2013). EFFECT OF SPOT WELD POSITION VARIATION ON QUALITY OF AUTOMOBILE SHEET METAL PARTS. *International Journal of Applied Research in Mechanical Engineering*, 170-174. doi:10.47893/IJARME.2013.1081

Montgomery, D. C. (2012). *Design and Analysis of Experiments, 8th Edition*: John Wiley & Sons, Incorporated.

Pashazadeh, H., Gheisari, Y., & Hamedi, M. (2016). Statistical modeling and optimization of resistance spot welding process parameters using neural networks and multi-objective genetic algorithm. *Journal of Intelligent Manufacturing, 27*(3), 549-559. doi:10.1007/s10845-014-0891-x

Salem, M. (2011). *Control and Power Supply for Resistance Spot Welding (RSW).* (Graduate Program in Electrical and Computer Engineering), The University of Western Ontario,

Tabar, R. S., Wärmefjord, K., & Söderberg, R. (2018). Evaluating evolutionary algorithms on spot welding sequence optimization with respect to geometrical variation. *Procedia CIRP, 75*, 421-426. doi:https://doi.org/10.1016/j.procir.2018.04.061

Talbi, E.-G. (2009). *Metaheuristics: From Design to Implementation*: WILEY.

Wang, L., Basu, P., & Leiva, J. (2003). Design optimisation of automobile welds. *International Journal of Vehicle Design - INT J VEH DES, 31*. doi:10.1504 /IJVD. 2003. 00 3352

Zhang, Y., & Taylor, D. (2001). Optimization of spot-welded structures. *Finite Elements in Analysis and Design, 37*, 1013-1022. doi:10.1016/ S0168-874X(01)00046-4

Zhao, F., Li, S., Sun, J., & Mei, D. (2009). Genetic algorithm for the one-commodity pickup-and-delivery traveling salesman problem. *Computers & Industrial Engineering, 56*(4), 1642-1648. doi:https://doi.org/10.1016/j.cie.2008.10.014

7. BIOGRAPHIES

Kawin Sonthipermpoon, he received B.S.degree in Physics from Srinakarinwirot Phisanulok campus, Thailand in 1985 and M.Eng. degree in Electrical Engineering from King Mongkut’s Institute of Technology Ladkrabang (KMITL), D.Eng. in Manufacturing Systems Engineering from Asian Institue of Technology (AIT), Thailand and received the Alexander von Humboldt Foundation scholarship to do Post-doctoral research in the Aerodynamic impeller design for Aero-Engines at the Institute of Turbomachinery, Hannover University, Germany. From 2005 - onwards, Associate Professor, Naresuan University, continue duties: Research in the field of Computational Fluid Dynamics (CFDs), Renewable energy such as Dish-Stirling Energy Systems. CNC machining application and CAD/CAM/CAE design, Enterprise Resource Planning (ERP), Information Technology as well as Robotics application and Smart Manufacturing Systems Engineering.

Kunyaphorn Santhisan, she received Bachelor's degree in Mechanical Engineering, Master's degree in Management Engineering from Naresuan University in 2013. The present a Ph.D. student in Mechanical Engineering at Naresuan University. Research interests in the field of Computational Fluid Dynamic (CFD) and Discrete Element Method (DEM)

Somchai Kongnoo, he received the B.I.Ed. Industrial Engineering from Pathumwan Institute of Technology in 2003, M.Eng. Management Engineering from Naresuan University in 2013. The present studying a Ph.D. in Management Engineering at Naresuan University. From 2000 to 2011, he was a Design Engineer in Pichit Industrial Works Co., Ltd., present is Schunk Carbon Technology Co., Ltd. (Schunk Group). Responsibilities about mechanical machine design, tooling design, CAD/CAM/CNC and manufacturing process. The last position is Engineering Design Manager. Since 2011, he has been a teacher at Production Machine Tool Department of Phitsanulok Technical College.